Rupture Behavior Characterization of Healthy Porcine Aorta Using the SymconCT Setup

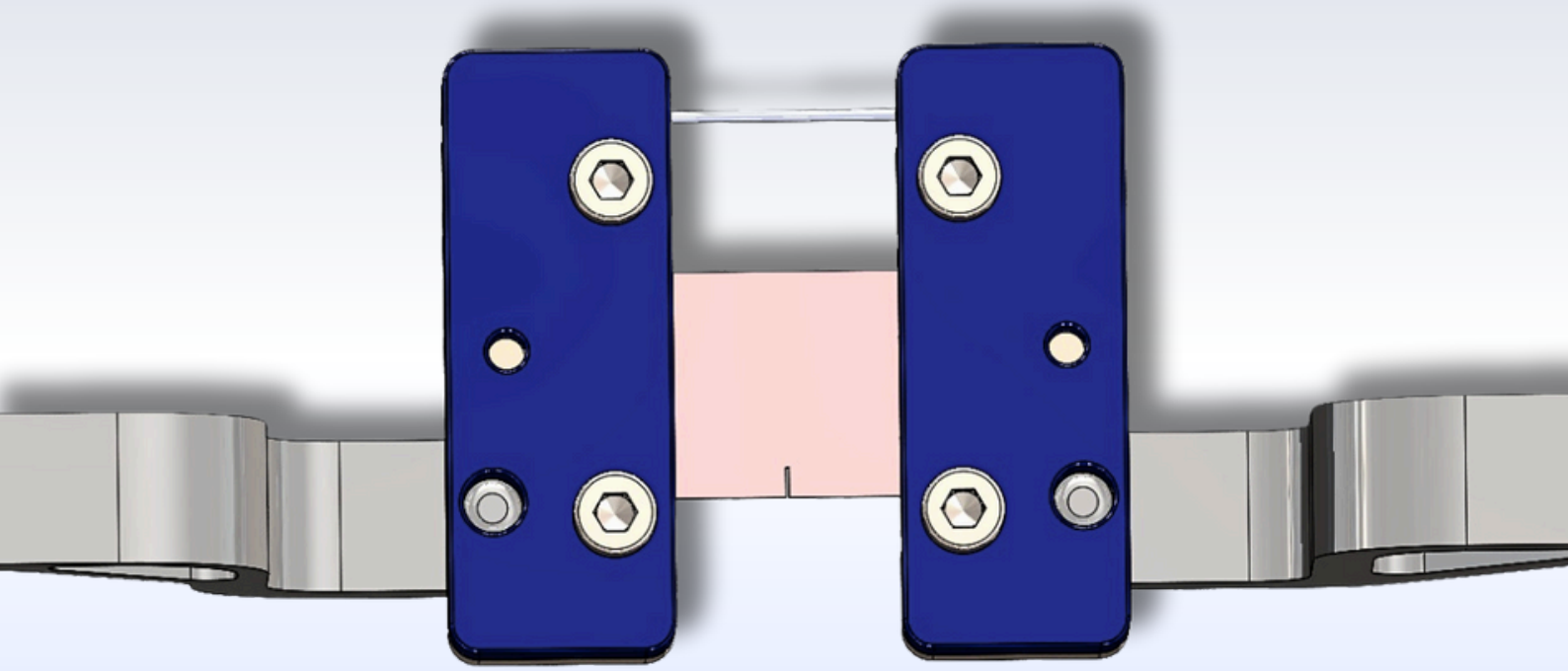

Juke de Planque
MSc BioMedical Engineering
Delft University of Technology
10 July 2025

Rupture Behavior Characterization of Healthy Porcine Aorta Using the SymconCT Setup

by

Juke de Planque

in partial fulfilment of the requirements of
Master of Science in Biomedical Engineering
track medical devices
at the Delft University of Technology,
to be defended publicly on Friday 11 July 2025

Main Supervisor:	Dr. ir. A. Akyildiz
Daily Supervisor:	S. Dreesen
Thesis committee:	Dr. ir. A. Akyildiz
	Dr. ir. N. Tümer
Student number:	5652383

TU Delft

Preface

This thesis follows a different approach from the standard thesis structure. The main content is presented in the form of a journal-style paper. It is followed by an appendix containing background information and the complete experimental dataset. The appendix provides an explanation of the experimental methods that were used, along with an inventory of all results. This includes all experimental data used in the analyses, as well as results that were excluded from the study.

After completing my Bachelor's degree in Medicine, I decided not to pursue the traditional path of medical internships, as I did not see myself working as a doctor in the future. My Bachelor's thesis, which applied a mechanical engineering approach, sparked my interest in continuing with an engineering-focused master's program.
I transitioned into a bridging program for Biomedical Engineering and began the master's the following year. To explore career options in this new field, I deliberately chose an internship at a company that invests in healthcare technology. However, it quickly became clear that my interests lay in the application of biomedical engineering. During this period, Ali Akyildiz was my supervisor. Together, we explored several research opportunities in experimental research, which led me to complete my master's thesis at the Biomedical Engineering Department at the Erasmus MC in Rotterdam.
I would like to thank Ali Akyildiz and Silke Dreesen for providing me with the opportunity to do research at Erasmus MC. Their guidance and expertise added great value to the outcome of this thesis. I enjoyed my time at Erasmus and would also like to thank the entire Biomedical Engineering Department. I learned the fundamentals of experimental research and gained a broader understanding of vascular biomechanics beyond the focus of my project, especially through the various research presentations held within the department.
I would also like to thank my family and friends for supporting me in making the difficult decision to change my academic direction. I am very happy with the choice I made and proud to have completed the bridging program and nearly finished the master's degree.

Juke de Planque
Delft, July 2025

Contents

Rupture Behavior Characterization of Healthy Porcine Aorta Using the SymconCT Setup

***Abstract*—Background and Purpose: An aortic aneurysm is a localized and permanent dilation of the aortic wall that has a risk of rupture, which can lead to life-threatening consequences. Reliable predictors to assess rupture risk of aneurysms are currently lacking. Changes in the composition and organization of the aortic wall, as seen in aneurysmal tissue, may influence how the vessel responds to mechanical stress. Studying rupture characteristics in aneurysmal tissue with varying wall structures may, therefore, support the identification of more reliable indicators of rupture risk. This study aims to characterize the rupture behavior of healthy porcine aortic tissue using a custom-designed symmetry-constraint compact tension (SymconCT) test. The SymconCT setup is a modified version of a compact tension test specifically designed to analyze fracture behavior in soft biological tissues. Rupture behavior is evaluated under both longitudinal and circumferential tensile loading to assess mechanical response in different loading directions. Healthy porcine aortic tissue was chosen for testing the SymconCT setup before application in diseased human tissue due to its close anatomical similarity to the human aorta.**

Methods: The recently designed SymconCT test setup was developed for soft tissue rupture analysis. In this setup, rupture is initiated from a notch at a fixed location on the sample. To prevent buckling of the soft tissue during loading, the SymconCT incorporates a pre-straining beam opposite the notch, enabling controlled crack propagation. Eight healthy porcine aortic samples (five circumferential, three longitudinal) were tested under tensile loading in longitudinal or circumferential directions. Digital Image Correlation was used to evaluate the deformation field. Fracture behavior was characterized by ultimate stress, ultimate strain, strain at the crack tip, initiation energy, and dissipation. Crack trajectories were reconstructed based on maximal strain localization.

Results: Orientation-dependent fracture behavior was observed. Circumferential samples showed higher ultimate stress (289.2 ± 58.4 kPa vs. 184.6 ± 29.8 kPa) and ultimate strain (157 ± 9.1% vs. 111 ± 42.4%) compared to longitudinal samples. Initiation energy was almost twice as high in circumferential samples (21.78 ± 5.99 mJ/mm vs. 11.04 ± 4.12 mJ/mm). Energy dissipation was also higher in circumferential samples (1.34 ± 0.42 mJ/mm² vs. 0.98 ± 0.12 mJ/mm²). Longitudinal samples fractured in relatively straight pathways, whereas circumferential samples exhibited more zigzagging fracture paths.

Conclusion: The custom-designed SymconCT setup successfully captured rupture behavior in healthy porcine aorta tissue. It facilitated a stable rupture progression, demonstrating the method's capability of soft tissue fracture testing. The results reveal orientation-dependent fracture behavior of healthy arterial tissue, with increased resistance observed when samples were loaded along the circumferential direction. This study design provides a foundation for future studies into rupture risks in aneurysmal tissue with disrupted fiber architectures.

I. Introduction

An aortic aneurysm is a localized and permanent dilation of the aortic wall that can bulge to twice its normal diameter [1]–[3]. They are generally classified as saccular, where the bulge appears on one side of the aorta, or fusiform, where the aorta expands evenly around its diameter (Figure 1). The incidence rises with age, affecting approximately 5% of people over 60 years old. Aneurysms typically develop as a consequence of other diseases. Common causes include atherosclerosis, genetic connective tissue disorders, infections, and traumatic injury. These conditions affect the arterial wall by disrupting the balance between synthesis and breakdown of extracellular matrix components [1], [4]. As a consequence, the structural changes cause dilation and progressive weakening of the vessel wall. This increases the risk of rupture, which could result in life-threatening bleeding. [1], [2].

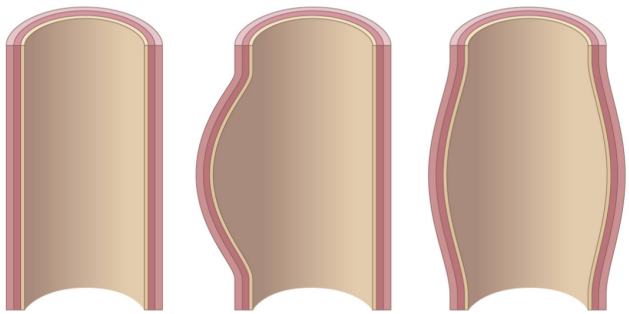

Fig. 1. Different types of aneurysms. Left: a healthy artery. Middle: a saccular aneurysm, showing a localized bulge on one side of the artery wall. Right: a fusiform aneurysm, where the arterial wall dilates around the entire circumference. [1]

Early identification of an aortic aneurysm at risk of rupture is crucial. Elective surgical repair of unruptured aneurysms carries a relatively low mortality rate of 5%. However, emergency surgery following rupture is associated with a mortality rate exceeding 50% [2]. Therefore, identifying the conditions under which an aneurysm becomes prone to rupture is essential for enabling timely intervention.

Currently, aneurysm size is the primary indication for intervention [2]–[4]. Dilations of 5.5 cm or larger are typically assessed for elective surgery. However, multiple studies report considerable variation in rupture rates across both small and large aneurysms [5], [6]. In addition, small aneurysms are also associated with a substantial number of ruptures [5]–[7]. These findings suggest that aneurysm size alone is not a

reliable predictor of rupture. Despite growing interest, research on how structural changes in the aneurysm wall influence its mechanical stability and rupture risk remains limited [5]. An improved understanding of how wall remodeling affects rupture behavior can add value to improving the risk assessment of aortic aneurysms.

The general architecture of blood vessels is similar throughout the cardiovascular system [1], [8]. A vessel wall consists of the intima, media, and adventitia layers, which together determine the vessel's mechanical properties. The intima is the innermost layer of the vessel wall. It consists of a thin sheet of endothelial cells attached to a basement membrane. Beneath the basement membrane lies a thin layer of subendothelial connective tissue, providing structural support and flexibility. The middle layer, the media, primarily contains smooth muscle cells, elastin, and collagen fibers. The smooth muscle cells regulate vessel diameter through contraction and relaxation. Elastin enables the vessel to stretch and recoil with pulsatile pressure, contributing to vascular compliance. In contrast, collagen fibers provide tensile strength, preventing vessels from overexpanding. The outermost layer is the adventitia layer. It contains connective tissue, primarily collagen, nerve fibers, and small blood vessels. The adventitia provides additional structural support and ensures the delivery of nutrients to the outer regions of the vessel wall [1], [8].

The arrangement and thickness of the vascular layers vary based on the specialization of blood vessels. For example, the aorta contains a high concentration of elastin between the smooth muscle cells in the media. This arrangement allows the aorta to resist large pulsatile forces. In contrast, veins have thinner, less organized walls and larger diameters. Their structure facilitates a larger blood storage capacity to return to the heart [1], [8].

Moreover, the structural organization of the vessel wall gives rise to specific mechanical behavior. Healthy arterial tissue exhibits anisotropy, which refers to the direction-dependent mechanical response of the vessel wall [9], [10].

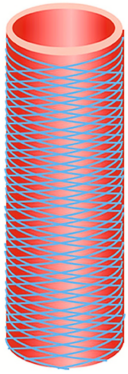

Fig. 2. Illustration of the predominant circumferential orientation of collagen fibers in the arterial media. Two fiber families are symmetrically arranged in a helical pattern at approximately 30° relative to the vessel's circumferential axis. This collagen orientation contributes to the anisotropic mechanical behavior of the arterial wall, enhancing stiffness in the circumferential direction [11].

This property arises from the organized structure of collagen fibers in the arterial media, which form two helical fiber families oriented at small angle relative to the vessel's circumferential axis. This structured arrangement gives rise to a predominantly circumferential orientation of the collagen fibers (Figure 2). Consequently, the structural organization creates greater stiffness in the circumferential direction than in other directions, enabling the vessel to better resist circumferential forces such as blood pressure [9]–[13].

Changes in the composition and organization of the aortic wall, as seen in aneurysmal tissue, may influence how the vessel responds to mechanical stress. Studying rupture characteristics across aneurysmal tissue with varying wall structures may, therefore, support the development of improved risk assessment strategies.

This study aims to characterize the rupture behavior of healthy porcine aortic tissue using a customized version of the symmetry-constraint compact tension (SymconCT) test. The SymconCT setup is specifically designed for analyzing fracture behavior in soft biological tissues [14]. The rupture behavior is evaluated under longitudinal and circumferential tensile loading to assess the mechanical behavior under different loading directions. Healthy porcine tissue was used to validate the experimental setup before application to diseased human samples. Porcine aorta closely resembles human aortic tissue in size and composition [15]. By evaluating the ultimate stress, strain, fracture energy, and rupture propagation patterns in healthy tissue, this study provides a reference for future studies into aneurysmal wall rupture across different structural architectures.

II. Methodology

A. Experimental Setup

The fracture properties of vascular tissue were assessed using the SymconCT test design developed by Alloisio et al. [14]. This setup is a modified version of the compact tension test, a method commonly used in materials science to investigate fracture mechanics.

In a standard compact tension test, a tensile force is applied to a notched specimen, causing a crack to initiate at the notch and propagate toward the opposite end of the material [14]–[16]. During the tests, stress is concentrated at the notch, ensuring that the crack initiates at a fixed location and enabling controlled crack propagation from that point. It allows for the assessment of mechanical behavior both before crack initiation and during crack propagation, offering insight into the material's resistance to rupture initiation and propagation. However, this approach is not suitable for soft biological tissues. Due to their low bending stiffness, soft tissues tend to buckle out-of-plane in the region opposite to the notch when placed under tensile loading. This prevents stress from being concentrated at the notch tip, resulting in unstable crack propagation [14].

The SymconCT design overcomes this issue by incorporating an elastic beam opposite to the notch. The customized setup developed for this study is shown in Figure 3. It consisted

of arms for applying tensile load, clamps for securing the sample, and an elastic beam. The beam introduces an outward bending moment on the clamps, slightly stretching the tissue opposite the notch. Tensile load was applied close to the notch, ensuring that stress was concentrated at this location. The beam stabilized the back of the tissue during loading, enabling controlled fracture propagation from the notch toward the end of the sample. A detailed description of the SymconCT setup is provided in Appendix A.

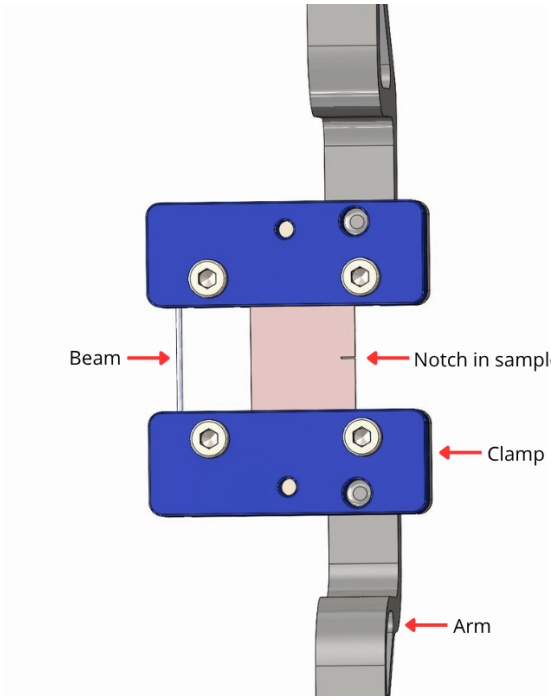

Fig. 3. Top view of the custom-designed symconCT setup. The setup includes arms, connected to the biaxial testing machine, for applying tensile load. The clamps secure the tissue sample, with the beam positioned opposite to the notch.

The fracture tests were performed using a biaxial testing machine, the Biotester 5000 (CellScale, Canada), equipped with the custom-designed SymconCT setup. For these experiments, two inline actuators and a 10 N load cell were used to apply and record tensile loading, resulting in an uniaxial test configuration. The aluminum arms of the SymconCT setup were mounted onto the biaxial testing machine and connected to the aluminum clamps. The beams were made from spring steel wire, with a length of 34 mm, a diameter of 0.8 mm, and a bending stiffness between 1800 and 2000 N/mm². To mimic physiological conditions, the clamps were submerged in a temperature-controlled fluid bath filled with phosphate-buffered saline (PBS) maintained at 37 ± 1°C.
Figure 4 shows the complete experimental setup, which includes the SymconCT setup mounted on the biaxial testing machine, along with a digital image correlation (DIC) and ultrasound system. The DIC system captured two-dimensional (2D) surface displacements of the tissue using a high-speed camera and a blue light LED source. A detailed description of the DIC technique is provided in Appendix B. The ultrasound probe was used to assess tissue thickness. Force, displacement, and time data were recorded using CellScale software. Strain data were processed using DaVis software (LaVision, Germany).

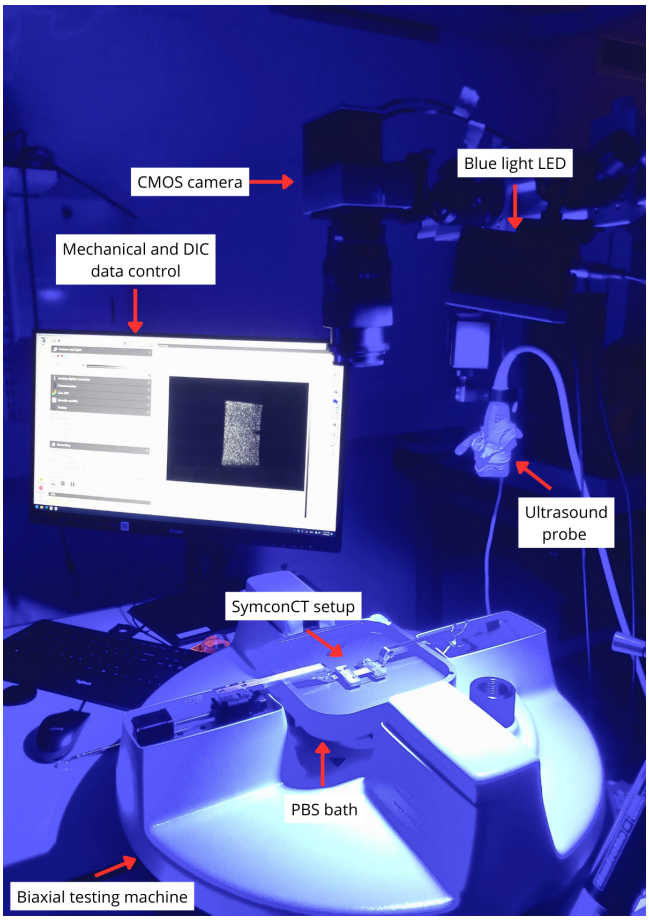

Fig. 4. Experimental setup at Erasmus MC laboratory. The biaxial testing machine contains the symconCT setup within a PBS bath. A tripod above the biaxial testing machine includes a CMOS camera, blue light LED, and ultrasound probe. Mechanical loading and DIC measurements are controlled via the connected computer system.

B. Tissue Preparation

The porcine aortas were collected from a slaughterhouse on 25 June 2024 and stored in PBS at -80 ° C. On the day of testing, the aortas were defrosted in a PBS bath at room temperature. Loose connective tissue was removed, and the adventitia layer was carefully dissected using forceps and surgical scissors. The remaining aorta tissue, consisting of the intima and media layers, was cut into 30 by 11 mm samples using a customized cutting device, shown in Figure 5a. A 2 mm notch was made using a scalpel, and its dimensions were verified with a ruler. Sixteen aortic samples were prepared over two days, with four longitudinal samples and four circumferential samples tested each day. Longitudinal samples were cut with the long side of the sample aligning with the length of the vessel, following the direction of blood flow.

In circumferential samples, the long side followed the vessel's circumference. The 2 mm notch was introduced at the center of one of the long edges. During tensile testing, each sample was pulled along its long edge, causing the rupture to propagate from the notch toward the opposite side. As a result, rupture in longitudinal samples was induced in the direction around the vessel wall, while in circumferential samples it was induced along the vessel's length.

To enable DIC analysis, a randomized fluorescent orange dye speckle pattern was applied to the intima surface using an airbrush.

Once prepared, the sample was mounted within the aluminum clamps. A custom clamp holder, shown in Figure 5b, was used to position the sample into the clamps at a fixed distance of 15 mm. The inside of the clamps was lined with sandpaper to prevent sample slippage during testing.

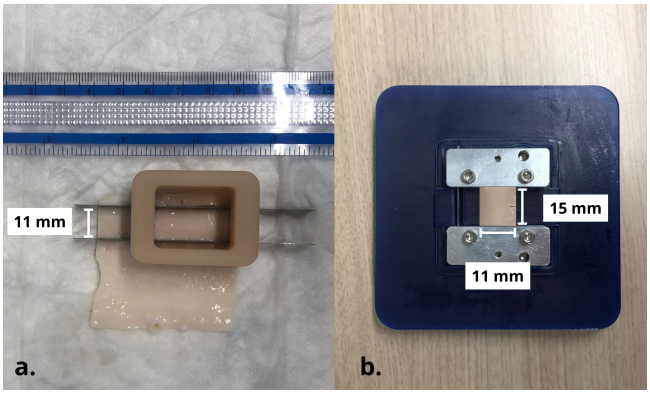

Fig. 5. (a) Customized cutting device used to cut aortic samples evenly. Razor blades were set in the cutting frame at an 11 mm distance to ensure a constant sample width. The remaining 30 mm edges and the 2 mm notch were cut manually using a scalpel and ruler. (b) Custom clamp holder designed to secure the aluminum clamps at a fixed 15 mm length.

C. Testing Protocol

Before each fracture test, residual forces from the setup or previous measurements were removed by zeroing the load cells. This was done with the clamps mounted in the biaxial testing machine while submerged in the PBS bath. The aortic tissue was not yet placed in the setup. After this step, a sample was prepared, inserted into the clamps, mounted in the setup, and submerged in the PBS bath. The beam was inserted to pre-strain the sample and secured using an Allen key.

Before the fracture testing, an ultrasound scan was performed to assess tissue thickness. The ultrasound probe captured cross-sectional images of the sample.

Following ultrasound imaging, fracture testing was initiated using a displacement-controlled protocol. The clamps were separated by 150% of the initial distance, increasing from 15 mm to 37.5 mm over 150 seconds, followed by a 10-second recovery phase during which they returned to their original position. Figure 6 shows the raw force-time curve of the second circumferential sample (C2) that was tested, illustrating the applied protocol. Throughout testing, both data and images were recorded at a sampling rate of 10 Hz.

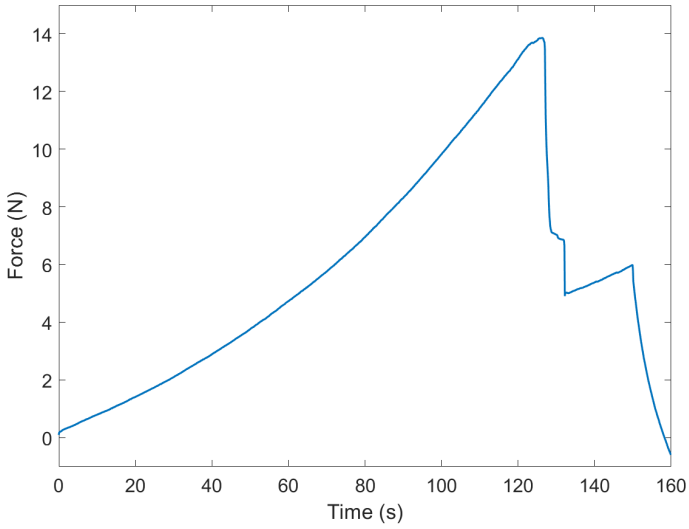

Fig. 6. Raw force-time curve of sample C2 illustrating the fracture test protocol. The curve shows a gradual increase in force during the loading phase (0-150 s). A sharp drop at approximately 123 s marks the onset of tissue fracture, which progressed until complete rupture at around 130 s. Clamp displacement continued after rupture, with the following increase in force reflecting the mechanical response of the beam to further clamp displacement. The unloading phase begins at 150 s, indicated by the decline in force during the 10-second recovery period.

When samples reached complete rupture, the beam took over and carried the remaining mechanical load throughout the rest of the test. To account for the mechanical contribution of the beam, a separate beam-only test was performed at the end of each testing day using the same experimental setup but without mounting a tissue sample. First, the load cells were zeroed following the same protocol used in the fracture tests. After that, the mechanical behavior of the beam was assessed. Ten loading-unloading cycles were applied during the beam tests, following the same protocol used in the fracture tests.

D. Beam Characterization

To isolate the fracture behavior of the aortic samples from the mechanical contribution of the beam, correction of the raw force-displacement data was performed. Sample C2 is presented as a representative example to illustrate the correction process applied to all samples. Figure 7 shows the raw force-displacement data that was captured during 150% clamp displacement and the return to the starting position. The measured force in this raw force-displacement curve, marked as F_r, consists of the sample force F_s and the beam force F_b:

$$F_r = F_s + F_b \tag{1}$$

The F_r increases until a sharp drop indicates the start of rupture. A second drop follows, representing continued tearing and eventual tissue failure. The following increase in force represents the mechanical behavior of the beam, corresponding to F_b.

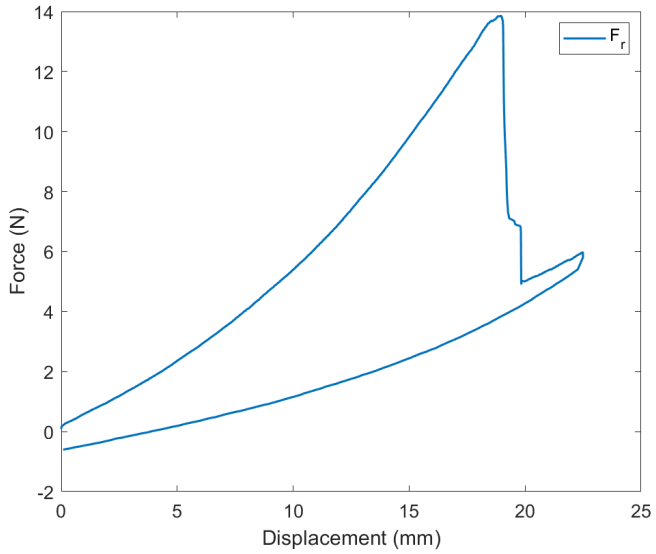

Fig. 7. Raw force–displacement curve of C2. The F_r increases until a sharp drop occurs at approximately 19 mm, indicating the onset of rupture. A second drop follows, representing continued tearing and eventual tissue failure. The following rise in force, from around 20 mm to 22.5 mm, represents the mechanical behavior of the beam, corresponding to F_b.

Beam-only tests were performed at the end of each testing day to characterize the contribution of the pre-straining beam. Figure 8 shows ten repeated loading-unloading cycles conducted under the same displacement protocol as the tissue tests. The first cycle differs from the others, potentially due to preconditioning effects. In the following cycles, the beam settled into a stable configuration within the setup, and the mechanical response became more consistent. The curves increasingly show repeatable behavior with constant hysteresis. Therefore, the eighth cycle was selected as the reference for F_b subtraction, being unaffected by early-cycle variability.

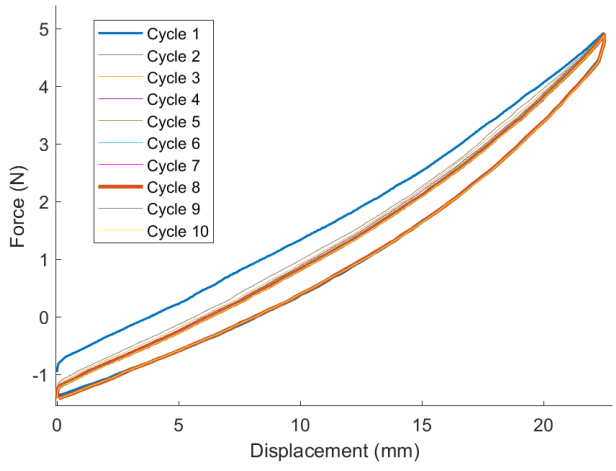

Fig. 8. Force–displacement curves from ten successive beam-only loading-unloading cycles. The first cycle (blue) varies due to preconditioning effects. The following cycles exhibit repetitive mechanical behavior. Beam cycle 8 (red) was selected for correction and subtraction from the sample curve.

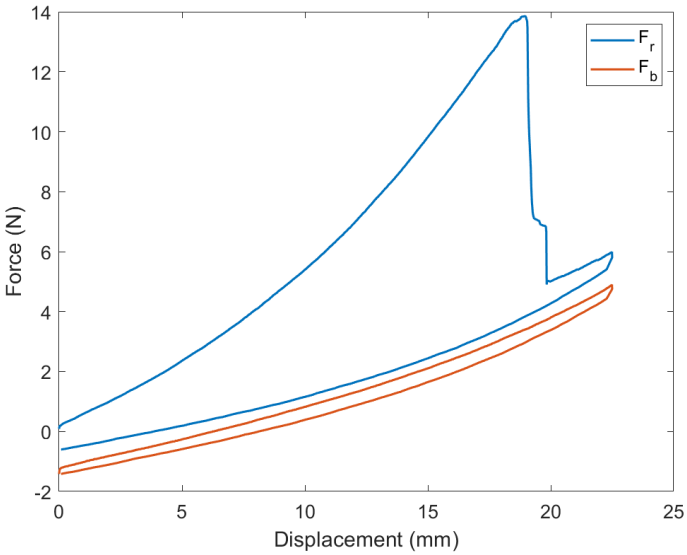

Fig. 9. The raw force-displacement curve of C2 plotted in blue alongside beam cycle 8, shown in red. A vertical offset is visible due to differences in the load cell zeroing conditions between the sample and beam tests.

Figure 9 shows the force-displacement curve of beam cycle 8 plotted alongside the raw force-displacement curve of C2. The graph reveals a vertical offset between the two curves, resulting from differences in the initial loading conditions. In the sample test, the load cells were zeroed before the tissue was inserted, and the beam was tightened. Inserting the beam caused the clamps to shift slightly outward, generating a compressive force on the actuator arms that was registered by the load cells as a small negative preload. The tissue resisted this outward force, generating a positive counterforce. In contrast, during the beam-only test, no tissue was present to resist the outward motion of the clamps. As a result, the compressive force introduced by the beam revealed a negative initial force at the start of the beam curve.

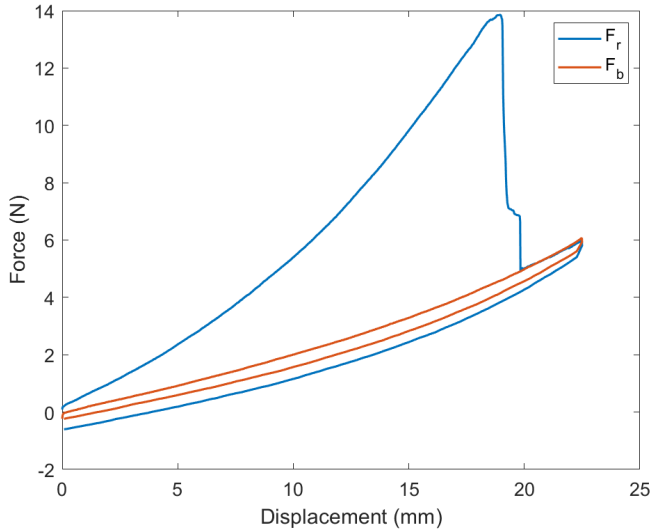

Fig. 10. Raw force–displacement curve of C2 plotted alongside beam cycle 8.5, after applying vertical offset correction.

To isolate the mechanical behavior of the tissue, F_b was subtracted from F_r. To enable subtraction, the two curves were aligned by applying a vertical shift to the beam curve, as shown in Figure 10. The offset was set at the moment of a complete rupture, where tissue ruptures and the beam takes over the force-displacement response.

After this correction, F_b was subtracted from F_r. The resulting force–displacement curve, containing only the F_s, is shown in Figure 11. This curve shows the isolated mechanical response of the tissue during loading and rupture.

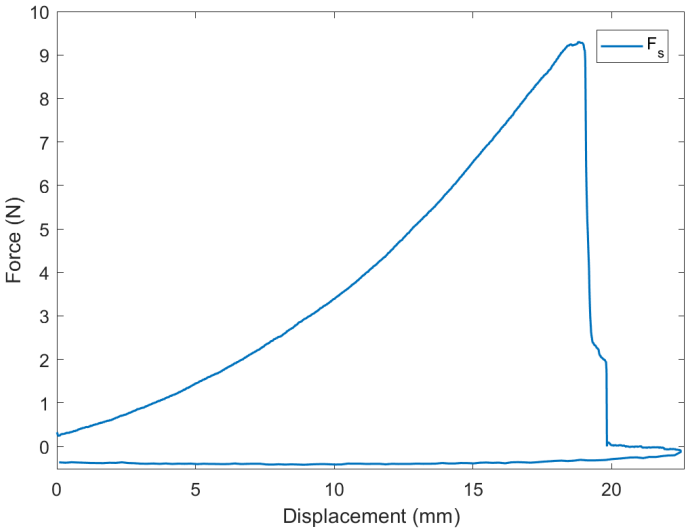

Fig. 11. The force–displacement curve of sample C2 after subtraction of the beam force. The curve shows the fracture behavior of C2 alone.

E. Data Processing

The mechanical properties of the aorta samples were assessed using the force-displacement and strain data that was obtained during fracture testing. All data processing and calculations were performed using MATLAB and DaVis software.

Figure 12 presents an example of a force-displacement curve of sample C2 that shows only the loading phase. The mechanical response of the beam has been removed to reveal the rupture behavior of the tissue. Figure 13 shows the corresponding DIC images of sample C2, visualizing the progression of a fracture test. The time points highlighted in the curve align with the time points shown in the DIC images. The force-displacement curve can be divided into the pre-fracture and fracture phases. The pre-fracture phase, from T0 to T1, represents the loading and deformation of the sample before rupture. The fracture phase, spanning T1 to T4, captures the process of crack propagation leading to complete rupture. Initial tearing begins between T1 and T2, followed by a slowdown in crack progression from T2 to T3. Finally, a sudden change in crack direction, as observed in the DIC images shown Figure 13 between the T3 and T4, led to rapid crack propagation, resulting in rupture at T4.

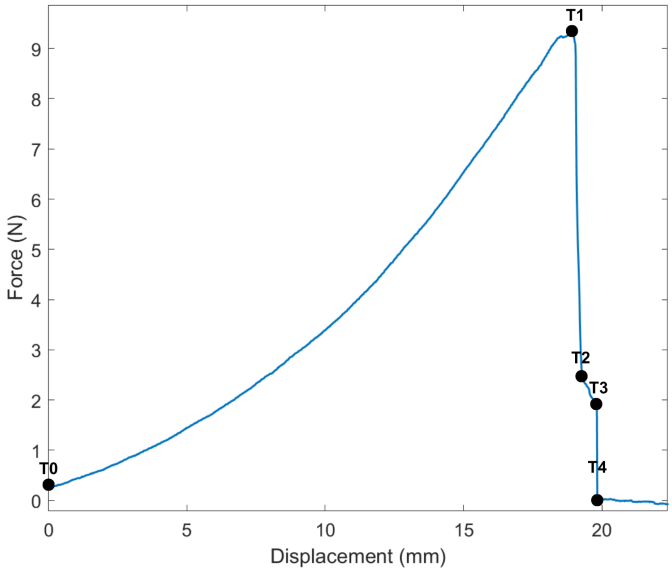

Fig. 12. Force–displacement curve of sample C2 undergoing fracture. The curve displays the loading phase only. Beam response has been subtracted to isolate the mechanical behavior of the tissue. The time points mark deformation (T0-T1), crack initiation (T1), crack progression (T1-T4), and rupture (T4).

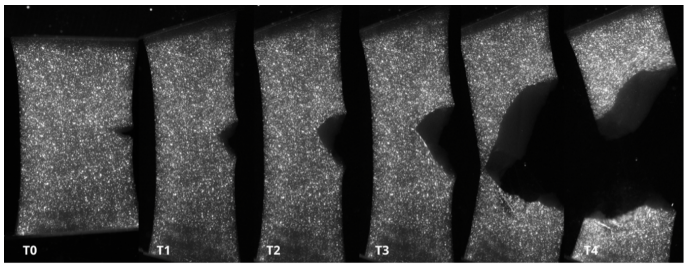

Fig. 13. DIC images of the sample C2 at time points T0–T4, corresponding to the force-displacement curve in Figure 12. The images capture the progression of rupture throughout the fracture process.

The highest stress the tissue could withstand during testing was determined by calculating the ultimate engineering stress (σ_u). This value was calculated using the following equation:

$$\sigma_u = \frac{F_u}{A_i} \tag{2}$$

F_u is the highest force recorded by the load cell during the test. A_i is the initial cross-sectional area of the tissue. This area was the product of the sample thickness and width, assessed by ultrasound in the region directly behind the notch.

In this study, ultimate strain (ε_u) is defined as the maximal principal strain measured just before visible crack initiation. This definition was chosen because it was impossible to determine the exact peak strain in the fracture tests. The 2D DIC system could not accurately capture out-of-plane displacements near the crack tip, resulting in noisy strain data in that region. As an alternative, the DIC image that is captured immediately before visible crack initiation was

manually selected in DaVis and used as the reference point for calculating the ultimate strain. This image represents the highest deformation the tissue can withstand before rupture, offering a consistent comparison point across all samples. This timepoint, labeled T1 in Figure 12, corresponds to the moment of maximum load during testing.
In addition to measuring ultimate strain, an average strain value (ε_a) was calculated from the same image within a fixed circular region that was centered around the notch. Its dimensions and position were held constant across all samples.

Fracture path patterns and lengths were estimated by analyzing the DIC data. The reconstruction method was based on the assumption that cracks preferentially propagate through regions of highest strain, aligning with studies on failure models in soft biological tissues [14], [20]. To identify these regions, the highest value of maximal principal strain, recorded at each pixel across all DIC frames, was extracted. A cumulative heat map was created from these values, highlighting the most deformed regions of the tissue surface. An example of a cumulative heat map is shown in Figure 17. Accordingly, the crack path was formed by interpolating a line through the data points that contained the highest strain values.
The crack path length was calculated by converting pixel measurements from the DIC images to millimeters using a calibration based on the known physical size of each sample (11 mm × 30 mm). Figure 18 shows an example of a reconstructed fracture path.

Fracture energy was calculated to measure the resistance of the tissue to fracture under tensile loading. It can be divided into initial energy and propagation energy [14], [21]. The initial energy corresponds to the work required to initiate crack formation. It is calculated by integrating the applied force (F) over the clamp displacement (U), from the start of loading (U_0) to the point of visible crack initiation (U_c). This is the area identified underneath the force-displacement curve from time point T0 to T1 in Figure 12.

$$W_i = \int_{U_0}^{U_c} F dU \tag{3}$$

To account for differences in sample thickness, the initial energy was normalized by the thickness (T) of each sample, producing (W_i^*) a thickness-independent measure of the initial energy:

$$W_i^* = \frac{W_i}{T} \tag{4}$$

The propagation energy represents the energy required to propagate a crack through the sample, from initiation to complete rupture. This corresponds to phases T1 to T4 in Figure 12. To account for differences in crack path lengths between samples, propagation energy was calculated by integrating the applied force (F) over the fracture path length (L). Accordingly, propagation energy was determined from the reconstructed force–fracture path curves. The integration begins at L_0, the point at which rupture initiates, and continues until L_f, marking complete rupture, as shown in the following equation:

$$W_p = \int_{L_0}^{L_f} F dL \tag{5}$$

The propagation energy was also normalized to account for variations in sample thickness. Additionally, differences in the lengths of the fracture paths were taken into account in the normalization, resulting in the dissipated energy per unit area (D) of the fractured sample:

$$D = \frac{W_p}{T \cdot L} \tag{6}$$

III. Results

From the 16 aortic samples that were tested, the fracture behavior of 9 was analyzed. The remaining 7 samples were excluded due to incomplete rupture or setup-related artifacts. Appendix C contains a detailed evaluation of the excluded samples.
The data analysis of sample C2 is discussed in detail below to illustrate how all results were obtained. A complete inventory of the analyses for the remaining samples is provided in Appendix D.

A. Ultimate engineering stress of sample C2

The ultimate engineering stress of sample C2 was calculated using the corrected force-displacement curve (Figure 11), which shows the fracture behavior of the tissue alone. The force data from this curve was divided by the sample's cross-sectional area (27.16 mm²), generating an engineering stress–displacement curve. The peak of this curve, shown in Figure 14, corresponds to an ultimate engineering stress of 342.6 kPa.

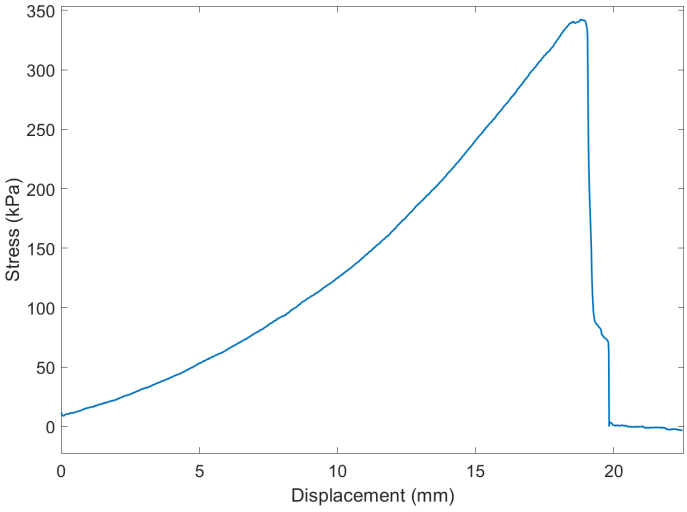

Fig. 14. Engineering stress–displacement curve of circumferential sample 2. The peak of the curve corresponds to an ultimate engineering stress of 342.6 kPa. The stress increases until a sharp drop indicates the start of rupture. A second drop follows, representing continued tearing and eventual tissue failure.

B. Strain analysis of sample C2

To assess the ultimate strain and average strain around the crack tip, the DIC image immediately preceding visible crack initiation was selected and processed in MATLAB. Figure 15 shows the resulting heatmap of maximal principal strain per pixel across the tissue surface. Elevated strain values are concentrated around the notch, where rupture is initiated. The highest local strain measured in this image was 156%, representing the ultimate strain measured in the sample. Noisy data points were identified and excluded before analysis.

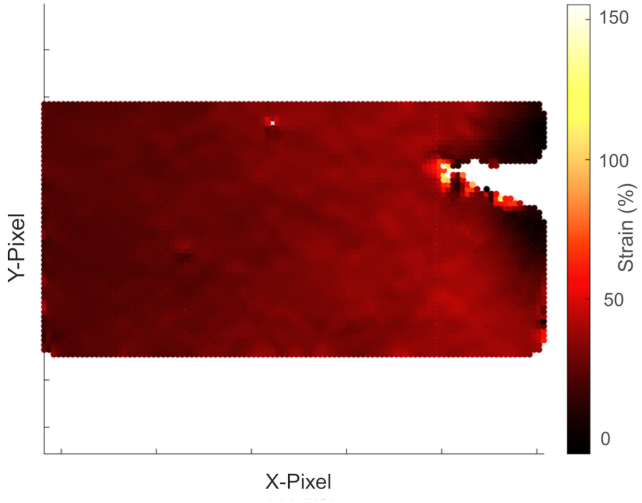

Fig. 15. Heatmap of maximal principal strain across the sample surface, generated from the DIC image immediately before crack initiation. Strain is expressed per pixel. Yellow areas indicate high strain, while red areas represent lower strain. The ultimate strain measured in this image is 156%.

The local deformation around the notch was assessed by averaging the strain within a circular region centered at the notch. Figure 16 shows a heatmap of the principal strain distribution within this region. The average principal strain was 30.9%.

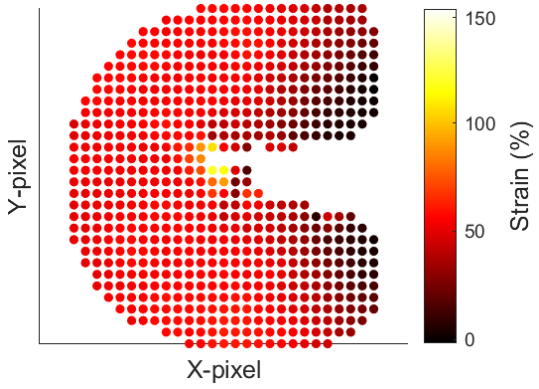

Fig. 16. Strain heatmap of the circular region surrounding the notch. Each circle represents a pixel where maximal principal strain was measured. Yellow pixels indicate areas of high local strain, while red show lower strain values. The average maximal principal strain within this region was 30.9%.

C. Fracture path reconstruction of sample C2

To reconstruct the fracture path of Sample C2, the highest principal strain values per pixel were identified across all recorded frames. These values were used to generate a cumulative heatmap, shown in Figure 17, highlighting the most deformed regions of the tissue surface.
The high-strain pattern extends from the initial 2 mm notch toward the posterior edge, outlining the route of crack propagation.

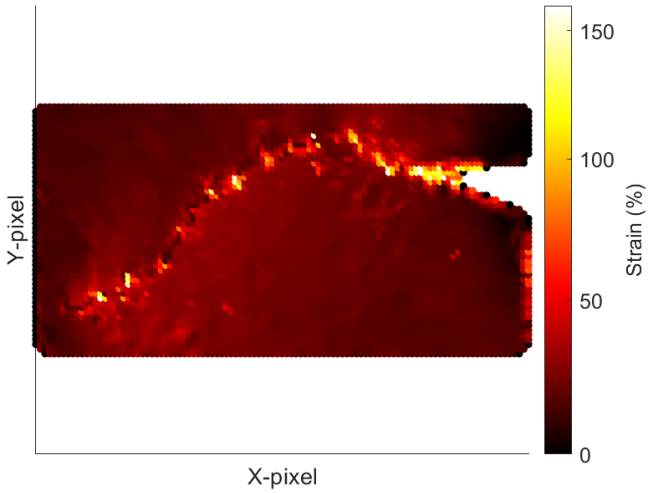

Fig. 17. Cumulative heatmap of maximal principal strain values across the surface of sample C2. Based on the DIC analysis, the map shows the highest strain value recorded at each pixel throughout the fracture test. Yellow areas indicate regions of high strain, while red areas represent lower strain. The curved pattern of elevated strain illustrates the fracture route across the tissue surface.

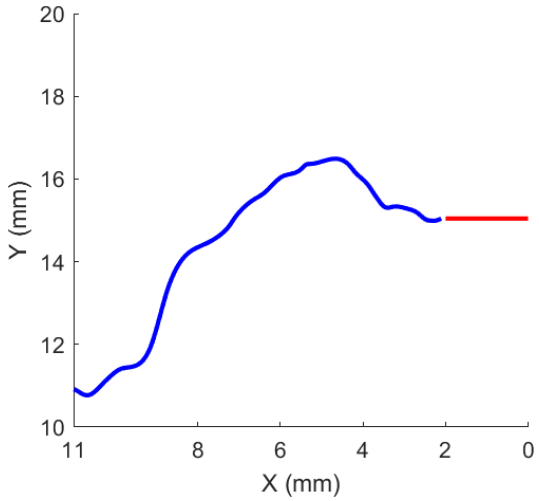

Fig. 18. Reconstructed fracture path of C2. The graph shows a close-up of the central region where the rupture occurred. The notch, positioned at the midpoint of the sample (15 mm), is marked in red. To match the orientation used in the DIC images, the x-axis is reversed. Fracture initiates at the notch and propagates leftward along the estimated trajectory, marked in blue. The total reconstructed crack path length was 16.84 mm.

The fracture path was estimated by interpolating a curve through the high-strain region. The reconstructed path, shown

in Figure 18, was 16.84 mm. The interpolated fracture paths were visually confirmed against the DIC image sequences to ensure they aligned with the observed fracture path.

D. Initial and propagation energy of sample C2

The initial energy was calculated by integrating the corrected force-displacement curve from the start of clamp displacement up to the point of visible tissue rupture (Figure 19). The total mechanical work required to initiate rupture was 70.2 mJ. Using the sample's thickness of 2.39 mm, the normalized initial energy was 29.4 mJ/mm.

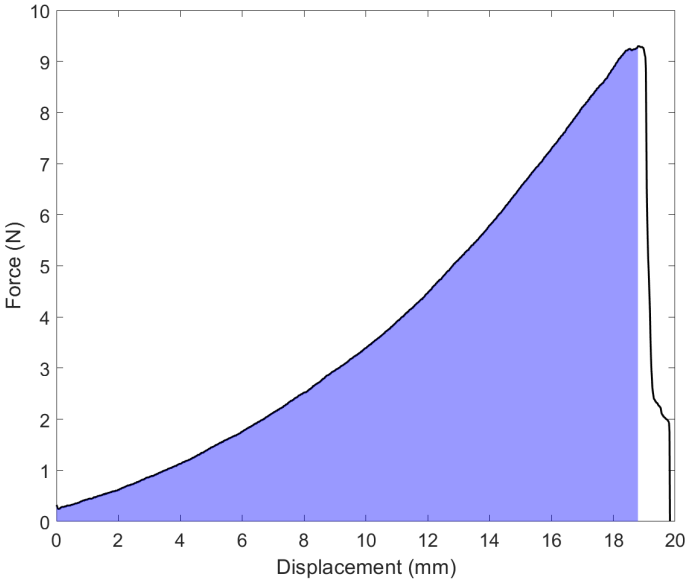

Fig. 19. Calculation of the initial energy. The blue area under the corrected force-displacement curve represents the mechanical work required to initiate rupture. The curve is integrated from the start of the test up to the point of visible crack formation. The total initial energy was 70.2 mJ, corresponding to a normalized inital energy of 29.4 mJ/mm.

The propagation energy was calculated from a reconstructed force–fracture path curve. The curve was generated from the force-time curve and a reconstructed fracture path–time curve, aligning both datasets to common time points (Appendix D). The resulting force–fracture path curve is shown in Figure 20, where the blue area represents the mechanical work required to propagate the crack from initiation to complete rupture.
The dissipation curve begins at * on the x-axis, with the zero point aligned to the onset of fracture. This shift ensures that the x-axis represents the fracture path length from the moment of crack initiation. The vertical point corresponding to zero on the x-axis marks the highest force measured during testing. It marks the start of tissue rupture. From this point onward, the force decreases as the crack propagates through the tissue until it reaches complete rupture. The part of the curve between * and 0 represents the initial loading phase, during which force is applied to the tissue while no fracture occurs.
The calculated propagation energy was 31.2 mJ, corresponding to a dissipation of 0.78 mJ/mm^2.

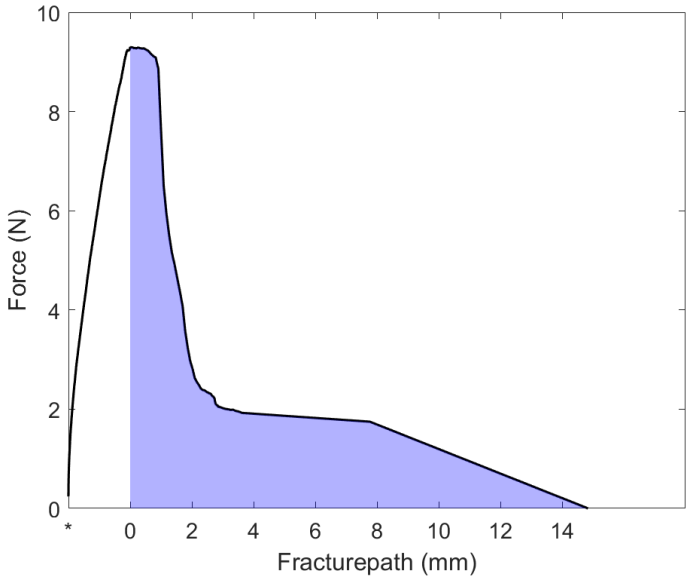

Fig. 20. Calculation of the propagation energy. The blue area under the force–fracture path curve represents the mechanical work required to propagate the crack through the sample. The total propagation energy was 31.2 mJ, corresponding to a dissipation of 0.78 mJ/mm^2.

E. Summary of results across all samples

The primary outcomes of the fracture tests are summarized in Table 1. Longitudinal samples are denoted by L and circumferential samples by C. The accompanying number refers to the order in which the measurements were performed.
Strain and propagation energy results could not be obtained for samples L3 and C4, as the intima and media layers ruptured separately during fracture testing. This delamination interfered with the accuracy of the DIC analysis, as the speckle pattern was applied to the intima layer. The tracked deformation no longer reflected the mechanical behavior of the underlying media, which was responsible for bearing the majority of the load. Nonetheless, the force-displacement data were not affected by the delamination. DIC images showing the delamination are provided in the individual appendix subsections.
Fracture path estimations revealed differences between the longitudinal and circumferential samples. Figure 21 shows the reconstructed fracture paths for all samples. Longitudinal samples showed relatively straight paths, while circumferential samples followed more irregular zigzagging trajectories.
Figures 22 to 27 present the mean values of the fracture test outcomes together with their standard deviations (SD). These values allow for a comparison of the fracture behavior between both longitudinal and circumferential samples. Ultimate stress, ultimate strain, average strain, fracture path length, initiation energy, and energy dissipation were all higher in the circumferential samples.

TABLE I
SUMMARY OF FRACTURE TEST RESULTS DERIVED FROM THE SYMMETRY-CONSTRAINT COMPACT TENSION TESTS

Sample	Area (mm^2)	Ultimate Stress (kPa)	Ultimate Strain (%)	Average Strain (%)	Fracture Path Length (mm)	Initiation Energy (mJ/mm)	Propagation Energy (mJ/mm^2)
L2	19.81	181.5	141	24.7	12.13	7.83	0.89
L3	16.32	156.5				9.62	
L7	22.16	215.9	81	37.2	12.92	15.7	1.06
C1	23.78	281.4	149	35.5	16.07	14.3	1.5
C2	27.16	342.6	156	30.9	16.84	29.4	0.78
C3	23.73	335.4	170	33.2	14.43	24.8	1.77
C4	21.84	290.2				23.0	
C8	21.38	196.4	153	41.4	15.25	17.4	1.31

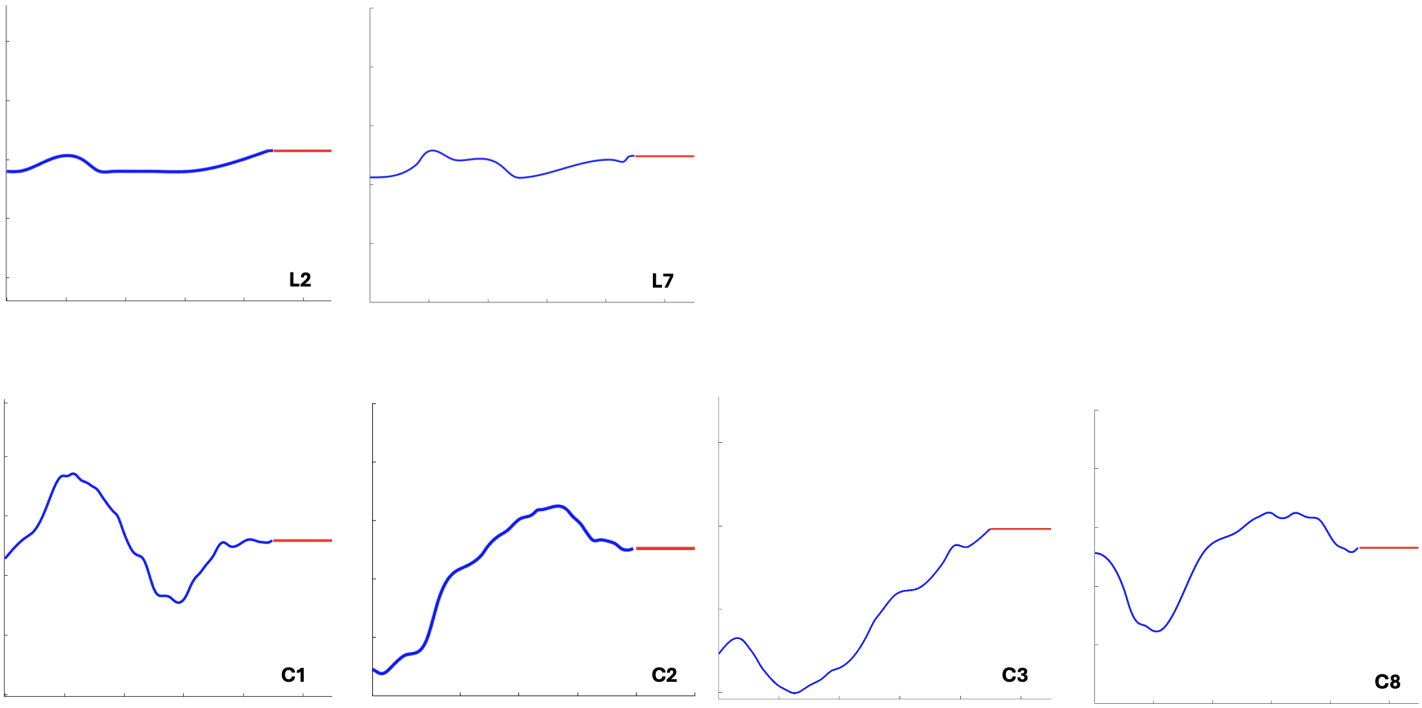

Fig. 21. Reconstructed fracture paths of all longitudinal and circumferential samples. Each plot shows the central rupture region of the sample, with the red segment indicating the initial 2 mm notch located at the midpoint. Longitudinal samples (top row) exhibit relatively straight fracture patterns. In contrast, circumferential samples (bottom row) show zigzagging trajectories. To match the DIC analysis orientation, x-axes are reversed. Fracture initiates at the notch and propagates leftward along the estimated trajectory, shown in blue.

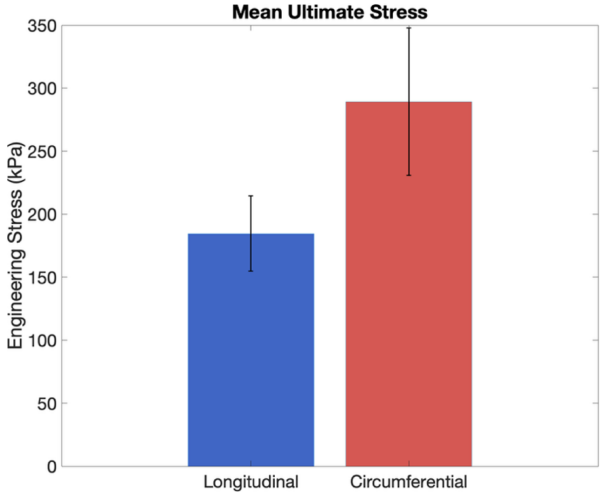

Fig. 22. Bar plot of mean ultimate engineering stress.
Longitudinal samples had a mean of 184.6 kPa (SD = 29.8).
Circumferential samples had a mean of 289.2 kPa (SD = 58.4).

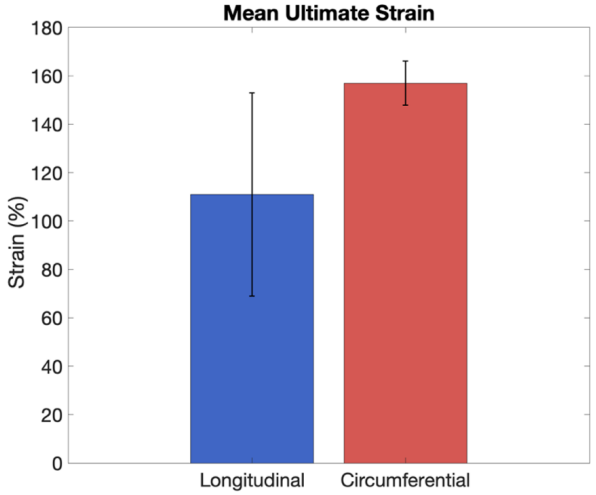

Fig. 23. Bar plot of mean ultimate strain.
Longitudinal samples had a mean of 111% (SD = 42%).
Circumferential samples had a mean of 157% (SD = 9.1%).

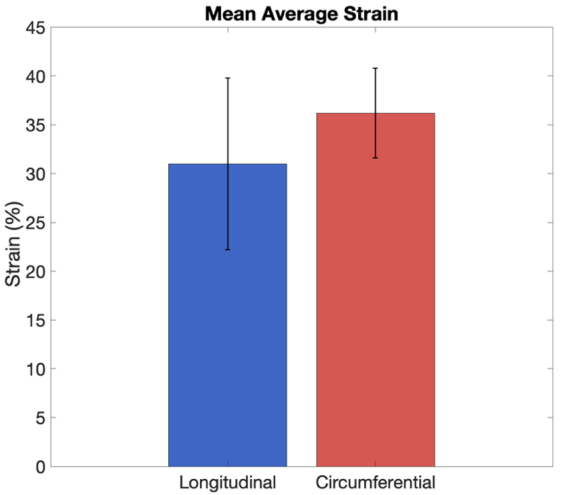

Fig. 24. Bar plot of mean average strain.
Longitudinal samples had a mean of 31.0% (SD = 8.8%).
Circumferential samples had a mean of 36.2% (SD = 4.6%).

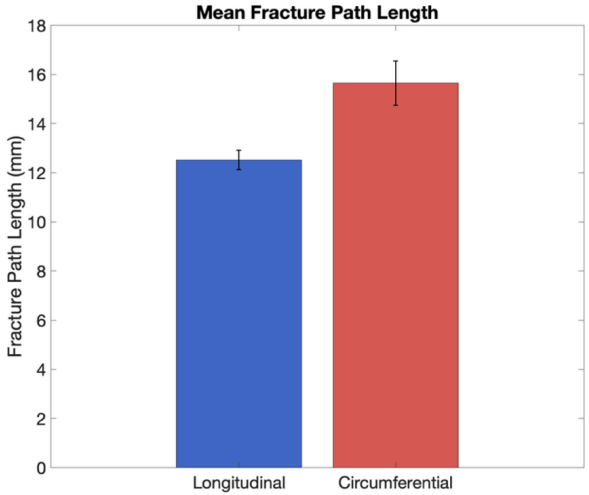

Fig. 25. Bar plot of mean fracture path length.
Longitudinal samples had a mean of 12.52 mm (SD = 0.39).
Circumferential samples had a mean of 15.65 mm (SD = 0.90).

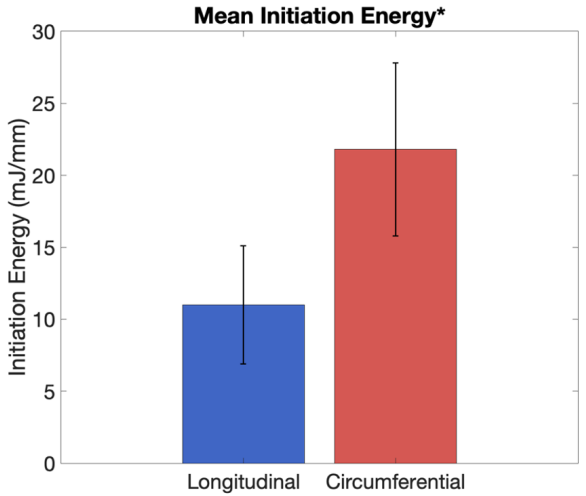

Fig. 26. Bar plot of mean initiation energy.
Longitudinal samples had a mean of 11.0 mJ/mm (SD = 4.1).
Circumferential samples had a mean of 21.8 mJ/mm (SD = 6.0).
*Normalized value of initiation energy.

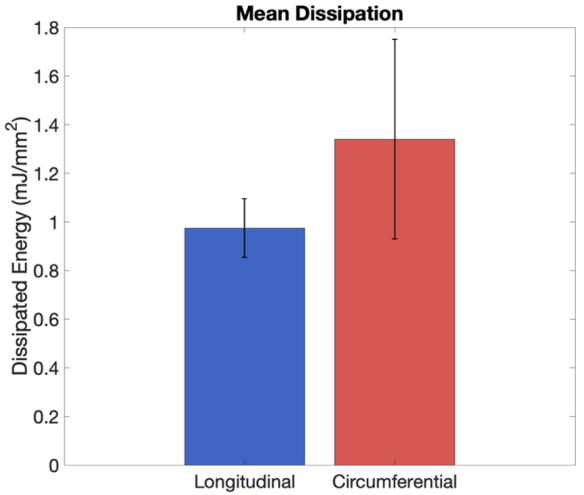

Fig. 27. Bar plot of mean Dissipation.
Longitudinal samples had a mean of 0.98 mJ/mm^2 (SD = 0.12).
Circumferential samples had a mean of 1.3 mJ/mm^2 (SD = 0.41).

Discussion

This study examined the rupture behavior of healthy porcine aorta tissue using a custom-designed SymconCT setup. Fracture was induced in both longitudinal and circumferential samples to investigate rupture behavior along different loading directions. By characterizing the fracture behavior of healthy porcine tissue, the study aimed to test the SymconCT setup before using it on human aneurysm tissue.
The results reveal clear differences between the two orientations, which could originate from the anisotropic mechanical behavior of healthy vascular tissue. Higher values of ultimate stress, ultimate strain, initiation energy, and dissipation were observed in circumferential samples. These findings are consistent with previous experimental studies that examined the rupture behavior of healthy vascular tissue under different loading orientations [14], [22], [23].

The results demonstrate higher ultimate stress values in circumferential samples, indicating a greater load-bearing capacity when the samples were loaded in the circumferential direction. These findings are consistent with the anisotropic mechanical behavior of arterial tissue reported in literature [9]–[12]. Although fiber orientation was not directly assessed in this study, Holzapfel et al. support the suggestion of anisotropic behavior in the tested samples [24]. They investigated the mechanical behavior of individual arterial wall layers. Collagen fibers are differently aligned across these layers, resulting in distinct mechanical responses. Specifically, the media layer was identified as the primary load-bearing component, with collagen fibers predominantly aligned in the circumferential direction, while the intima contributed minimally. This structural organization results in greater stiffness when the vascular tissue is subjected to circumferential loading. Since the present study used samples consisting of both intima and media, it is likely that the media mainly determined the mechanical response. The higher ultimate stress observed in circumferential samples may reflect the need for higher force to rupture across circumferentially aligned collagen fibers. In contrast, longitudinal samples required less stress to initiate rupture, possibly because rupture occurred along the collagen fiber direction.

Ultimate strain and average strain around the crack tip were higher in circumferential samples. Both values were calculated from the DIC-derived strain field based on the image captured just before rupture. These findings suggest that aortic tissue can withstand greater deformation in the circumferential direction compared to the longitudinal direction before rupture. They highlight that the vessel is structurally designed to accommodate circular loading, such as pulsatile blood pressure [12].
A recent study by Alloisio et al. [14], which also employed the symconCT setup with 2D DIC, reported similar findings for ultimate strain in circumferentially loaded samples. However, they found no significant difference in the average strain around the crack tip between orientations. This difference arises due to their different method of strain assessment.
Both studies encountered noisy strain measurements near the crack tip due to out-of-plane displacements. This is a known limitation of 2D DIC, which assumes that the surface remains flat relative to the camera. To correct the inaccuracy, Alloisio et al. applied a post-processing interpolation function to reconstruct a full-field displacement map and track strain throughout the entire test. In contrast, the present study analyzed displacement in a single image just before rupture. This image was manually filtered to remove physiologically unrealistic strain values, ensuring accuracy.
Focusing on the image just before rupture provides a relevant estimate of ultimate strain, as this is typically when tissue experiences its maximum deformation [13]. In contrast, average strain reflects a broader strain distribution around the notch tip rather than a single peak value. As the average strain was calculated from the same image as the ultimate strain, it serves primarily as supportive data. Using continuous strain tracking data throughout the entire fracture test may offer a more comprehensive understanding of average strain evolution.

The reconstructed fracture paths revealed straight crack trajectories in the longitudinal samples, suggesting that rupture propagated along the predominant circumferential collagen fiber alignment. The samples required less energy to initiate fracture, and less energy was dissipated during propagation. This suggests that the rupture encountered little resistance from the tissue's architecture. Moreover, the fracture progressed in multiple stages rather than as a continuous event. Nevertheless, these stages followed one another consistently along a straight path, supporting the interpretation of low structural resistance along the fiber-aligned direction.
The circumferential samples showed curved fracture paths. Their ruptures likely propagated across collagen fibers that were oriented more perpendicular to the fracture direction. The higher initiation energy and greater dissipation observed in these fracture tests suggest an increased resistance from the tissue. The circumferential fractures progressed intermittently, pausing possibly at locations of high resistance. Fracture paths deviated from the straighter trajectories observed in longitudinal samples. They showed changes in direction, likely reflecting interactions with the underlying fiber orientation. The findings suggest that fracture initiation and propagation are strongly influenced by the underlying fiber architecture.
To further explore this relation, future studies could enhance the fracture analysis by incorporating high-resolution imaging techniques to image collagen fiber architecture. Multiphoton microscopy, for example, is a suitable technique for capturing collagen fiber alignment and orientation at the microscale [25]. Knowing the fiber architecture of each sample enables the study of how fracture paths relate to the structural organization. This is especially interesting for future research

on aneurysm tissue, where pathology changes collagen fiber alignment and affects mechanical behavior.

The symconCT setup proved to be an effective modification of the compact tension test for fracturing soft tissue samples. The incorporation of the beam prevented tissue buckling and ensured that fractures propagated from the notch toward the end of the sample, rather than deflecting into the clamps.
While the setup proved functional, material wear between the aluminum clamps and actuator arms affected force measurements in some tests. Friction occurred after several loading and unloading cycles, introducing unphysiological force spikes in the force-displacement curves. All samples that suffered from the artifact were excluded. A solution would be to line the internal surface of the clamps, where they rotate with the actuator arms, with another material. Teflon is a suitable choice due to its low coefficient of friction [26].
Another improvement to the setup would be the integration of a second high-speed camera to enable 3D DIC. Upgrading from a 2D to a 3D DIC system would enable the measurement of out-of-plane deformations, thereby eliminating the tracking inaccuracies of the current setup. Moreover, it would facilitate to track strain data throughout the entire test, adding more value to the average strain measurements.
The strain assessment protocol could be improved by ensuring consistent speckle pattern quality. Strain data reliability was strongly influenced by the applied pattern. For example, the seventh longitudinal sample produced less accurate strain measurements compared to others. The poor-quality speckle pattern required a larger pixel subset size, which reduced strain resolution. To improve measurement quality, speckle patterns should be inspected before testing and reapplied if necessary.
Future studies would also benefit from a larger sample size. In this study, nine samples were tested, including only three longitudinal samples. A larger sample size would enable statistical analysis, such as a t-test, to determine whether the differences in fracture behavior between orientations are statistically significant rather than due to random variation.

F. conclusion

This study demonstrated that the customized SymconCT setup is capable of assessing rupture behavior in soft vascular tissue. By using healthy porcine aorta samples to validate the setup, the study identified clear orientation-dependent differences in rupture behavior. Circumferential samples ruptured with higher ultimate stress, strain, and fracture energy compared to longitudinal samples. These findings suggest that the orientation of collagen fibers in the vascular wall may influence the rupture behavior of vascular tissue.
This study provides a methodological basis for future research into aneurysmal rupture risk, where changes in the aortic wall's structure may influence how the vessel responds to mechanical stress. Enhancing the current setup with 3D DIC and high-resolution imaging techniques would improve strain tracking and enable visualization of collagen fiber orientation, allowing for a more detailed analysis of rupture behavior in aneurysmal tissue.

REFERENCES

[1] V. Kumar, A. K. Abbas, and J. C. Aster, "Chapter 11: Blood Vessels," in Robbins & cotran pathologic basis of disease, 10th ed., V. Kumar, A. Abbas, and J. C. Aster, Eds. Philadelphia, PA: Elsevier - Health Sciences Division, 2020.

[2] P. Kumar and M. L. Clark, "Chapter 30: Cardiology," in Kumar and clark's clinical medicine, A. Feather, Ed. Elsevier, 2017.

[3] J. Golledge, "Abdominal aortic aneurysm: update on pathogenesis and medical treatments," Nat. Rev. Cardiol., vol. 16, no. 4, pp. 225–242, 2019.

[4] S. Sherifova and G. A. Holzapfel, "Biomechanics of aortic wall failure with a focus on dissection and aneurysm: A review," Acta Biomater., vol. 99, pp. 1–17, 2019.

[5] F. Inzoli, F. Boschetti, M. Zappa, T. Longo, and R. Fumero, "Biomechanical factors in abdominal aortic aneurysm rupture," Eur. J. Vasc. Surg., vol. 7, no. 6, pp. 667–674, 1993.

[6] Y.-G. Jeong, Y.-T. Jung, M.-S. Kim, C.-K. Eun, and S.-H. Jang, "Size and location of ruptured intracranial aneurysms," J. Korean Neurosurg. Soc., vol. 45, no. 1, pp. 11–15, 2009.

[7] Y. Orz, S. Kobayashi, M. Osawa, and Y. Tanaka, "Aneurysm size: a prognostic factor for rupture," Br. J. Neurosurg., vol. 11, no. 2, pp. 144–149, 1997.

[8] Y. Gao, "Architecture of the blood vessels," in Biology of Vascular Smooth Muscle, Singapore: Springer Nature Singapore, 2022, pp. 3–17.

[9] G. A. Holzapfel and R. W. Ogden, "Biomechanical relevance of the microstructure in artery walls with a focus on passive and active components," Am. J. Physiol. Heart Circ. Physiol., vol. 315, no. 3, pp. H540–H549, 2018.

[10] D. B. Camasão and D. Mantovani, "The mechanical characterization of blood vessels and their substitutes in the continuous quest for physiological-relevant performances. A critical review," Mater. Today Bio, vol. 10, no. 100106, p. 100106, 2021.

[11] S. S, S. Dahal, S. Bastola, S. Dayal, J. Yau, and A. Ramamurthi, "Stem cell based approaches to modulate the matrix milieu in vascular disorders," Front. Cardiovasc. Med., vol. 9, p. 879977, 2022.

[12] J. Zhou and Y. C. Fung, "The degree of nonlinearity and anisotropy of blood vessel elasticity," Proc. Natl. Acad. Sci. U. S. A., vol. 94, no. 26, pp. 14255–14260, 1997.

[13] C. M. García-Herrera et al., "Mechanical behaviour and rupture of normal and pathological human ascending aortic wall," Med. Biol. Eng. Comput., vol. 50, no. 6, pp. 559–566, 2012.

[14] M. Alloisio, M. Chatziefraimidou, J. Roy, and T. Christian Gasser, "Fracture of porcine aorta-Part 1: symconCT fracture testing and DIC," Acta Biomater., vol. 167, pp. 147–157, 2023.

[15] A. Ortega, P. Maimí, E. V. González, and L. Ripoll, "Compact tension specimen for orthotropic materials," Compos. Part A Appl. Sci. Manuf., vol. 63, pp. 85–93, 2014.

[16] F. H. Wittmann, K. Rokugo, E. Brühwiler, H. Mihashi, and P. Simonin, "Fracture energy and strain softening of concrete as determined by means of compact tension specimens," Materials and Structures, vol. 21, no. 1, pp. 21–32, 1988.

[17] N. I. Cupitra, J. León-Rodríguez, J. C. Calderón, and R. Narvaez-Sanchez, "The pig is a better model than the rabbit or rat for studying the pathophysiology of human mesenteric arteries," Microvasc. Res., vol. 147, no. 104494, p. 104494, 2023.

[18] P. L. Reu et al., "DIC challenge: Developing images and guidelines for evaluating accuracy and resolution of 2D analyses," Exp. Mech., 2017.

[19] F. Tariq, M. Siddiqui, Zeeshan, Nausheen, M. Ahmed, and W. Hussain, "Practical Application of DIC in Fatigue and Fracture Toughness Testing," in Proceedings of the International Astronautical Congress, 2012.

[20] K. Bircher, M. Zündel, M. Pensalfini, A. E. Ehret, and E. Mazza, "Tear resistance of soft collagenous tissues," Nat. Commun., vol. 10, no. 1, p. 792, 2019.

[21] B. Merei, P. Badel, L. Davis, M. A. Sutton, S. Avril, and S. M. Lessner, "Atherosclerotic plaque delamination: Experiments and 2D finite element model to simulate plaque peeling in two strains of transgenic mice," J. Mech. Behav. Biomed. Mater., vol. 67, pp. 19–30, 2017.

[22] H. Chen et al., “A study on the ultimate mechanical properties of middle-aged and elderly human aorta based on uniaxial tensile test,” Front. Bioeng. Biotechnol., vol. 12, p. 1357056, 2024.
[23] R. N. Vaishnav, J. T. Young, J. S. Janicki, and D. J. Patel, “Nonlinear anisotropic elastic properties of the canine aorta,” Biophys. J., vol. 12, no. 8, pp. 1008–1027, 1972.
[24] G. A. Holzapfel, G. Sommer, C. T. Gasser, and P. Regitnig, “Determination of layer-specific mechanical properties of human coronary arteries with nonatherosclerotic intimal thickening and related constitutive modeling,” Am. J. Physiol. Heart Circ. Physiol., vol. 289, no. 5, pp. H2048-58, 2005.
[25] R. Cicchi et al., “Scoring of collagen organization in healthy and diseased human dermis by multiphoton microscopy,” J. Biophotonics, vol. 3, no. 1–2, pp. 34–43, 2010.
[26] V. Saisnith and V. Fridrici, “A study of the wear damage of a PTFE coating: The effects of temperature and environment on its mechanical and tribological properties,” Wear, vol. 480–481, no. 203946, p. 203946, 2021.
[27] P. Frankovský, I. Virgala, P. Hudák, and J. Kostka, “The use the of digital image correlation in a strain analysis,” Int. J. Appl. Mech. Eng., vol. 18, no. 4, pp. 1283–1292, 2013.
[28] P. L. Reu et al., “DIC challenge: Developing images and guidelines for evaluating accuracy and resolution of 2D analyses,” Exp. Mech., 2017.
[29] LaVision GmbH, “DIC software,” LaVision GmbH. [Online]. Available: https://www.lavision.de/en/applications/materials-testing/system-components/dic-software/. [Accessed: 01-Jun-2025].
[30] F. Tariq, M. Siddiqui, Zeeshan, Nausheen, M. Ahmed, and W. Hussain, “Practical Application of DIC in Fatigue and Fracture Toughness Testing,” in Proceedings of the International Astronautical Congress, 2012.

Appendix

A. Symmetry-constrained compact tension test setup

The symmetry-constraint compact tension (SymconCT) test setup was developed by Alloisio et al. as an improved version of the conventional compact tension test. It is specifically designed to assess rupture behavior in soft biological materials [14]. The conventional compact tension test is a standard method in materials science for assessing fracture behavior by applying a tensile load to a notched sample [14]-[16]. The load is applied near the notch to concentrate stress at the crack tip and initiate propagation toward the opposite end of the sample. However, this method is unable to produce stable crack propagation in soft tissue, such as blood vessels. Due to their low bending stiffness, soft tissue tends to deform out of plane during tensile loading. Specifically, the region opposite the notch is prone to buckling, which prevents stress from being concentrated at the notch tip. As a result, it is not possible to perform stable and repeatable fracture tests.

The SymconCT setup addresses this issue by incorporating an elastic beam on the side opposite the notch. This beam causes a slight outward shift in the clamps, spanning the back of the sample. During loading, it counteracts clamp rotation and stabilizes the tissue opposite to the notch. This constraint reduces out-of-plane deformation and allows for controlled crack propagation from the notch through the tissue.

In addition to preventing buckling, the beam also compensates for the anisotropic mechanical properties of vascular tissue, which can affect fracture path trajectory. In the aortic media, collagen fibers are predominantly aligned in the circumferential direction. When rupture is initiated along this fiber orientation, fractures tend to follow a relatively straight path. In contrast, when rupture has to propagate across the fibers, it may cause the crack to shift along the relatively perpendicular fiber direction and deviate toward one of the clamps. The bending moment introduced by the beam ensures a symmetrical opening of the clamps, stabilizing the tissue on both sides. Increasing the stiffness of the beam further enhances this symmetry, making it more likely that the fracture remains centered throughout the test. A higher beam stiffness increases the degree of symmetry, making it more likely that the fracture remains centered.

Figure 1 shows the SymconCT setup, which was specifically designed for this study. The setup includes aluminum arms mounted on a biaxial testing machine, configured for uniaxial tensile loading. The arms apply tensile force to aluminum clamps that hold the aortic sample in place. The inner surfaces of the clamps are lined with sandpaper to prevent sample slippage during testing. Each sample contains a notch and is positioned in the clamps with the notch aligned on the side of the arms. This positioning ensures that the tensile force is concentrated at the notch throughout the fracture test. The elastic beam, made of spring steel wire, is inserted into the clamps on the side opposite the notch. The beam has a bending stiffness between 1800 and 2000 N/mm².

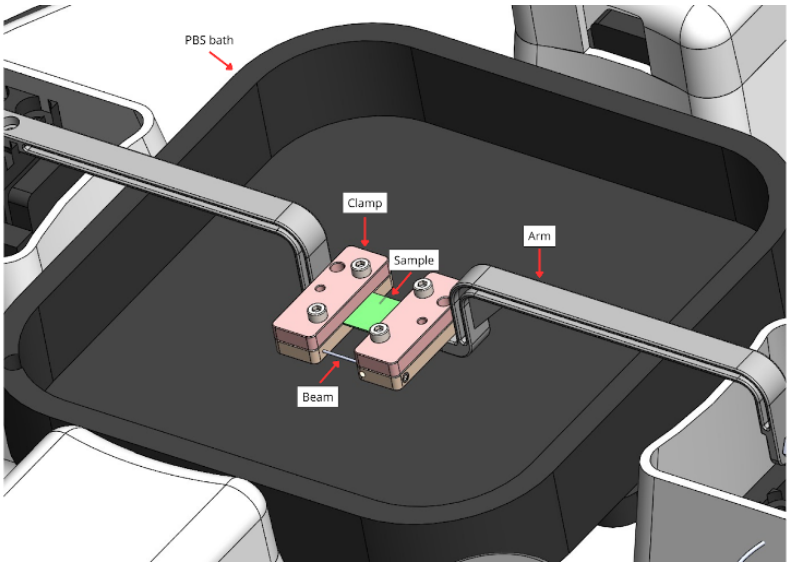

Figure 1: Side view of the custom-designed SymconCT setup. The setup includes arms, connected to the biaxial testing machine, for applying tensile load. The clamps secure the tissue sample, with the beam positioned opposite to the notch.

B. Digital Image Correlation

Digital Image Correlation (DIC) is an optical technique that is used to measure surface deformation during the mechanical testing of materials. The method tracks the movement of a contrasting pattern applied to the surface of the material that is deformed [27]-[30]. In this study, the contrasting pattern was a randomized orange fluorescent speckle pattern that was applied to the intima layer of the aortic samples.

A high-speed camera is used to capture surface displacement during mechanical testing. DIC can be performed in two-dimensional (2D) or three-dimensional (3D) configurations. The 2D setup captures in-plane deformation using a single camera. In contrast, the 3D setup uses at least two cameras positioned at an angle to also capture out-of-plane motion [27], [29].

The present study used a 2D DIC configuration, using a single high-speed camera. The camera was paired with a blue LED light source to enhance image contrast. Blue lighting reduced background glow from the tissue and reflections from the surrounding phosphate-buffered saline bath, enabling better tracking of the contrast between the speckles and tissue.

The camera records a sequence of images throughout the deformation process. They are then analyzed using DIC software that divides the surface of the material into small sub-regions. The first image that was taken before deformation is the reference frame. The software tracks the motion of the contrasting pattern in each sub-region, by comparing subsequent images to the reference [27], [30].

For this study, post-processing was performed in DaVis (LaVision, Germany), which provided the magnitude and orientation of the maximum and minimum principal strains at each sub-region in the sample [29].

C. Excluded results

Of the 16 tested samples, 7 were excluded from the study due to incomplete rupture or setup-related artifacts. In cases of incomplete rupture, the fracture behavior could not be fully characterized, making these measurements unsuitable for comparison with samples that did rupture.
The second reason for exclusion involved a mechanical artifact in the experimental setup. Both the clamps and the actuator arms in the custom symconCT setup were made of aluminum. After repeated testing, friction occurred between these aluminum components, leading to surface wear. This caused the clamps to rotate less smoothly within the actuator arms. Consequently, the following tests displaced in a stick–slip motion, visible as sharp force spikes in the force–displacement curves. These fluctuations interfered with the real rupture response. To restore smooth operation, the clamp–arm interfaces were polished whenever surface friction became apparent.
Figures 2–9 show the force–displacement curves of the excluded samples.

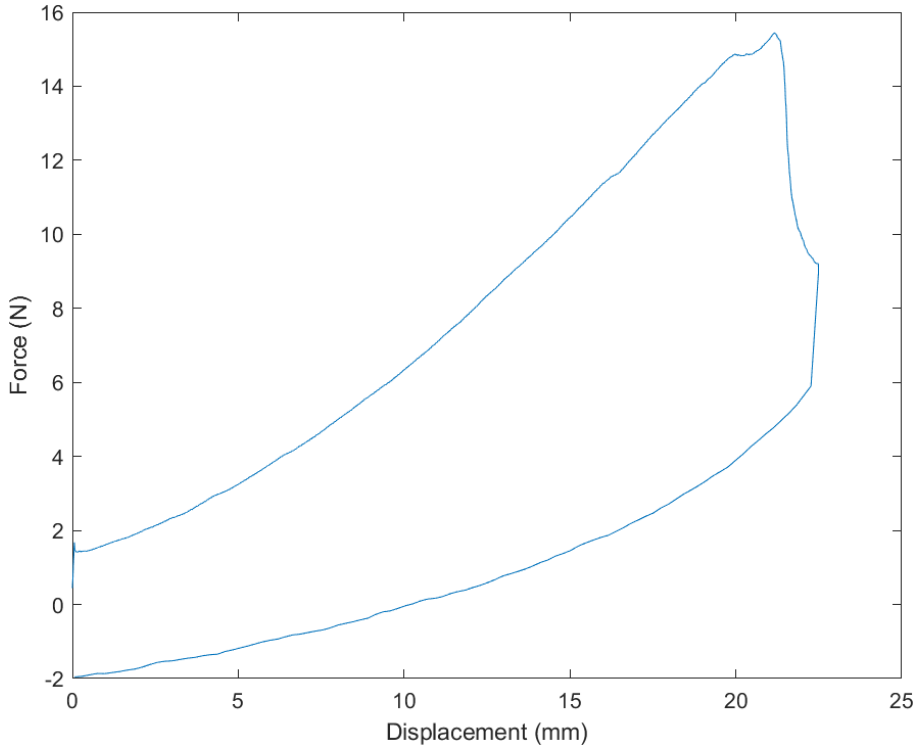

Figure 2: Raw force–displacement curve of L1, tested on 29 January. The test was excluded due to incomplete rupture. Force increases during the loading phase. There is no distinct rupture or post-rupture beam behavior.

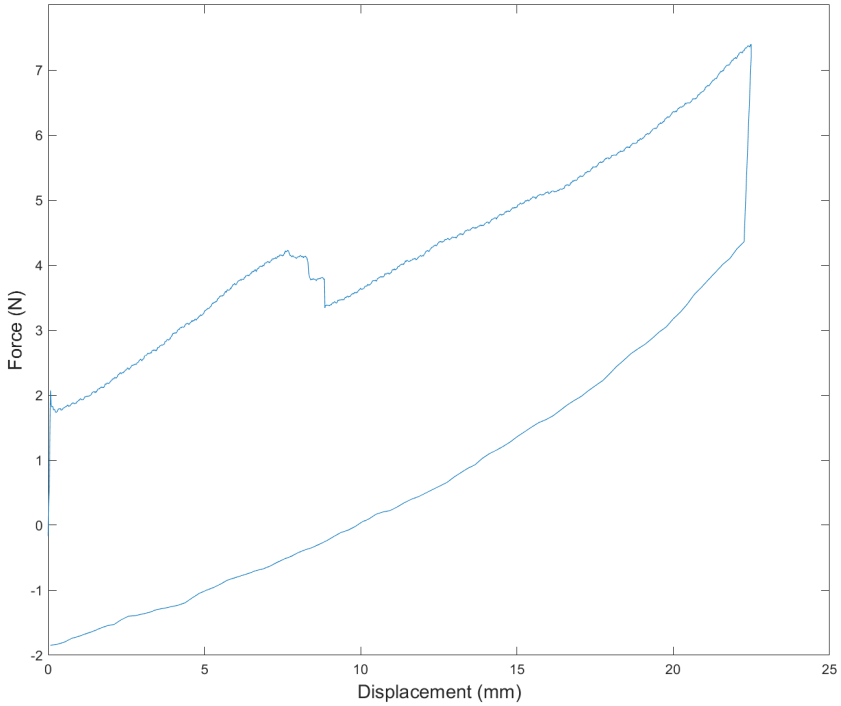

Figure 3: Raw force–displacement curve of the L4, tested on 29 January. The test was excluded due to setup-related artifacts. The curve shows irregular force spikes caused by the stick-slip motion of the clamps within the actuator arms.

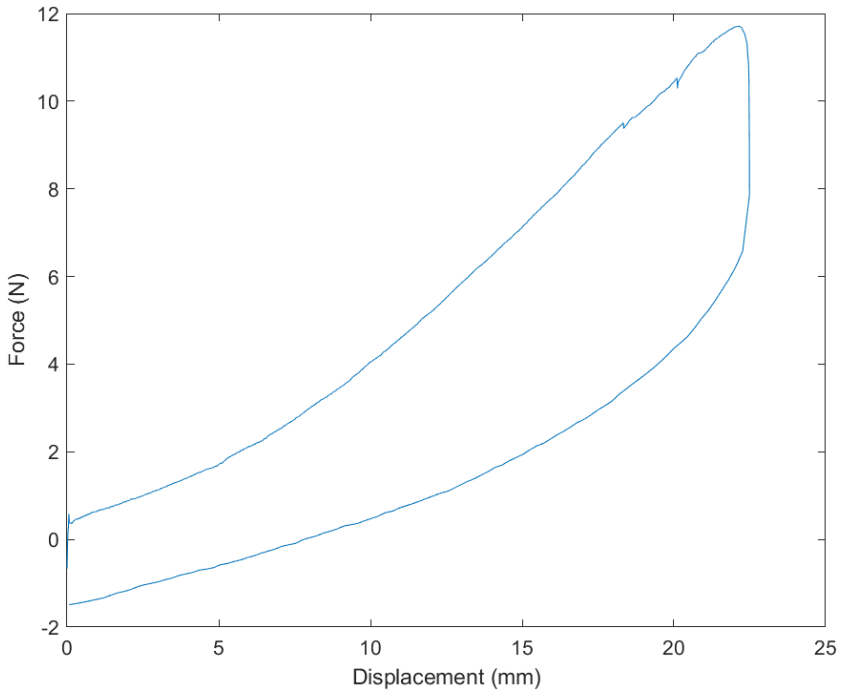

Figure 4: Raw force–displacement curve of sample L1, tested on 30 January. The test was excluded due to incomplete rupture. Force increases during the loading phase. There is no distinct rupture or post-rupture beam behavior.

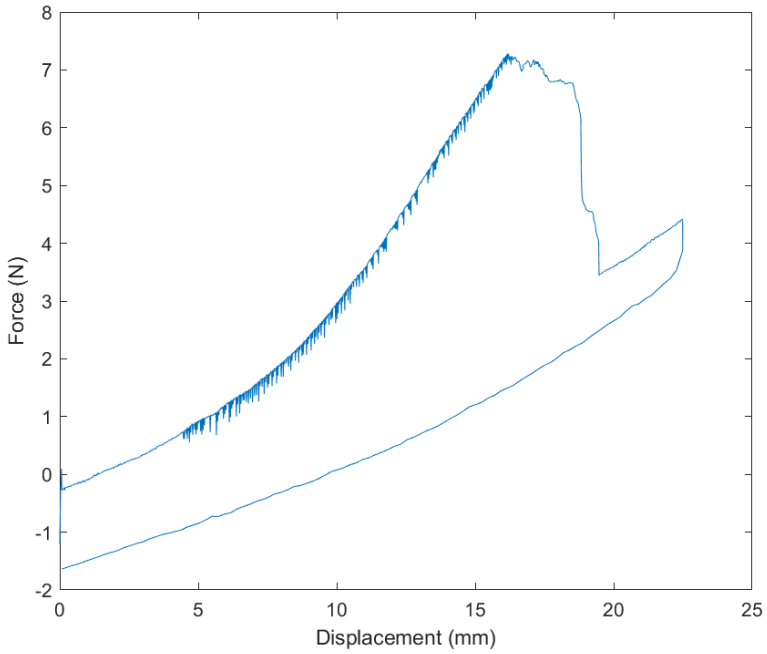

Figure 5: Force–displacement curve of the L3, tested on 30 January. The test was excluded due to setup-related artifacts. The curve shows irregular force spikes caused by the stick-slip motion of the clamps within the actuator arms.

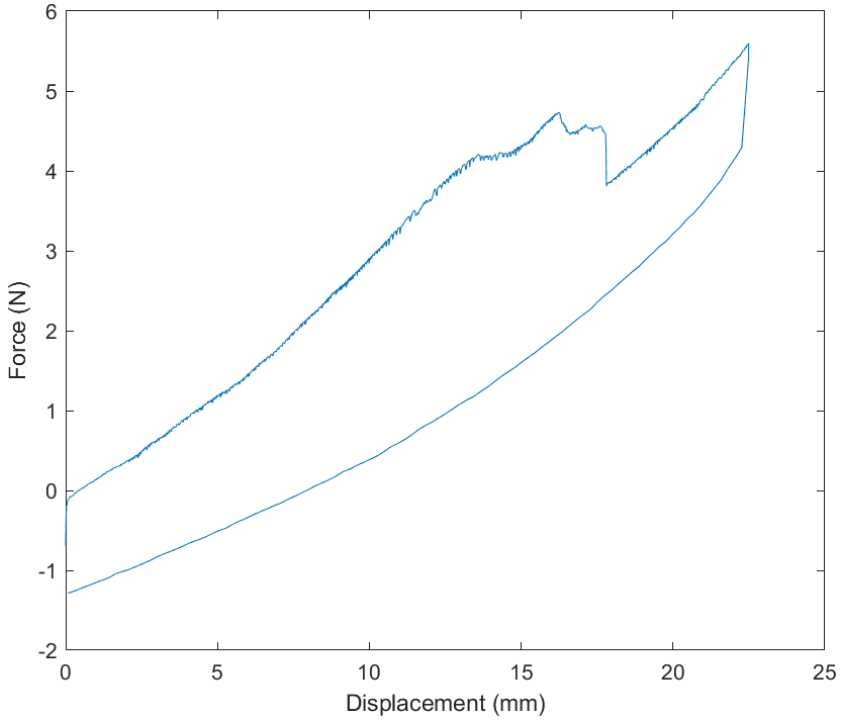

Figure 6: Force–displacement curve of the L4, tested on 30 January. The test was excluded due to setup-related artifacts. The curve shows irregular force spikes caused by the stick-slip motion of the clamps within the actuator arms.

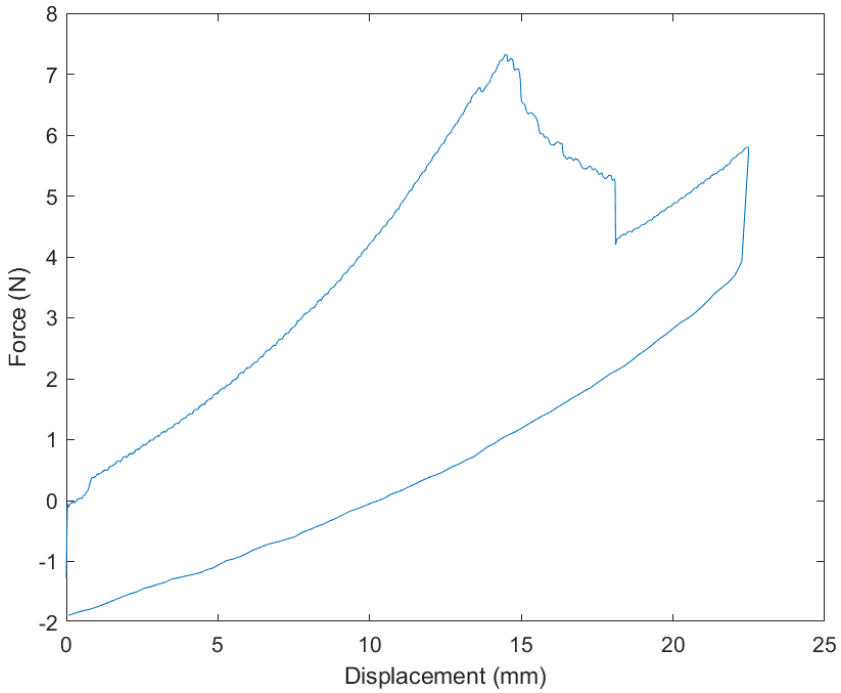

Figure 7: Force–displacement curve of sample C1, tested on 30 January. The test was excluded due to setup-related artifacts. The curve shows irregular force spikes caused by the stick-slip motion of the clamps within the actuator arms.

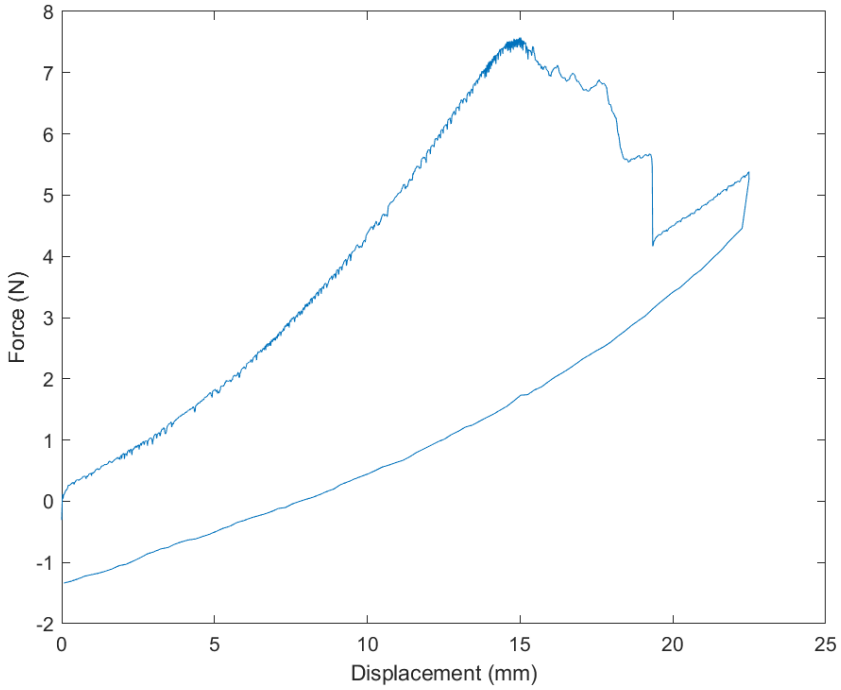

Figure 8: Force–displacement curve of sample C2, tested on 30 January. The test was excluded due to setup-related artifacts. The curve shows irregular force spikes caused by the stick-slip motion of the clamps within the actuator arms.

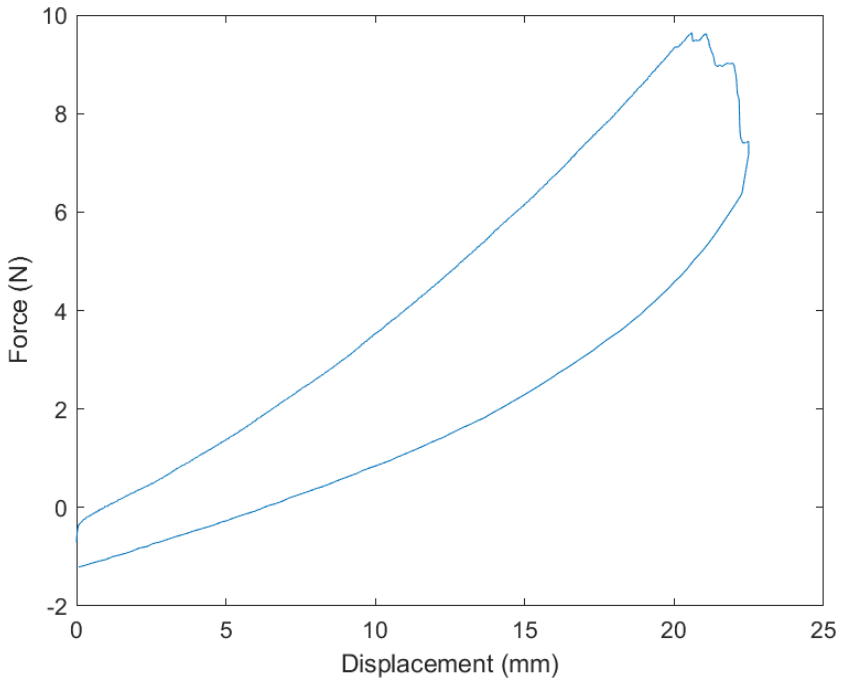

Figure 9: Raw force–displacement curve of sample C4, tested on 30 January. The test was excluded due to incomplete rupture. Force increases during the loading phase. There is no distinct rupture or post-rupture beam behavior.

D. All results

From the 16 aortic samples tested, the mechanical behavior of 9 samples was analyzed. The results of the second circumferential sample (C2) were used as the representative example and are presented in the main paper. This appendix contains the results of all remaining samples. Each subsection includes the analyses for ultimate stress, strain, reconstructed fracture path, and fracture energy. Longitudinal samples are denoted by L and circumferential samples by C. The accompanying number refers to the order in which the measurements were performed.

Samples L2 and C4 lacked reliable DIC data due to the separation of the intima and media layers during testing. This limitation prevented accurate tracking of strain and crack progression. Nevertheless, force-displacement data were recorded, allowing for the assessment of ultimate stress and initiation energy. DIC images of the failed samples are included in the subsections to reveal the layer separation.

Second longitudinal sample tested on 29 January

Sample L2 exhibited a relatively straight rupture path . The ultimate engineering stress was 181.5 kPa. Following this peak, the tissue tore in three stages, visible as three distinct drops in the force-displacement curves, ending in a complete rupture. The reconstructed crack path measured 12.13 mm in length. The sample reached a maximum principal strain of 141% before rupture, with an average strain of 24.7% in the circular area surrounding the crack tip. The normalized initiation energy was 7.83 mJ/mm, and the propagation energy was 0.89 mJ/mm^2.

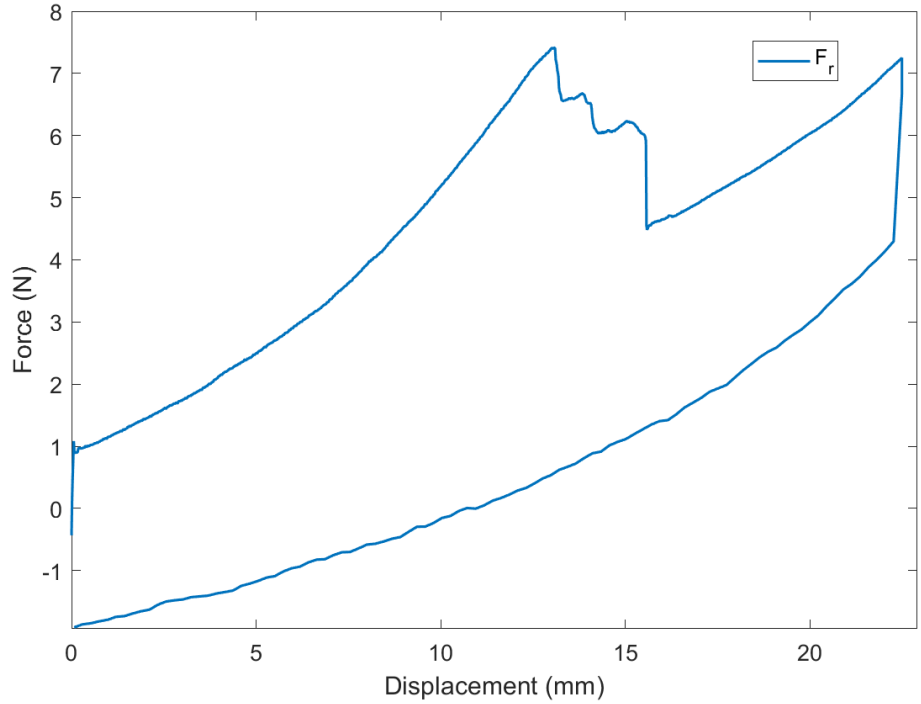

Figure 10: Raw force-displacement curve of L2, showing loading and unloading phases during fracture testing. The steep slope at the start of unloading indicates a friction-related artifact resulting from surface wear at the aluminum clamp–arm interface.

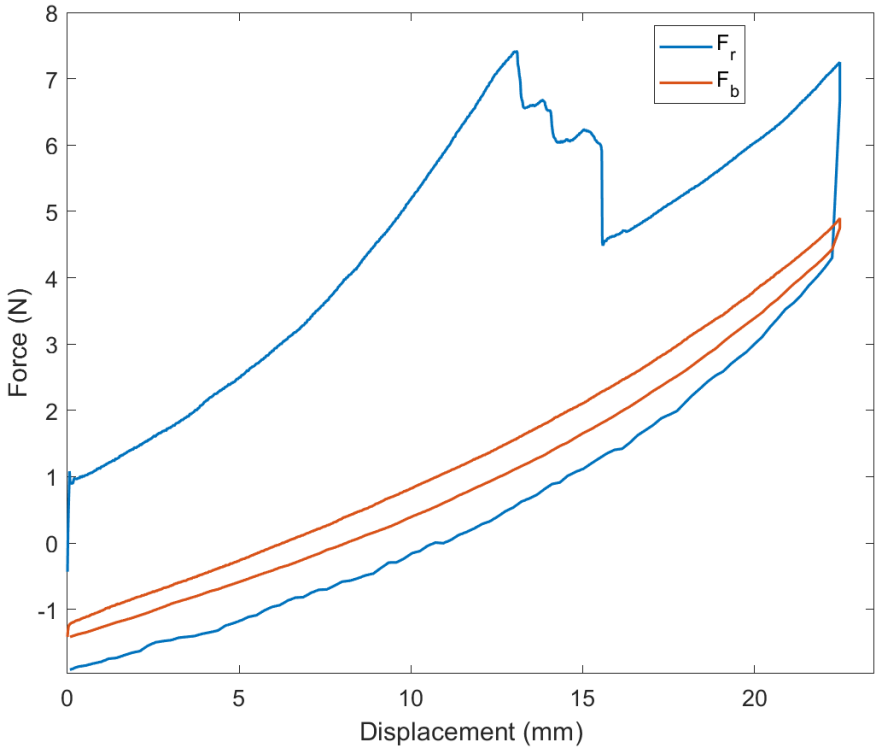

Figure 11: Raw force-displacement curve of L2 plotted alongside beam cycle 8 before offset correction.

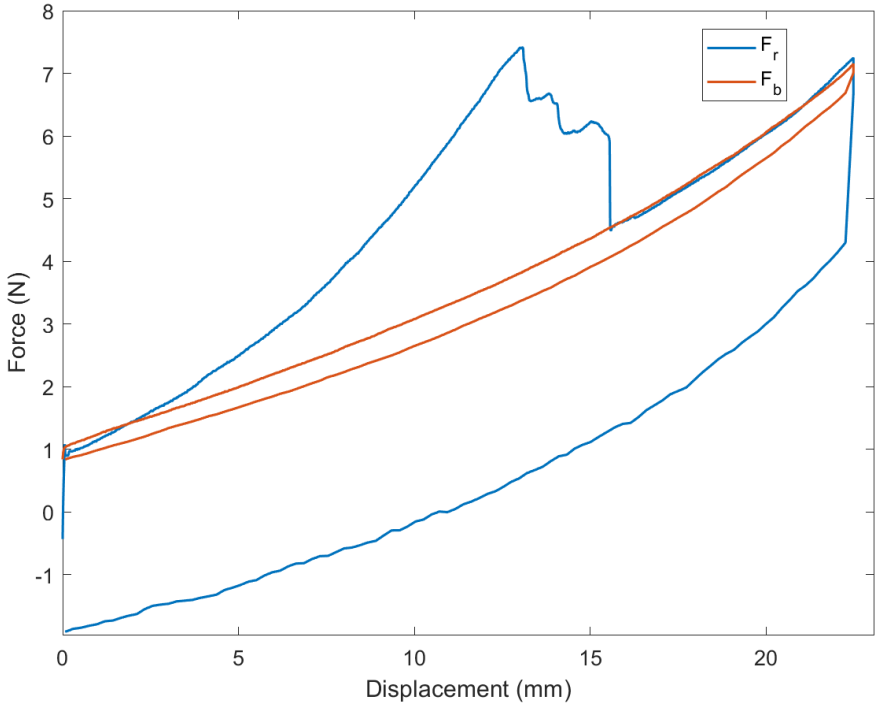

Figure 12: Raw force-displacement curve of L2 and beam cycle 8 after vertical alignment at the rupture point.

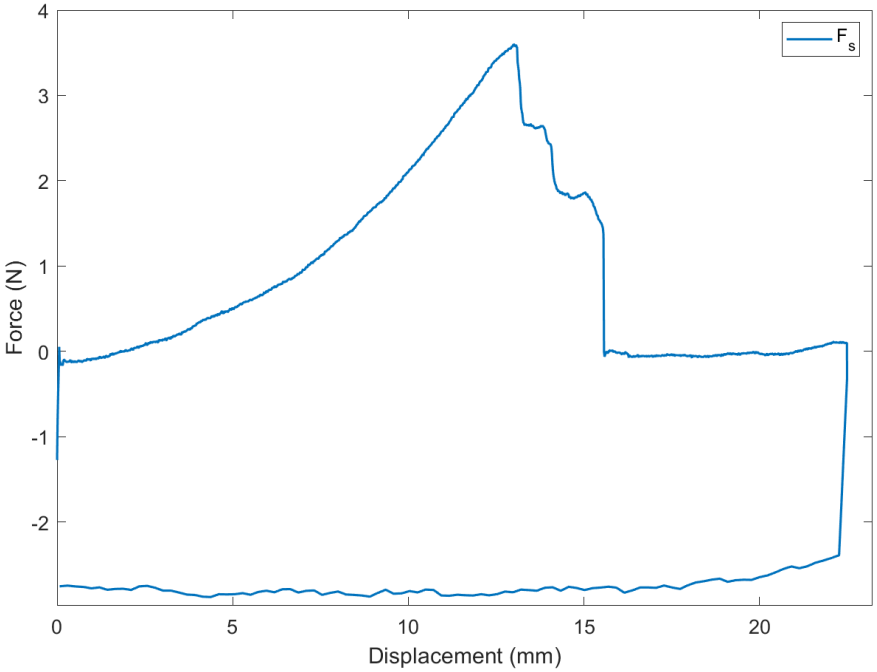

Figure 13: 5. Corrected force-displacement curve of L2 after subtraction of the beam contribution.

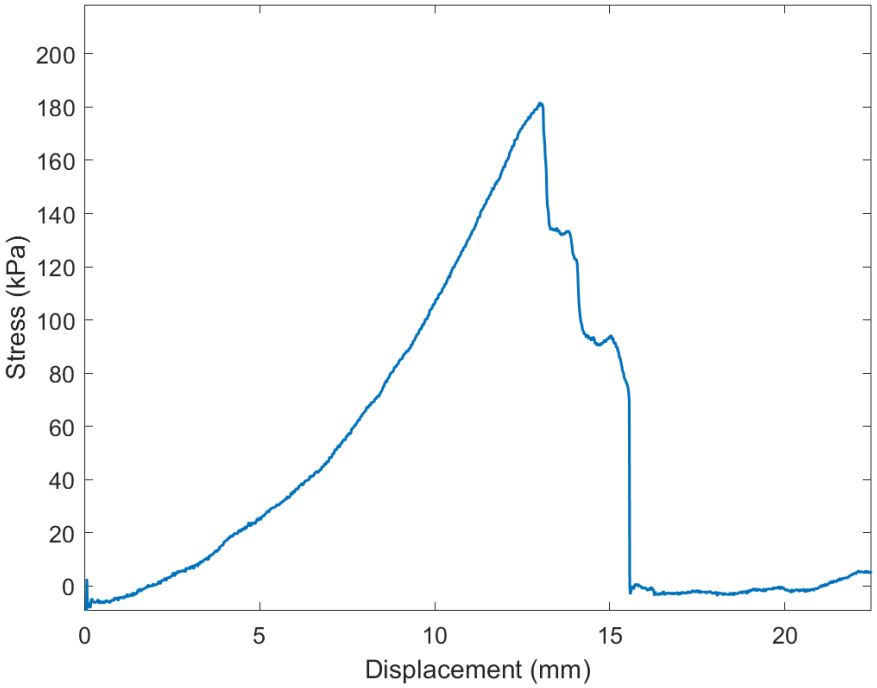

Figure 14: Engineering stress–displacement curve of L2. The peak corresponds to an ultimate engineering stress of 181.5 kPa. The curve shows the loading phase only.

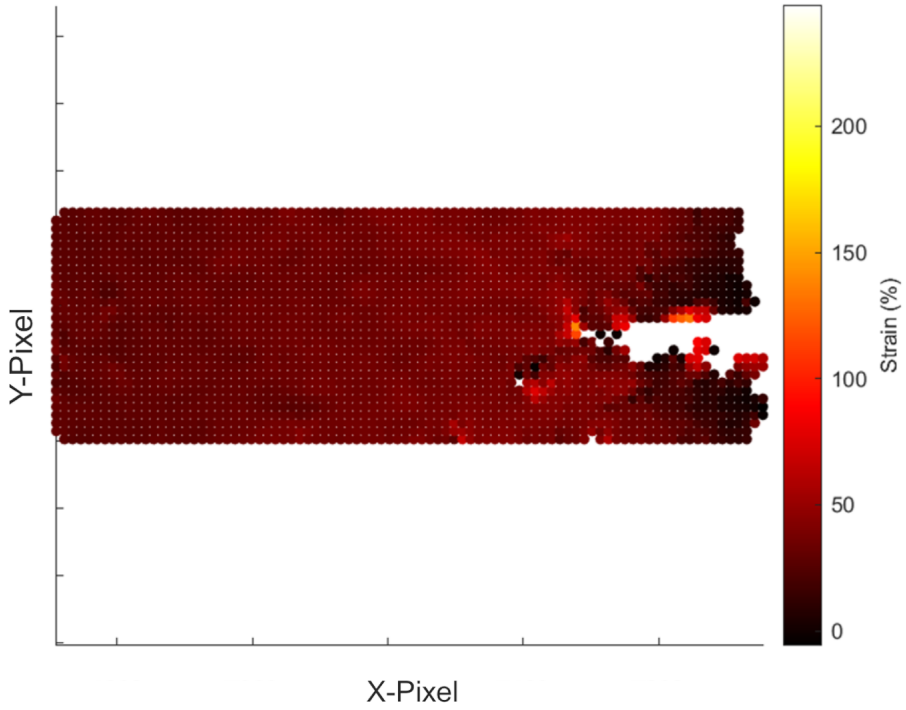

Figure 15: Heatmap of maximal principal strain across the sample surface, generated from the DIC image immediately before crack initiation. Yellow regions indicate high local strain, while red indicates lower strain levels. The ultimate strain was 141%.

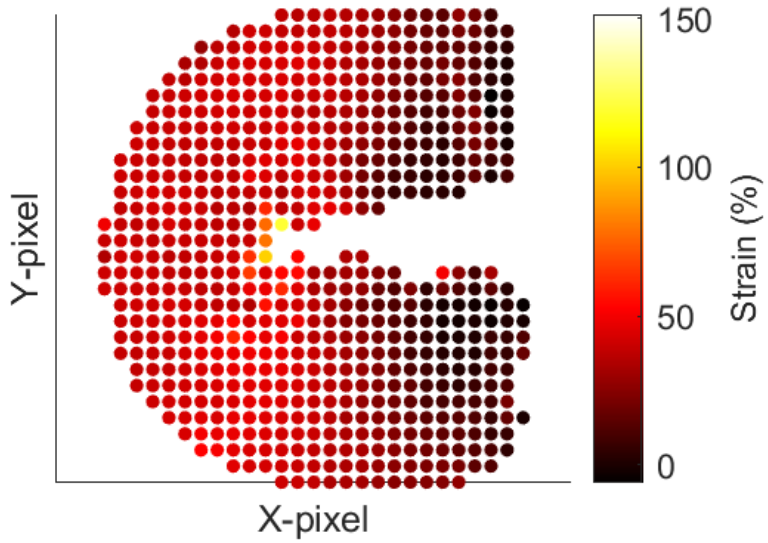

Figure 16: Zoomed-in strain heatmap of a circular region surrounding the crack tip. The average maximal principal strain within this region was 24.7%.

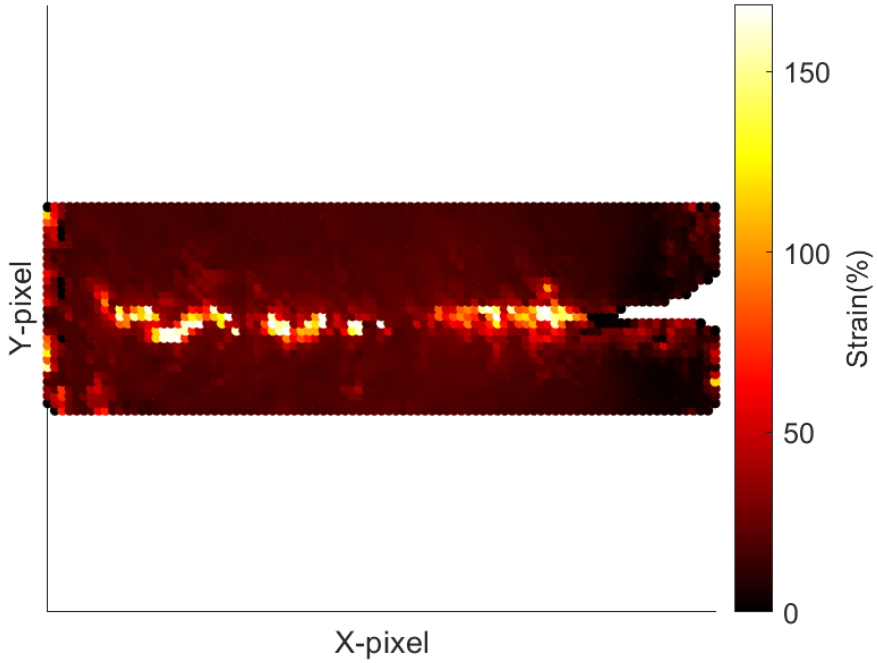

Figure 17: Cumulative heatmap of maximal principal strain recorded per pixel over the entire fracture test. The high-strain pattern visualizes the crack trajectory across the sample surface. Yellow regions represent highly strained areas, whereas red indicates lower strain values.

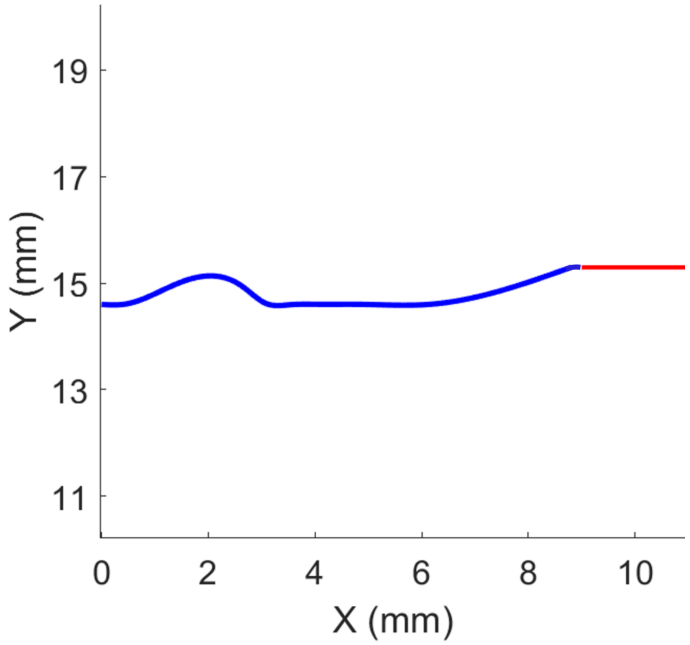

Figure 18: Reconstructed fracture path based on interpolated regions of highest strain. The 2 mm initial notch is shown in red. Pixel coordinates were converted to millimeters using the known sample width for calibration. The total crack path length was estimated to be 12.13 mm.

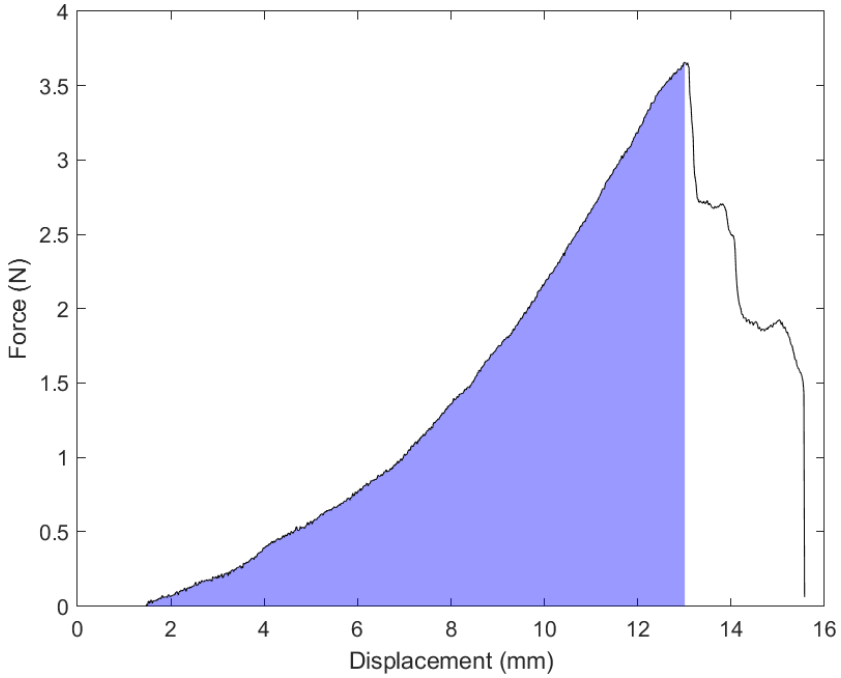

Figure 19: Calculation of the initiation energy. The blue area under the corrected force-displacement curve represents the mechanical work required to initiate rupture. The curve is integrated from the start of the test up to the point of visible crack formation. After normalization, the total initiation energy was 7.83 mJ/mm

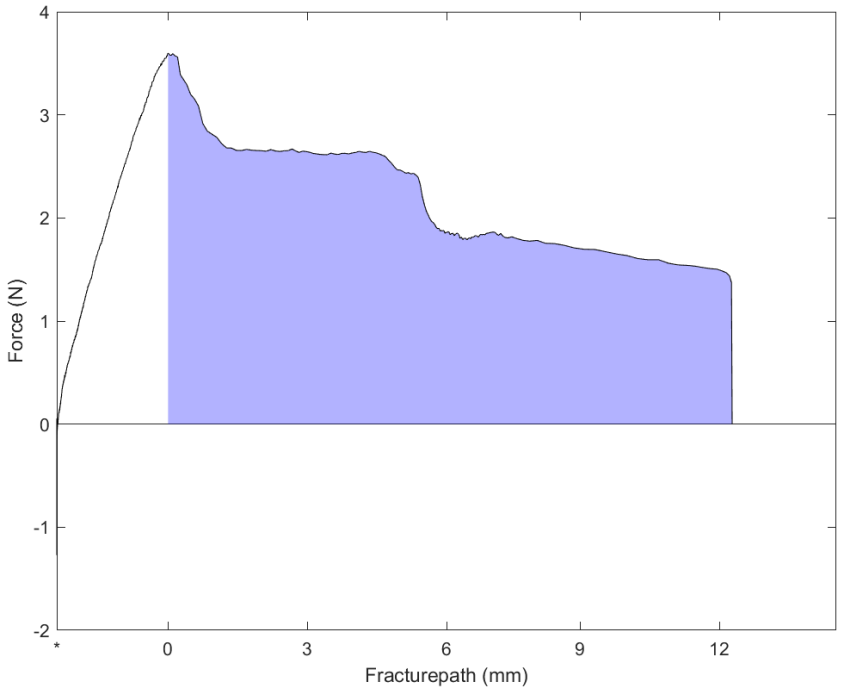

Figure 20: Calculation of the propagation energy. The blue area under the force–fracture path curve represents the mechanical work required to propagate the crack through the sample. After normalization, the dissipation was 0.89 mJ/mm^2.

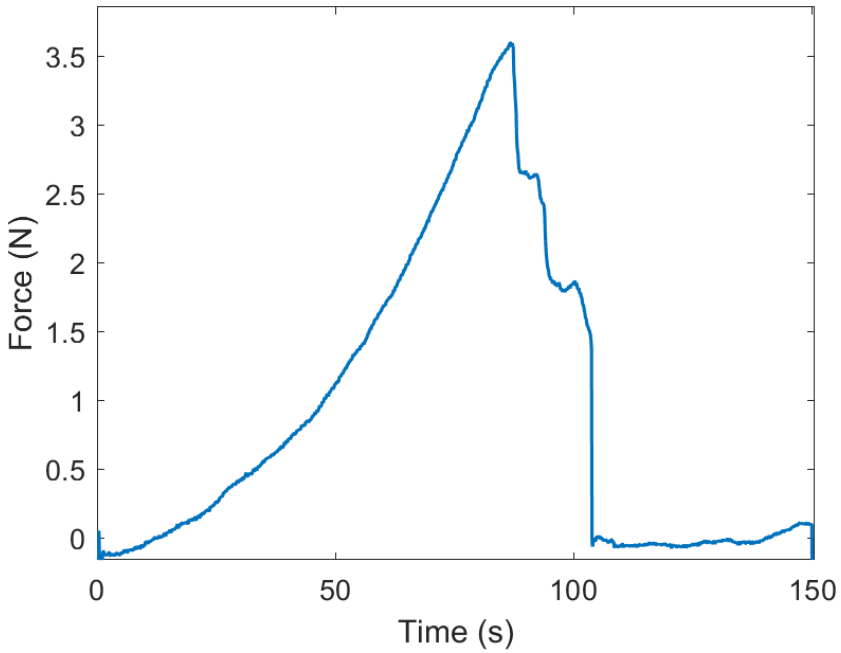

Figure 21: Raw force-time curve recorded by the biaxial testing machine during fracture testing. This dataset provided the force measurements used to construct the force-fracture path curve.

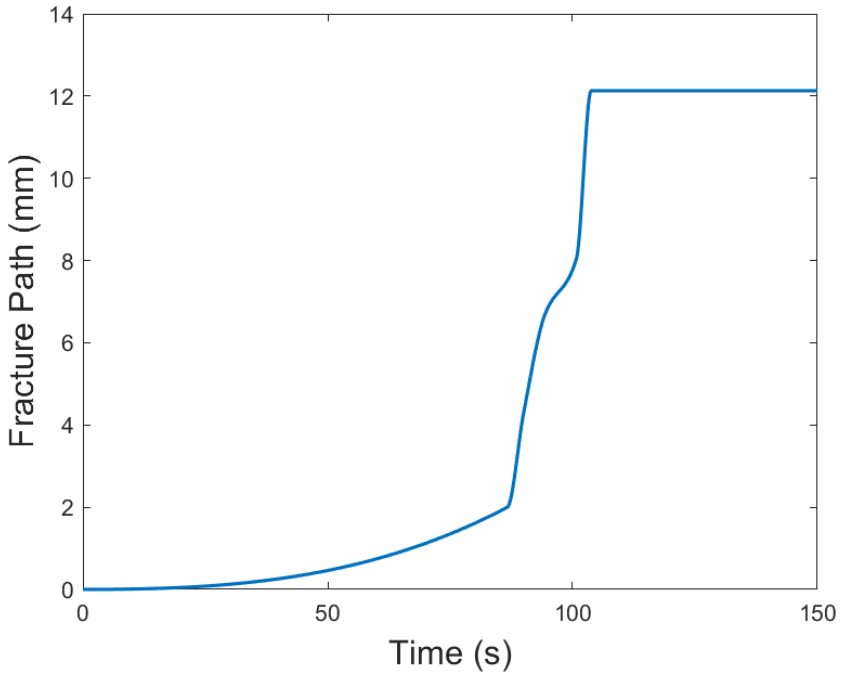

Figure 22: Fracture path–time curve reconstructed by manually analyzing DIC images. Fracture lengths were estimated by identifying the crack location at specific time points, enabling synchronization with the force-time data.

Third longitudinal sample tested on 29 January

Sample L3 presented challenges for DIC analysis due to delamination between the intima and media layers. As shown in Figure 21, the speckle pattern was applied to the intima, which exhibited a shifting crack trajectory toward the right clamp. In contrast, the underlying media layer ruptured in a straight line. This media tear is reflected in the force-displacement curve, which shows continuous rupture with two rapid fracture phases.
The separation of tissue layers resulted in unreliable strain field data, which prevented the calculation of ultimate strain, average strain, and reconstruction of the crack path. Despite these limitations, the ultimate engineering stress was calculated to be 156.5 kPa. Additionally, the initiation energy was 9.62 mJ/mm. The propagation energy could not be assessed due to the missing fracture path estimation.

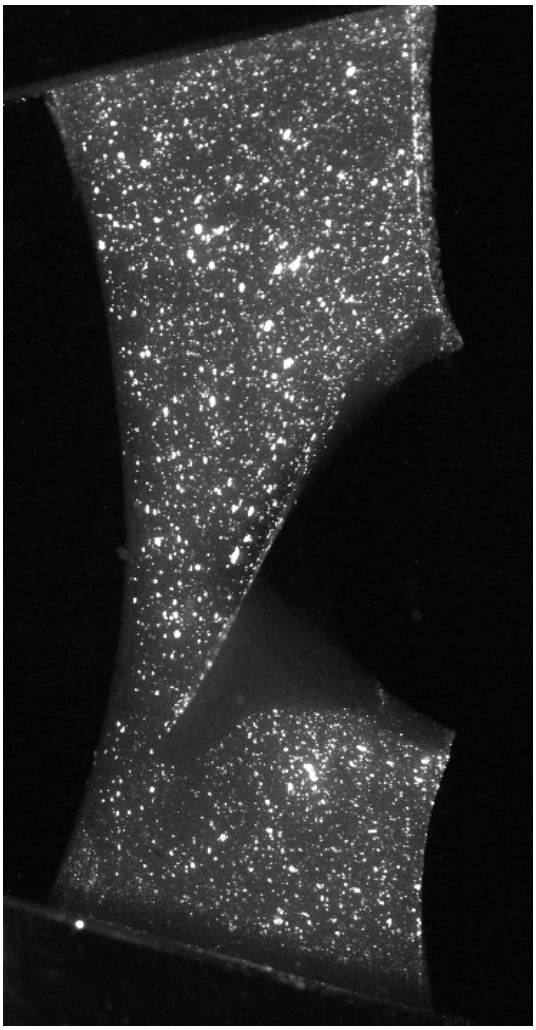

Figure 23: DIC image of L3 during rupture. The intima and media layers tore separately. The speckled intima turned right during tearing, while the media, shown underneath the intima in light grey, followed a straight crack path.

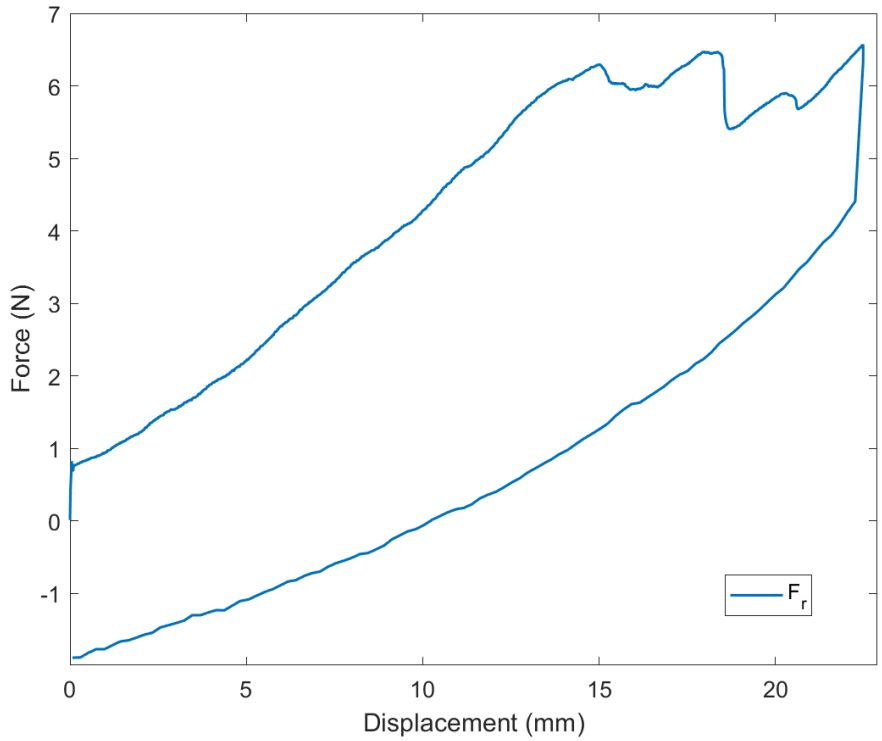

Figure 24: The raw force-displacement curve of L3, showing loading and unloading phases during fracture testing. The steep slope at the start of unloading indicates a friction-related artifact resulting from surface wear at the aluminum clamp–arm interface.

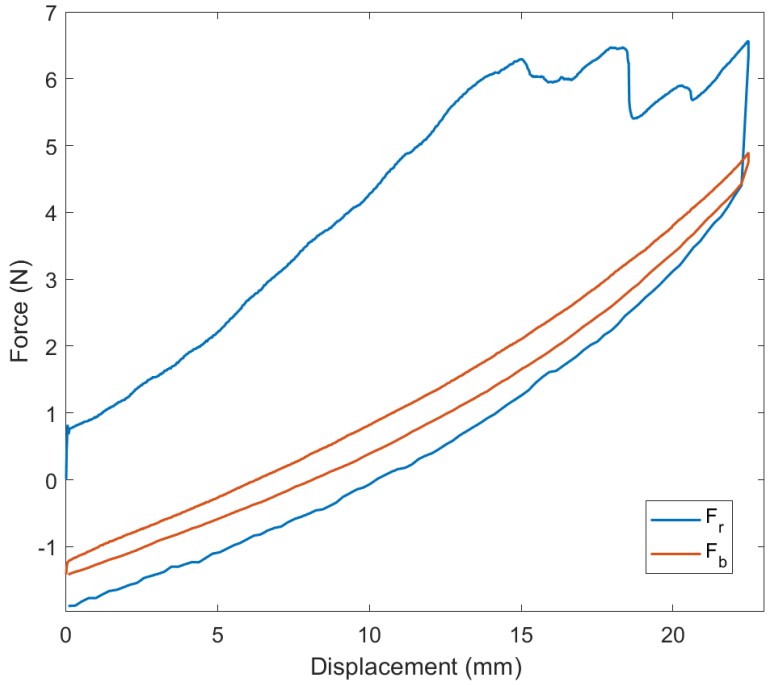

Figure 25: Raw force-displacement curve of L3 plotted alongside beam cycle 8 before offset correction.

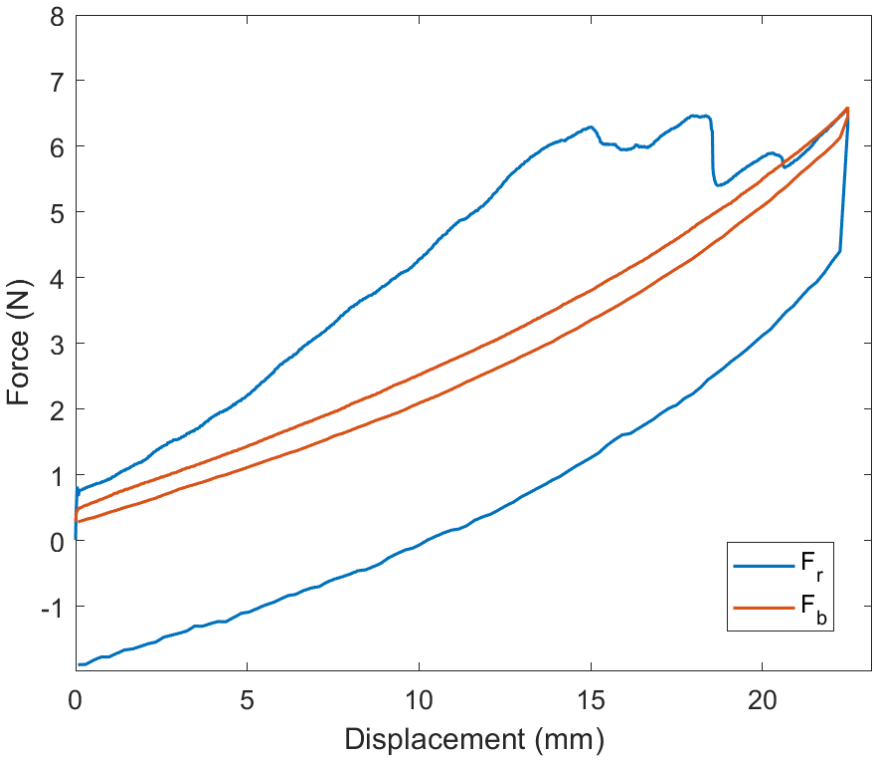

Figure 26: Raw force-displacement curve of L3 and beam cycle 8 after vertical alignment at the rupture point.

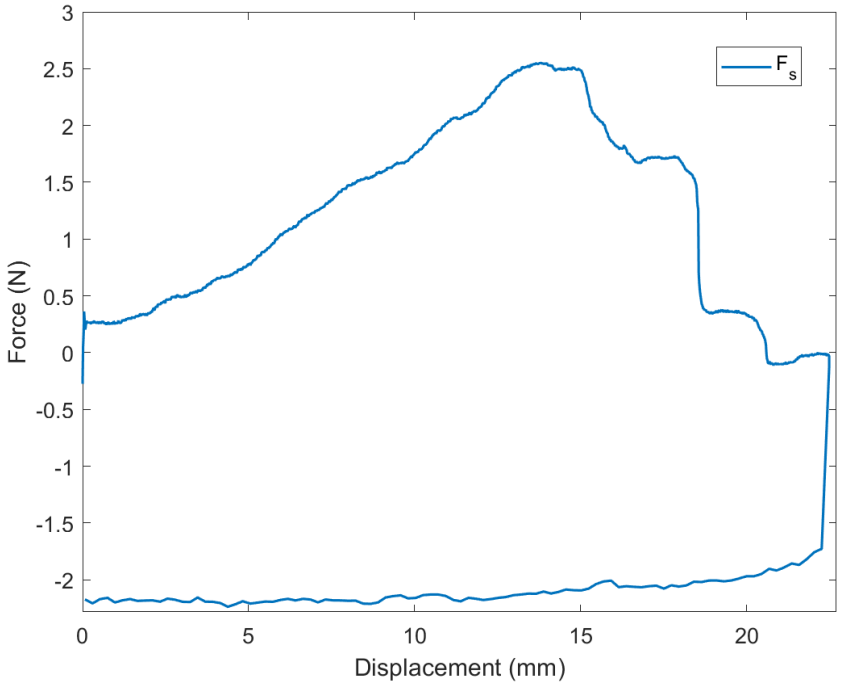

Figure 27: Corrected force-displacement curve of L3 after subtraction of the beam contribution.

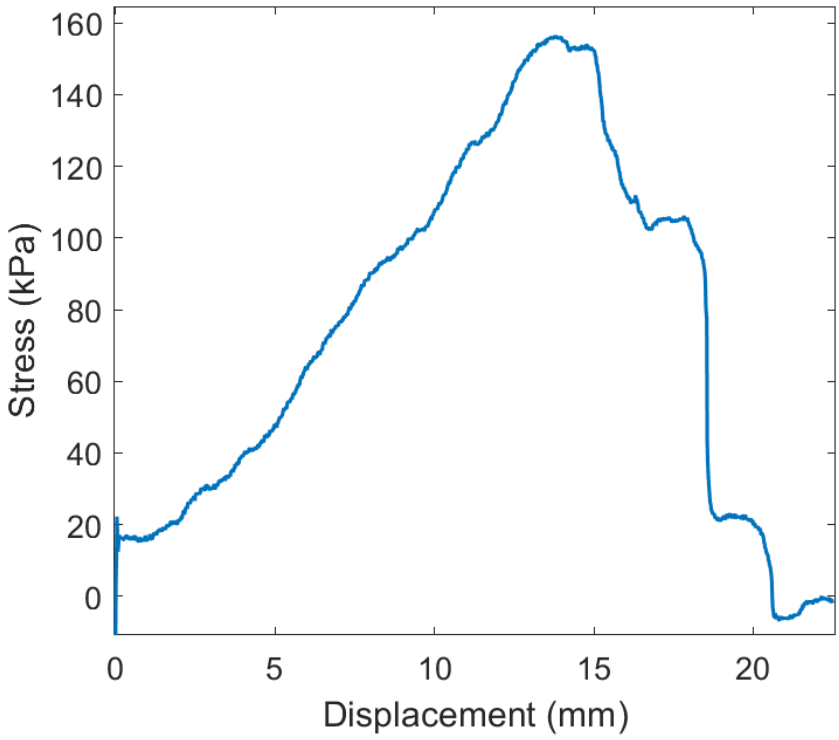

Figure 28: Engineering stress–displacement curve of L3. The peak corresponds to an ultimate engineering stress of 156.5 kPa. The curve shows the loading phase only.

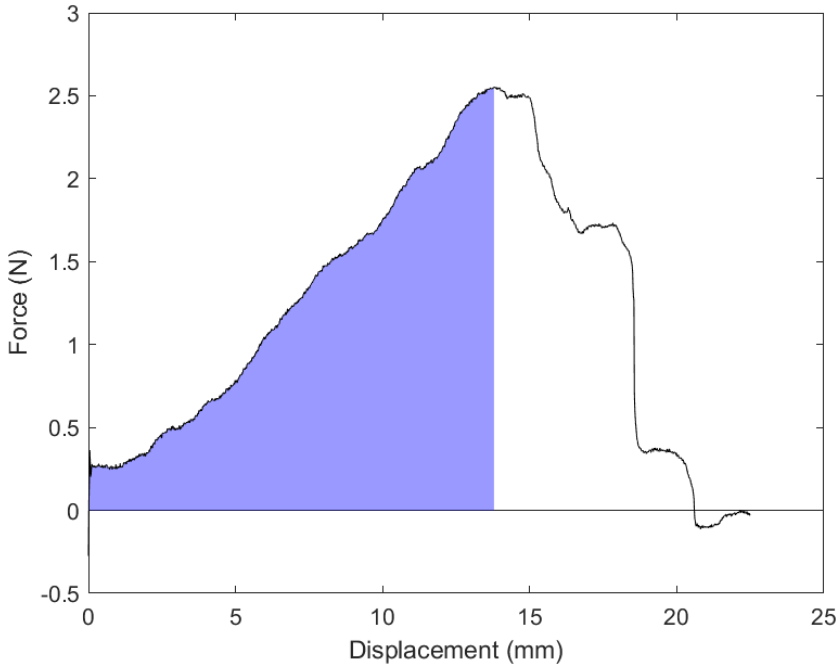

Figure 29: Calculation of the initiation energy. The blue area under the corrected force-displacement curve represents the mechanical work required to initiate rupture. The curve is integrated from the start of the test up to the point of visible crack formation. After normalization, the total initiation energy was 9.62 mJ/mm.

First circumferential sample tested on 29 January

Sample C1 exhibited a curved tearing pattern. The rupture started along a straight path before shifting to the left side of the tissue. Force built up again as the tear temporarily stalled, causing the fracture to redirect toward the right. From there, the tear shifted once more to the left, ultimately ending near the center of the tissue at complete rupture. These three rupture stages correspond to the force drops observed in the force–displacement curves. The ultimate engineering stress was 281.4 kPa, and the reconstructed crack path measured 16.07 mm in length. The sample reached a maximum principal strain of 149% before rupture, with an average strain of 35.5% in the circular area around the crack tip. The normalized initiation energy was 14.3 mJ/mm, and the propagation energy was 1.50 mJ/mm^2.

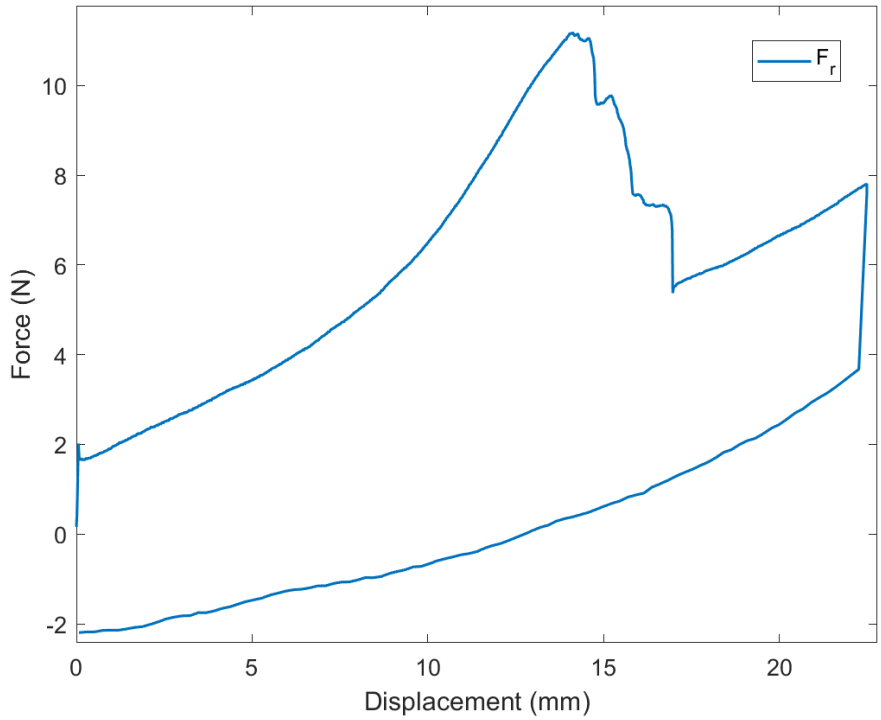

Figure 30: The raw force-displacement curve of sample C1, showing loading and unloading phases during fracture testing. The steep slope at the start of unloading indicates a friction-related artifact resulting from surface wear at the aluminum clamp–arm interface.

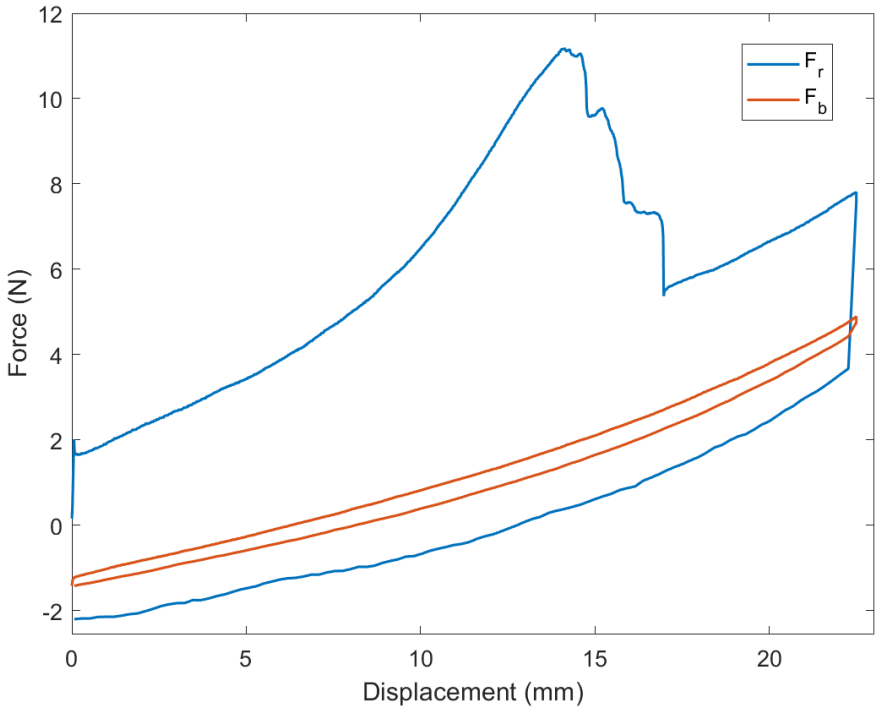

Figure 31: Raw force-displacement curve of C1 plotted alongside beam cycle 8 before offset correction.

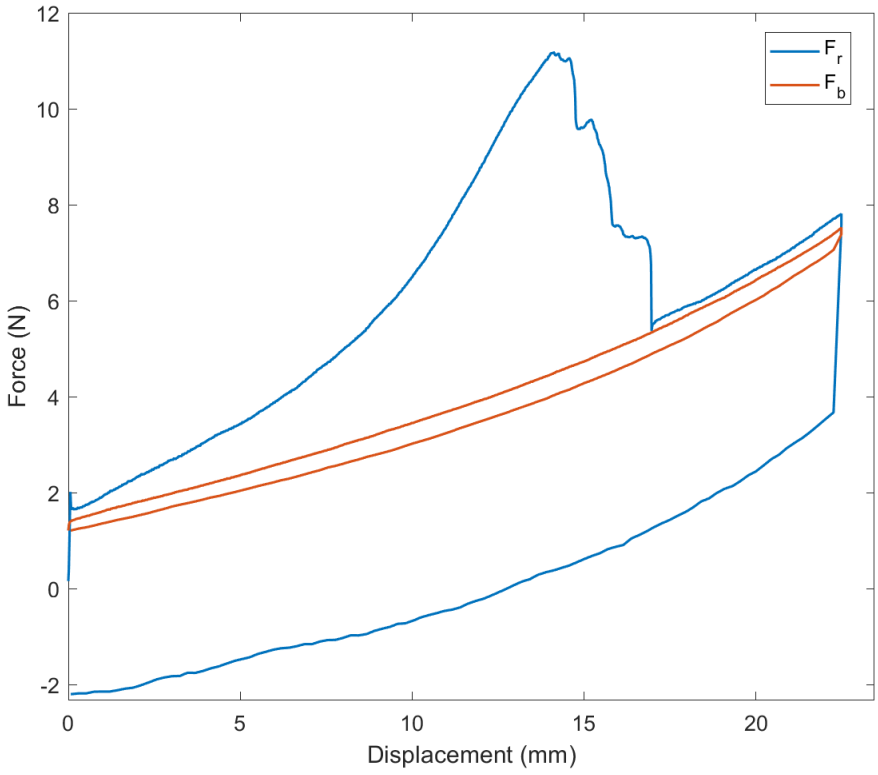

Figure 32: Raw force-displacement curve of C1 and beam cycle 8 after vertical alignment at the rupture point.

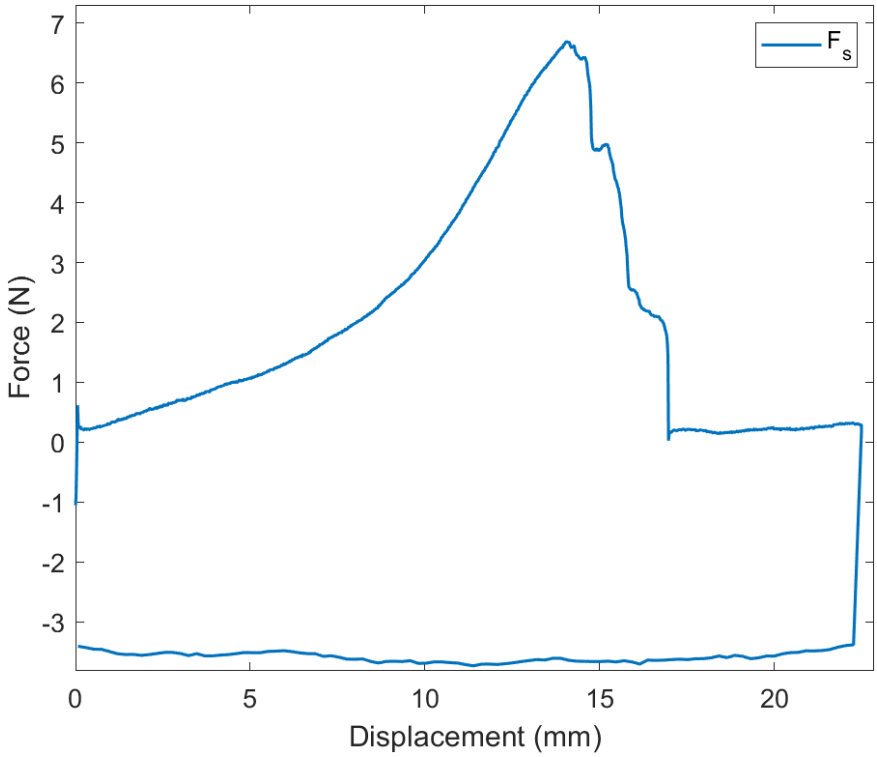

Figure 33: Corrected force-displacement curve of C1 after subtraction of the beam contribution.

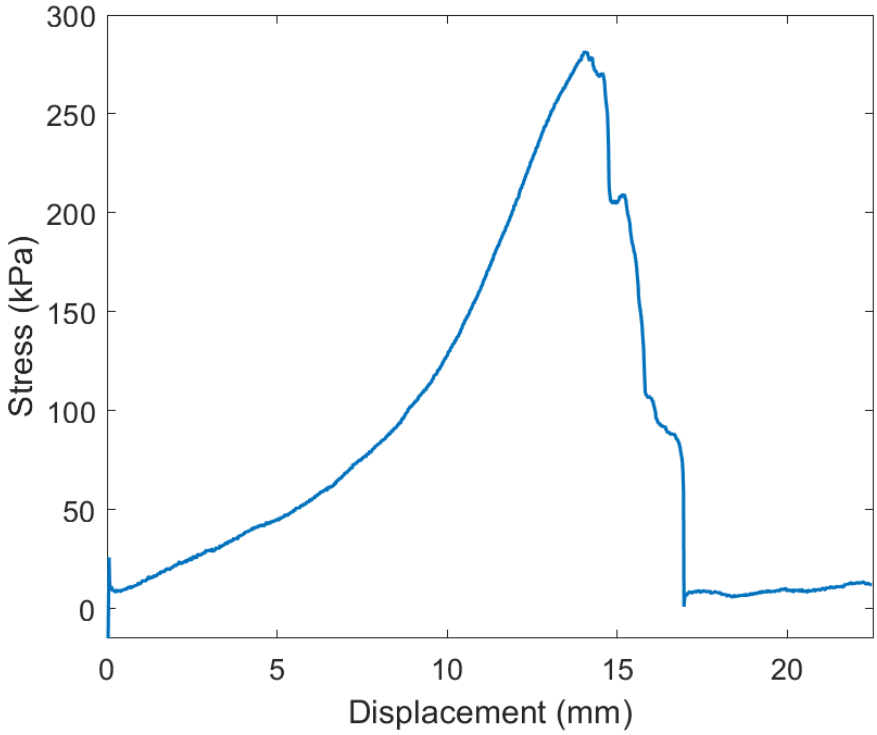

Figure 34: Engineering stress–displacement curve of C1. The peak corresponds to an ultimate engineering stress of 281.4 kPa. The curve shows the loading phase only.

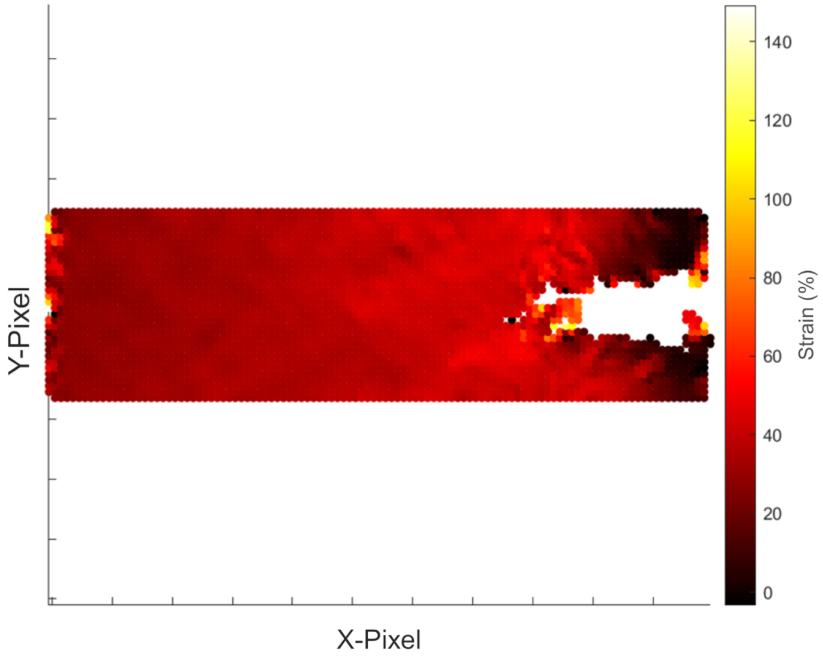

Figure 35: Heatmap of maximal principal strain across the sample surface, generated from the DIC image immediately before crack initiation. Yellow regions indicate high local strain, while red indicates lower strain levels. The ultimate strain was 149%.

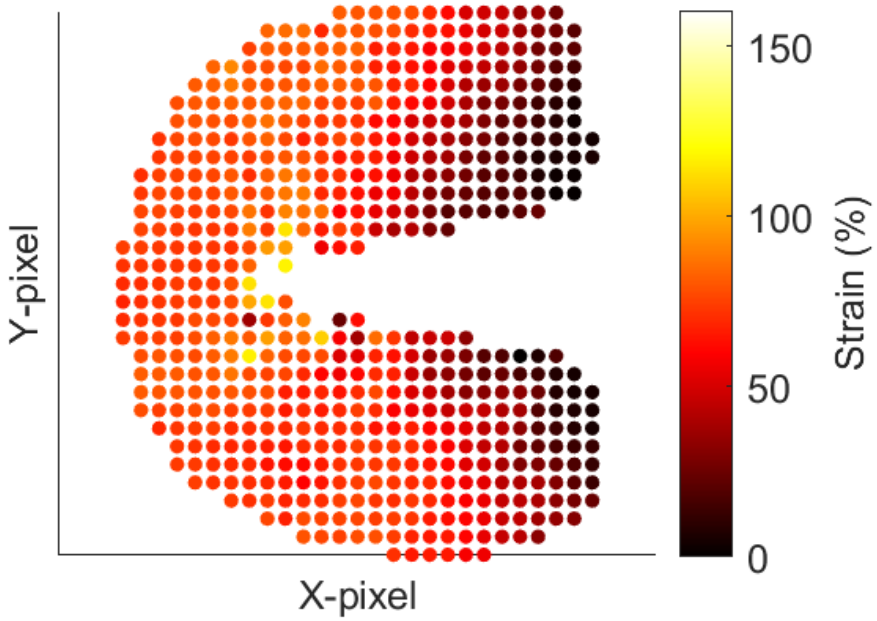

Figure 36: Zoomed-in strain heatmap of a circular region surrounding the crack tip. The average maximal principal strain within this region was 35.5%.

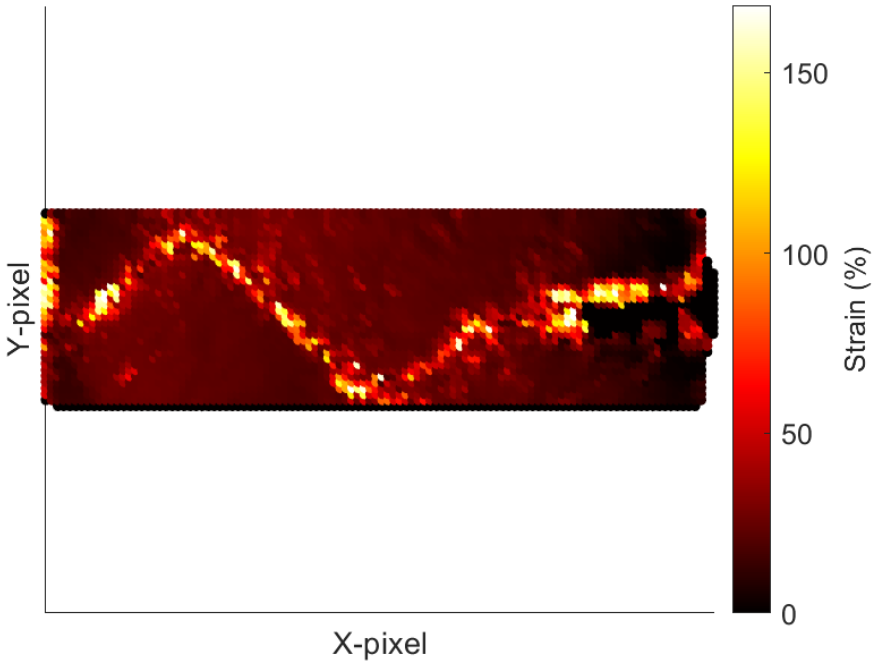

Figure 37: Cumulative heatmap of maximal principal strain recorded per pixel over the entire fracture test. The high-strain pattern visualizes the crack trajectory across the sample surface. Yellow regions represent highly strained areas, whereas red indicates lower strain values.

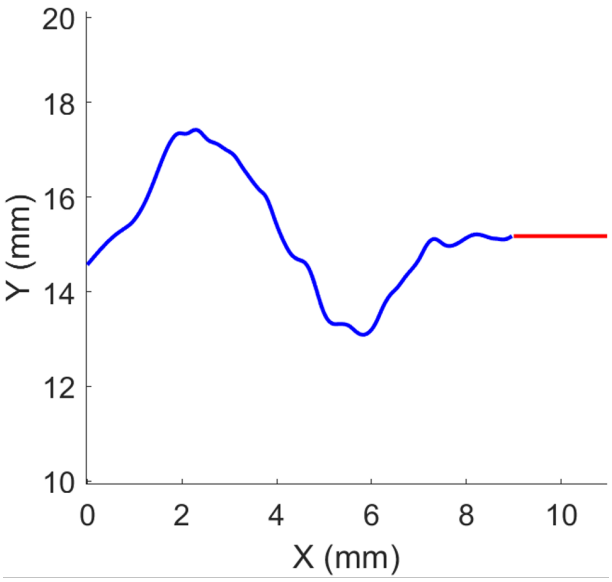

Figure 38: Reconstructed fracture path based on interpolated regions of highest strain. The 2 mm initial notch is shown in red. Pixel coordinates were converted to millimeters using the known sample width for calibration. The total crack path length was estimated to be 16.07 mm.

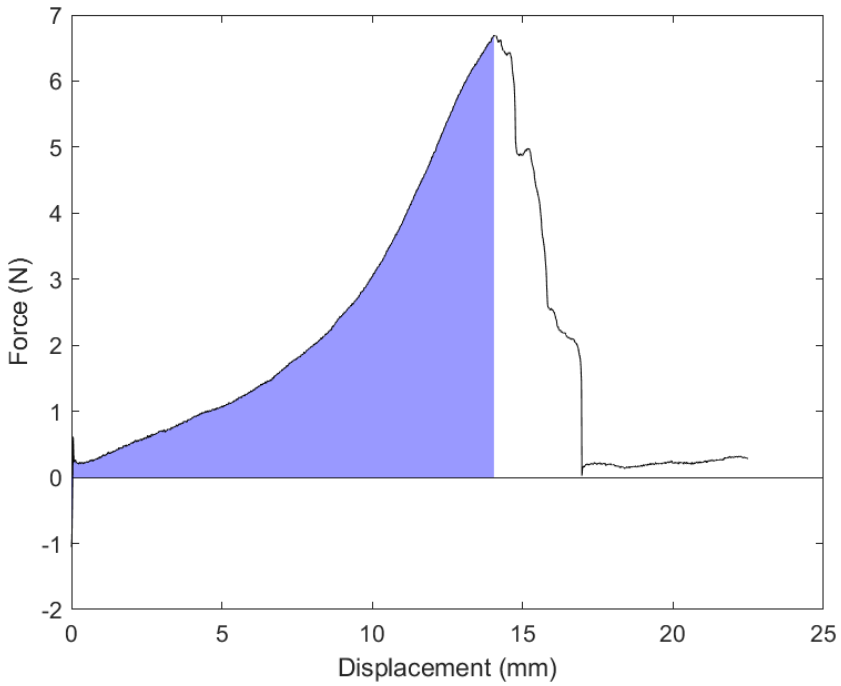

Figure 39: Calculation of the initiation energy. The blue area under the corrected force-displacement curve represents the mechanical work required to initiate rupture. The curve is integrated from the start of the test up to the point of visible crack formation. After normalization, the total initiation energy was 14.3 mJ/mm.

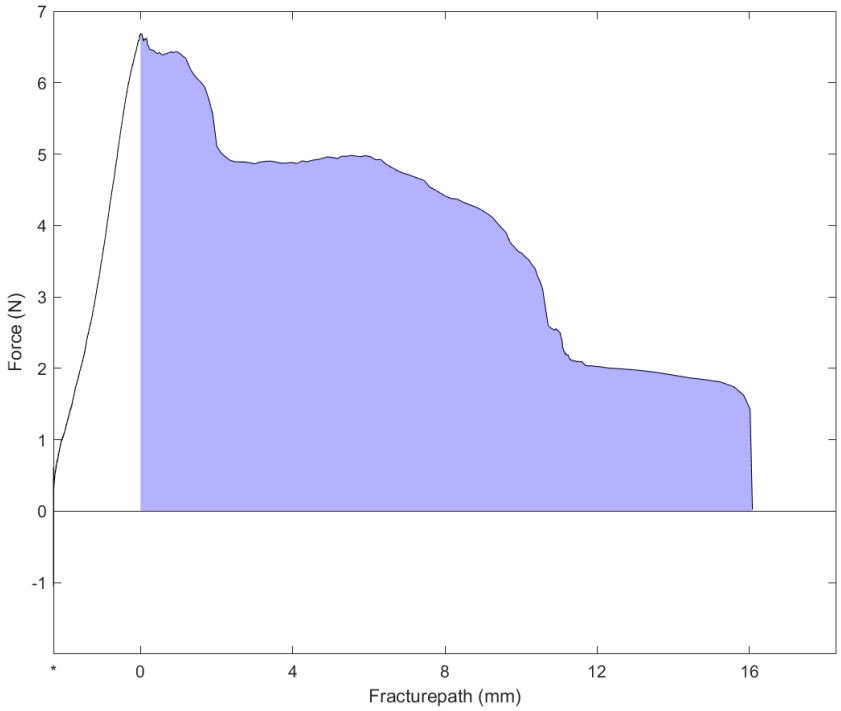

Figure 40: Calculation of the propagation energy. The blue area under the force–fracture path curve represents the mechanical work required to propagate the crack through the sample. After normalization, the dissipation was 1.50 mJ/mm^2.

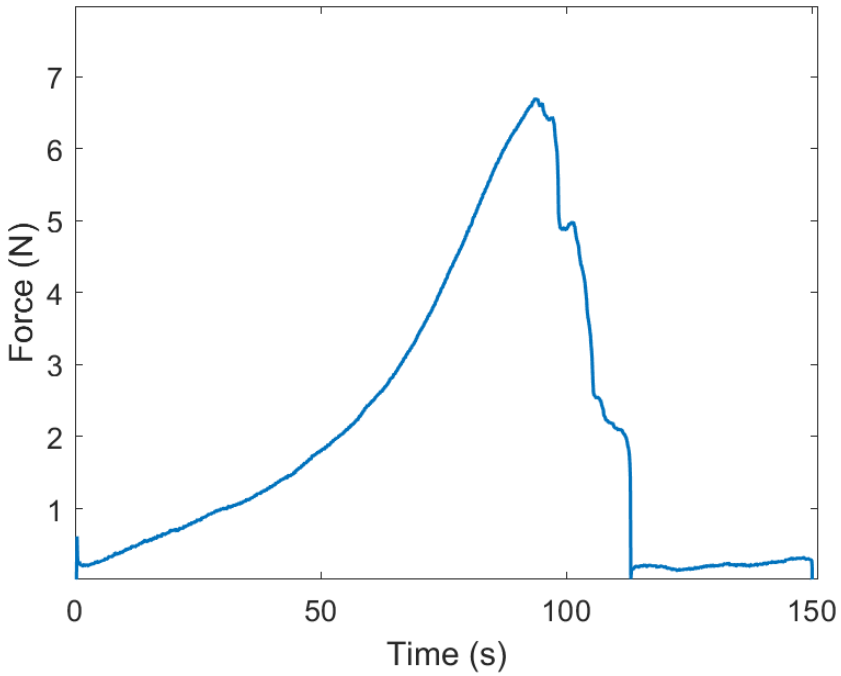

Figure 41: Raw force-time curve recorded by the biaxial testing machine during fracture testing. This dataset provided the force measurements used to construct the force-fracture path curve.

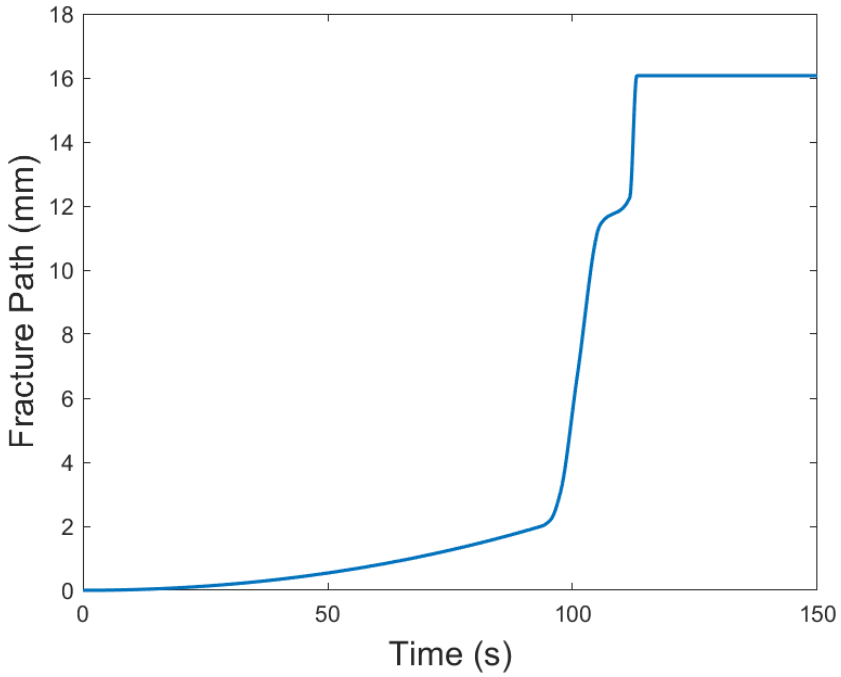

Figure 42: Fracture path–time curve reconstructed by manually analyzing DIC images. Fracture lengths were estimated by identifying the crack location at specific time points, enabling synchronization with the force-time data.

Second circumferential sample tested on 29 January

Sample C2 was used as the representative example in the main paper. Therefore, all fracture behavior analyses are discussed in detail in the main text. This appendix section contains only the raw force-time curve and the manually reconstructed fracture path–time curve that were used to generate the force–fracture path graph.

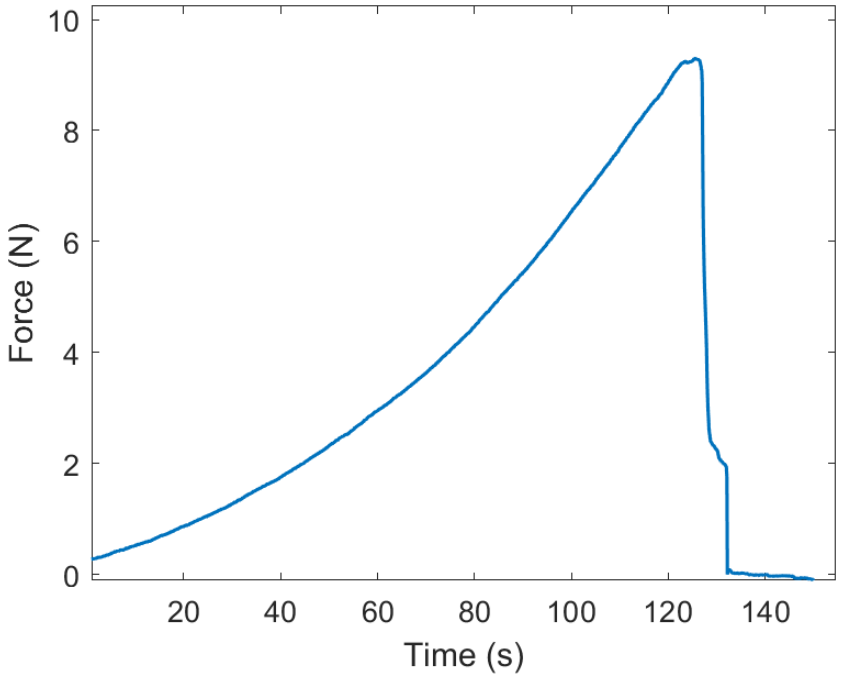

Figure 43: Raw force-time curve recorded by the biaxial testing machine during fracture testing. This dataset provided the force measurements used to construct the force-fracture path curve.

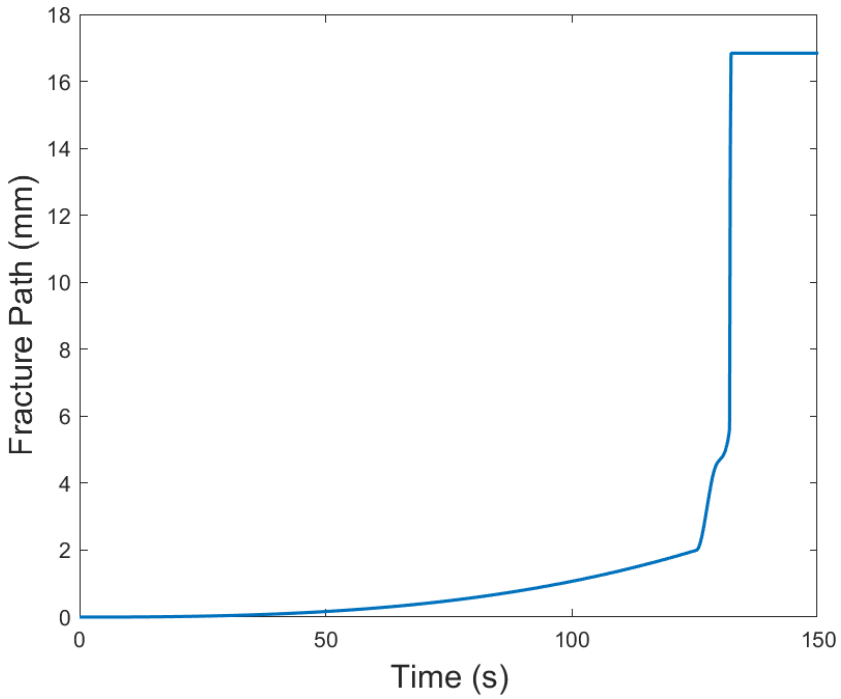

Figure 44: Fracture path–time curve reconstructed by manually analyzing DIC images. Fracture lengths were estimated by identifying the crack location at specific time points, enabling synchronization with the force-time data.

Third circumferential sample tested on 29 January

Sample C3 exhibited a curved tearing pattern. As the load increased, the rupture gradually shifted to the left, continuing in that direction for approximately three-quarters of the fracture path. At that point, the tear stalled and redirected to the right, continuing until complete rupture. These two rupture stages correspond to the force drops observed in the force–displacement curve. The ultimate engineering stress was 335.4 kPa, and the reconstructed crack path measured 14.43 mm in length. The sample reached a maximum principal strain of 170% before rupture, with an average strain of 33.2% in the circular area around the crack tip. The normalized initiation energy was 24.8 mJ/mm, and the propagation energy was 1.77 mJ/mm^2.

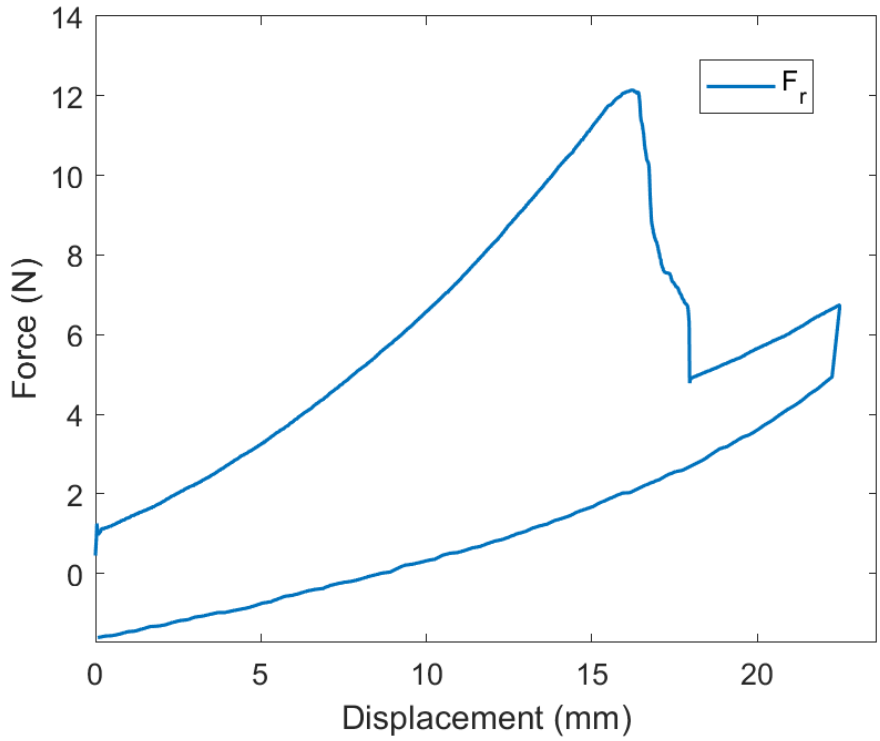

Figure 45: Raw force-displacement curve of C3, showing loading and unloading phases during fracture testing. The steep slope at the start of unloading indicates a friction-related artifact resulting from surface wear at the aluminum clamp–arm interface.

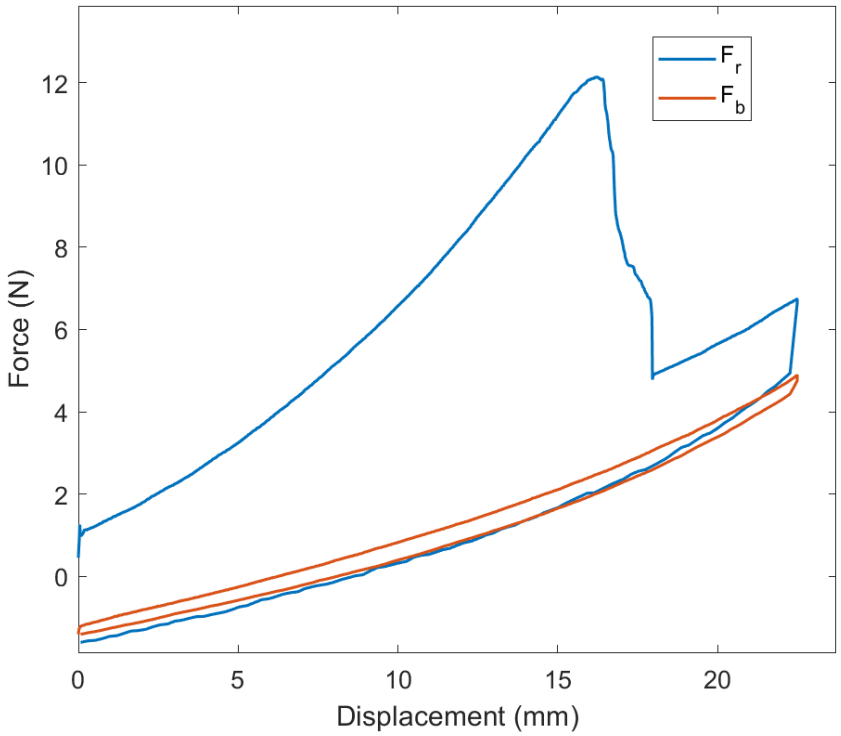

Figure 46: Raw force-displacement curve of C3 plotted alongside beam cycle 8 before offset correction.

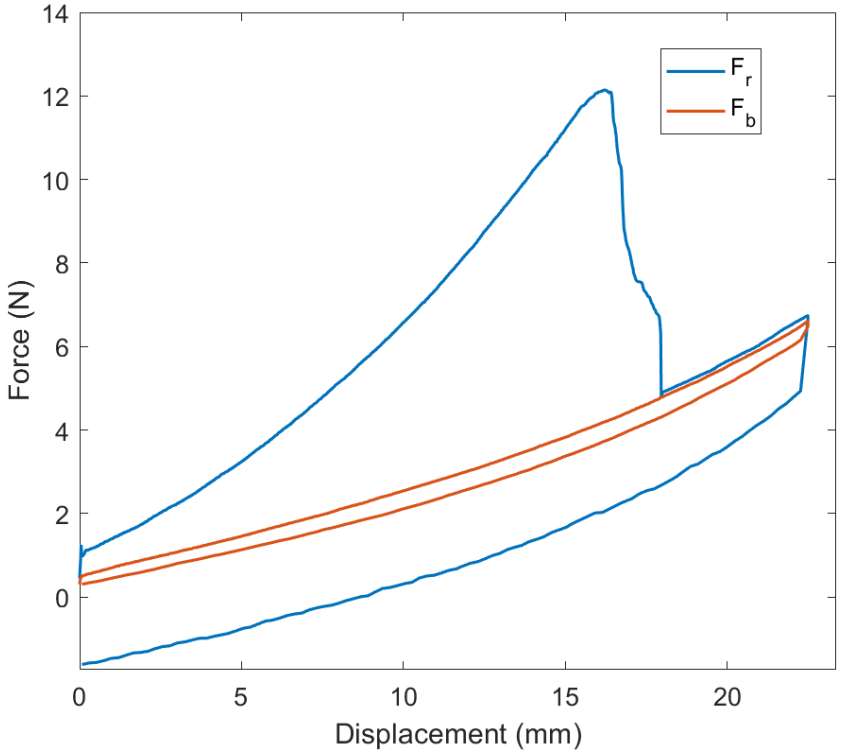

Figure 47: Raw force-displacement curve of C3 and beam cycle 8 after vertical alignment at the rupture point.

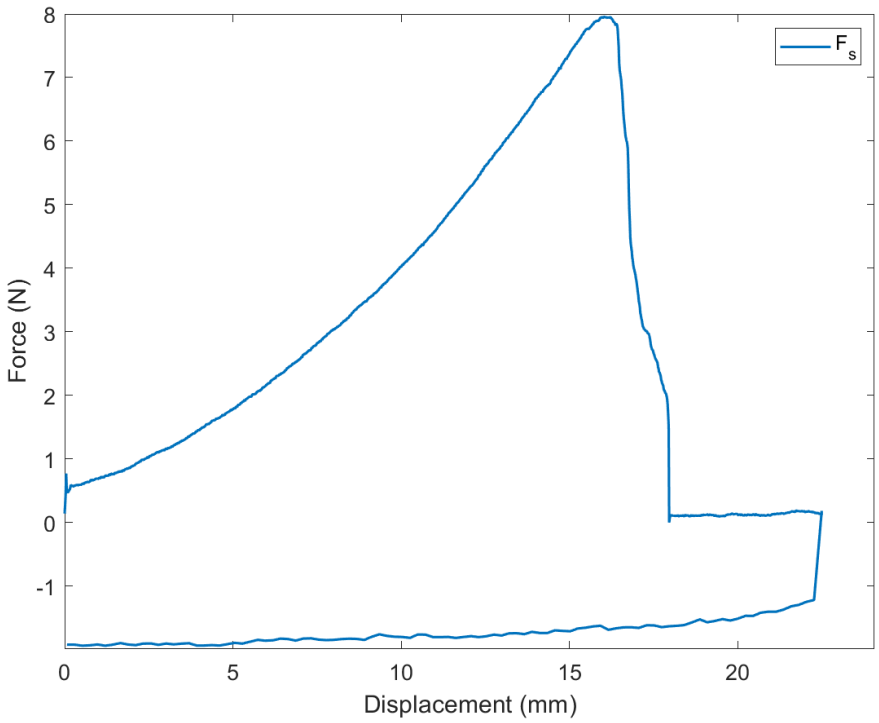

Figure 48: Corrected force-displacement curve of C3 after subtraction of the beam contribution.

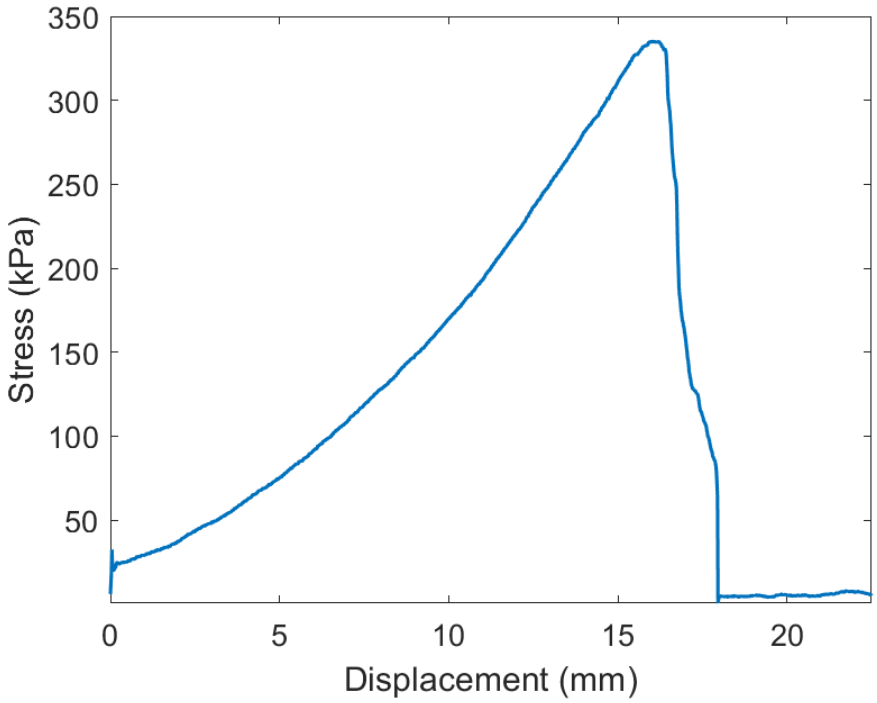

Figure 49: Engineering stress–displacement curve of C3. The peak corresponds to an ultimate engineering stress of 335.4 kPa. The curve shows the loading phase only.

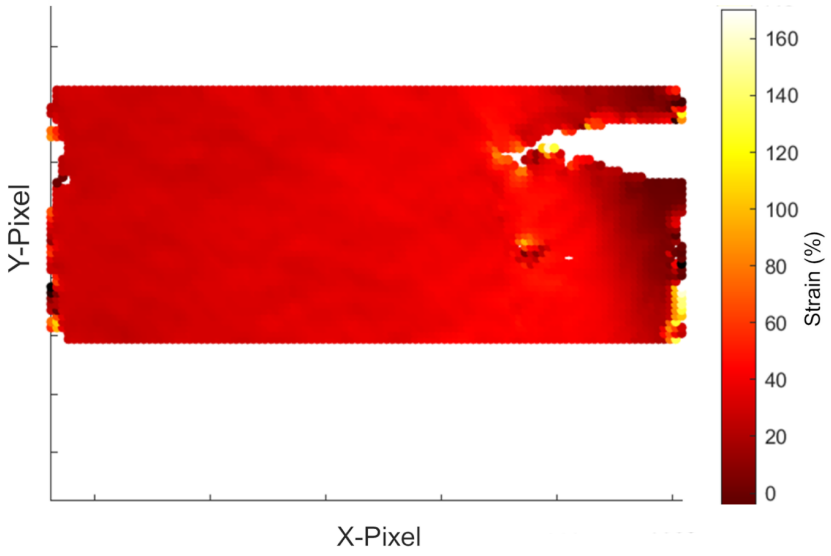

Figure 50: Heatmap of maximal principal strain across the sample surface, generated from the DIC image immediately before crack initiation. Yellow regions indicate high local strain, while red indicates lower strain levels. The ultimate strain was 170%.

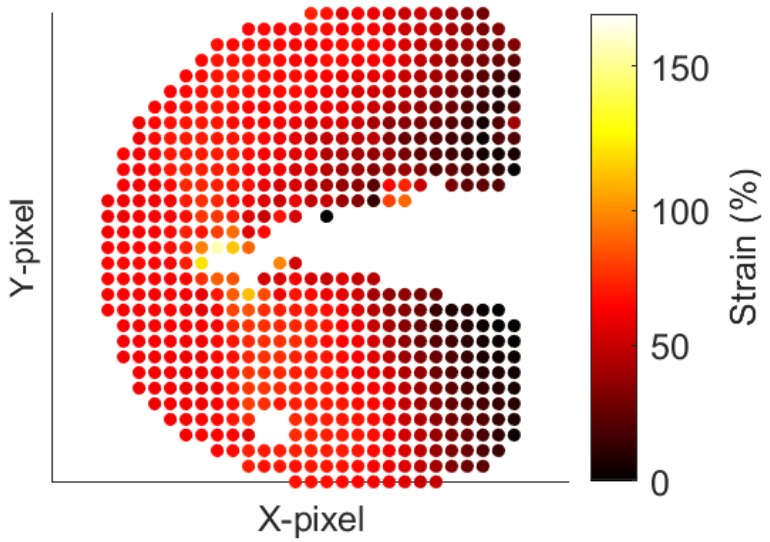

Figure 51: Zoomed-in strain heatmap of a circular region surrounding the crack tip. The average maximal principal strain within this region was 33.2%.

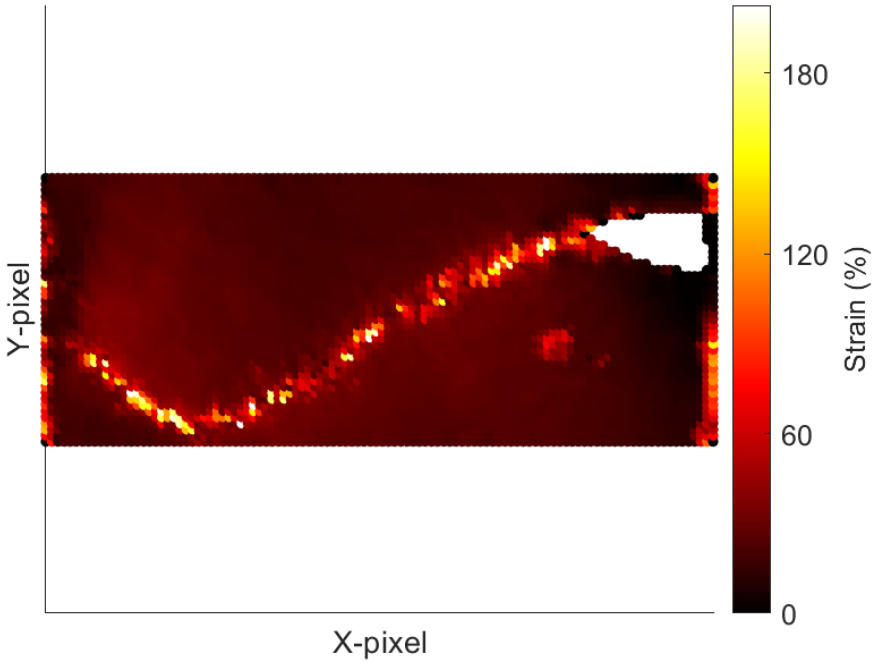

Figure 52: Cumulative heatmap of maximal principal strain recorded per pixel over the entire fracture test. The high-strain pattern visualizes the crack trajectory across the sample surface. Yellow regions represent highly strained areas, whereas red indicates lower strain values.

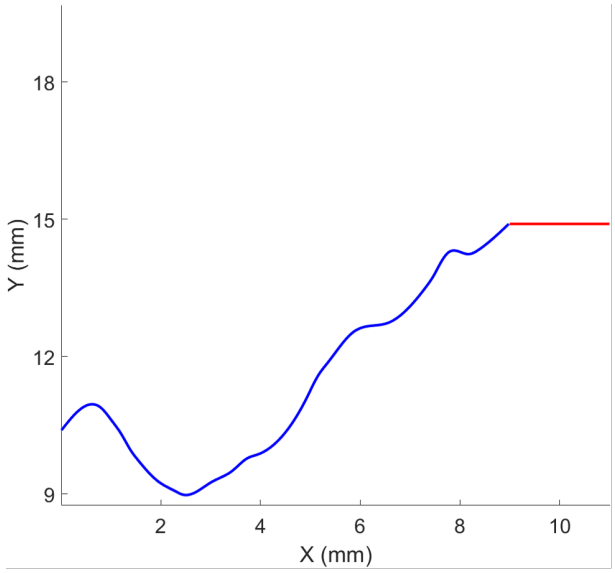

Figure 53: Reconstructed fracture path based on interpolated regions of highest strain. The 2 mm initial notch is shown in red. Pixel coordinates were converted to millimeters using the known sample width for calibration. The total crack path length was estimated to be 14.43 mm.

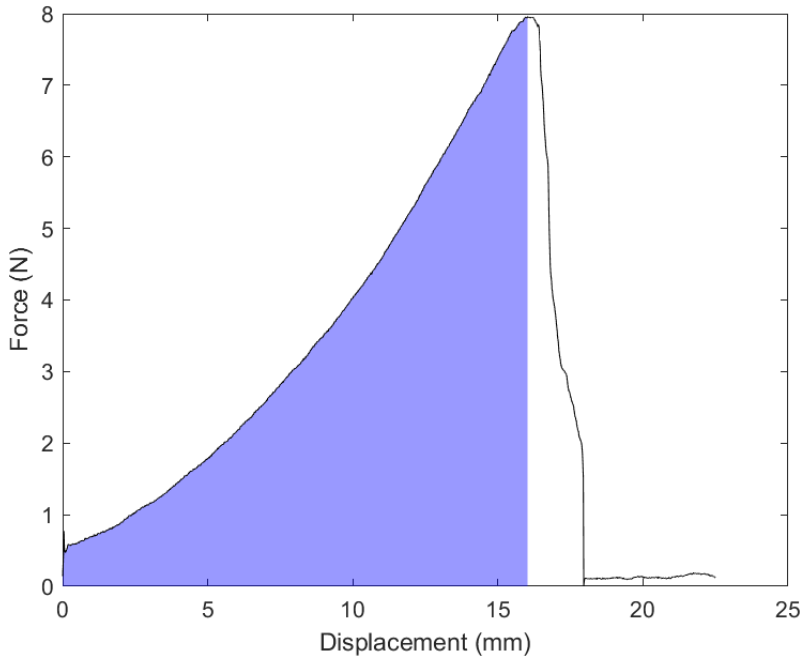

Figure 54: Calculation of the initiation energy. The blue area under the corrected force-displacement curve represents the mechanical work required to initiate rupture. The curve is integrated from the start of the test up to the point of visible crack formation. After normalization, the total initiation energy was 24.8 mJ/mm.

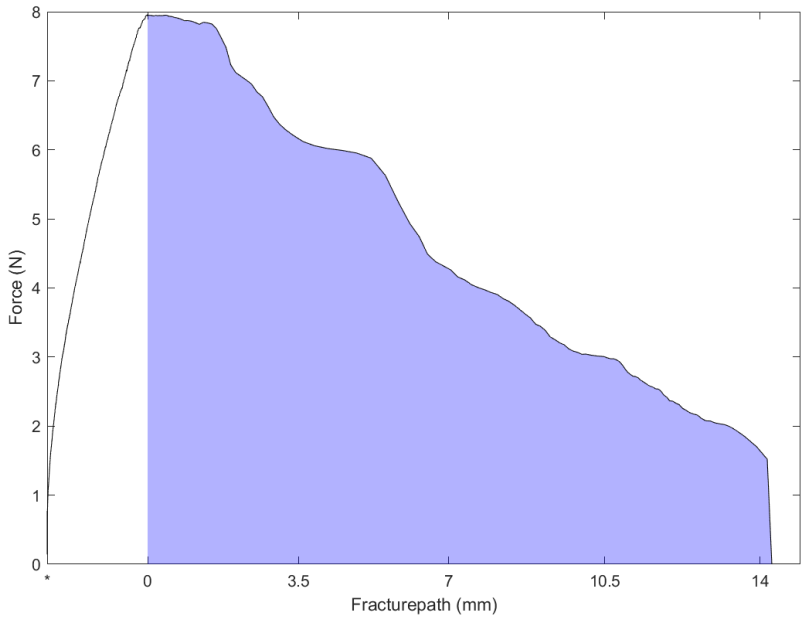

Figure 55: Calculation of the propagation energy. The blue area under the force–fracture path curve represents the mechanical work required to propagate the crack through the sample. After normalization, the dissipation was 1.77 mJ/mm^2.

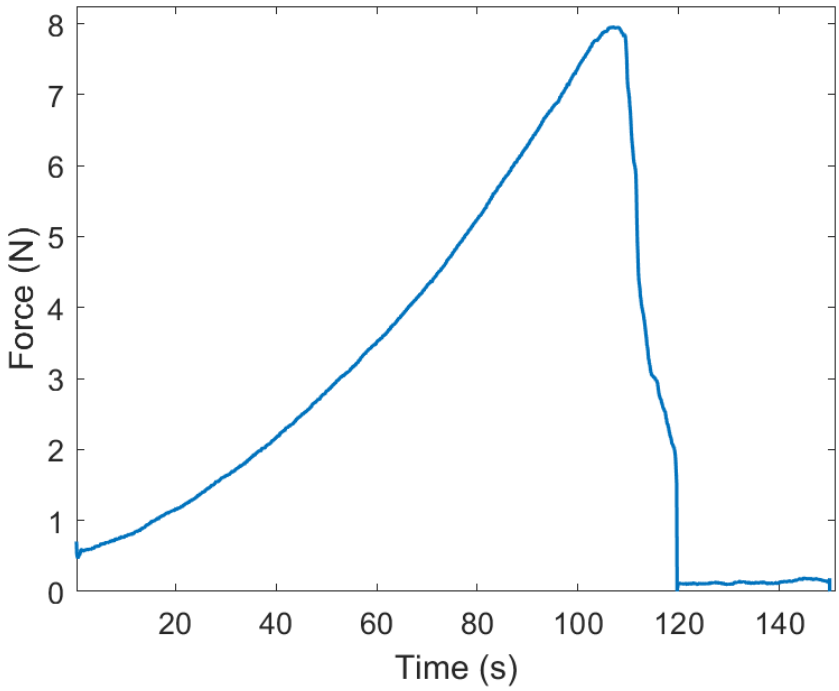

Figure 56: Raw force-time curve recorded by the biaxial testing machine during fracture testing. This dataset provided the force measurements used to construct the force-fracture path curve.

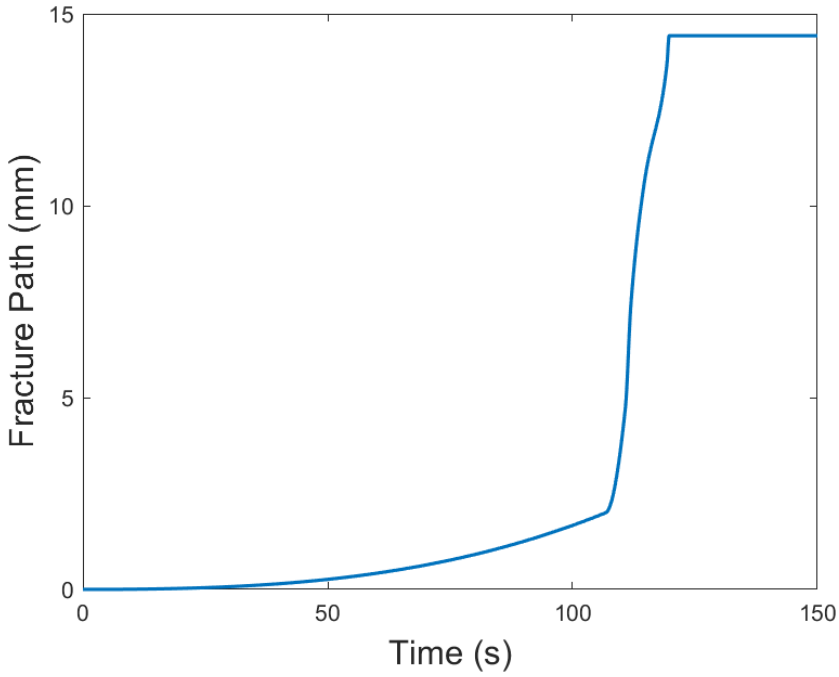

Figure 57: Fracture path–time curve reconstructed by manually analyzing DIC images. Fracture lengths were estimated by identifying the crack location at specific time points, enabling synchronization with the force-time data.

Fourth circumferential sample tested on 29 January

The intima and media layers of C4 tore separately, leading to unreliable DIC analysis (Figure 50a). As shown in Figure 50b, the intima showed a straight tearing pattern, whereas the underlying media followed a curved rupture path. The two-phased curved tearing response of the media is shown in the force-displacement curve, which exhibits two steep drops following the peak force. The ultimate engineering stress reached 290.2 kPa. Due to the distinct separation of the intimal layer, strain data, fracture path reconstruction, and propagation energy were not calculated for this sample. The normalized initiation energy was 23.0 mJ/mm.

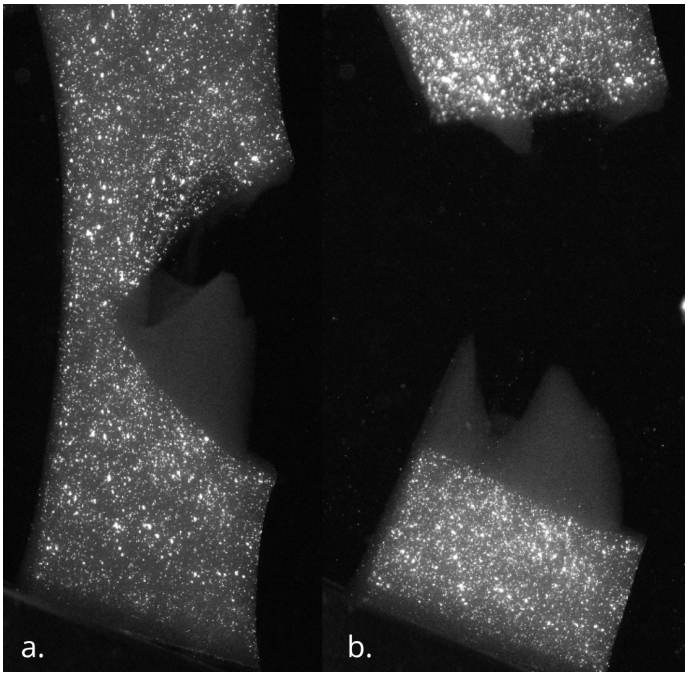

Figure 58: (a) DIC image of C4 during rupture, showing the separation of intima and media layers. (b) Final rupture stage, where the intima layer shows a straight tearing pattern. In contrast, the media layer reveals a two-directional curved tear.

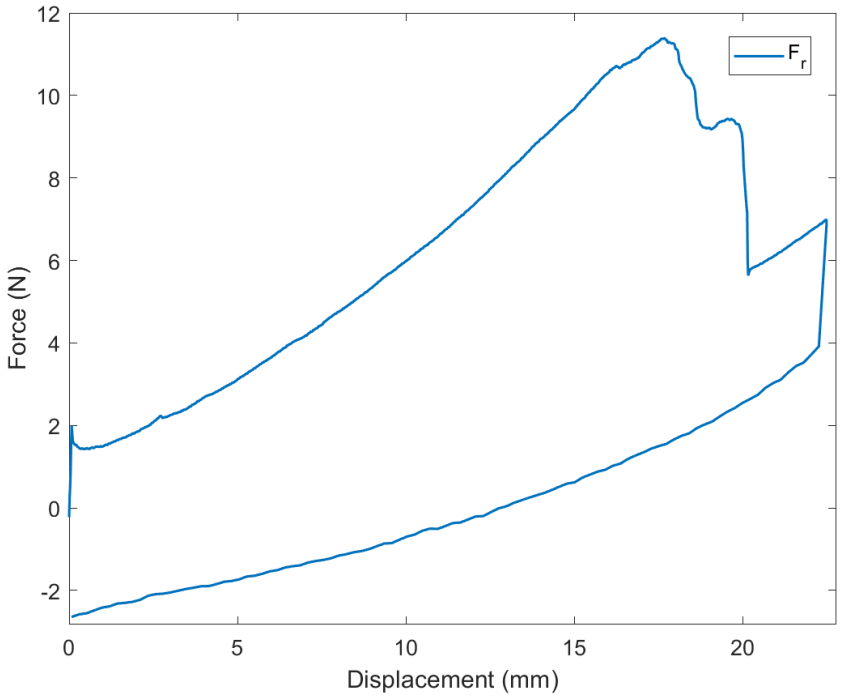

Figure 59: Raw force-displacement curve of C4, showing loading and unloading phases during fracture testing. The steep slope at the start of unloading indicates a friction-related artifact resulting from surface wear at the aluminum clamp–arm interface.

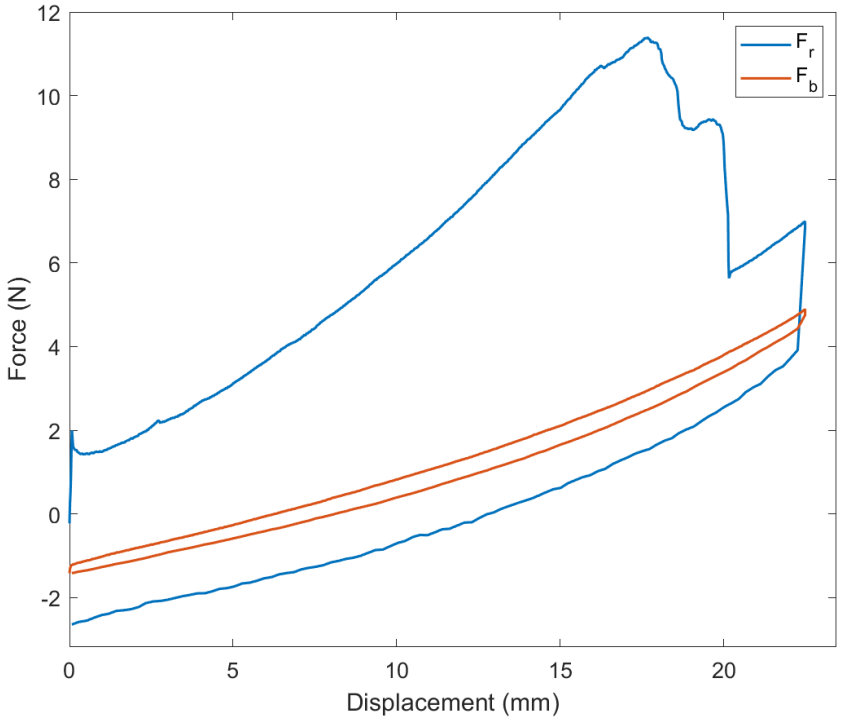

Figure 60: Raw force-displacement curve of C4 plotted alongside beam cycle 8 before offset correction.

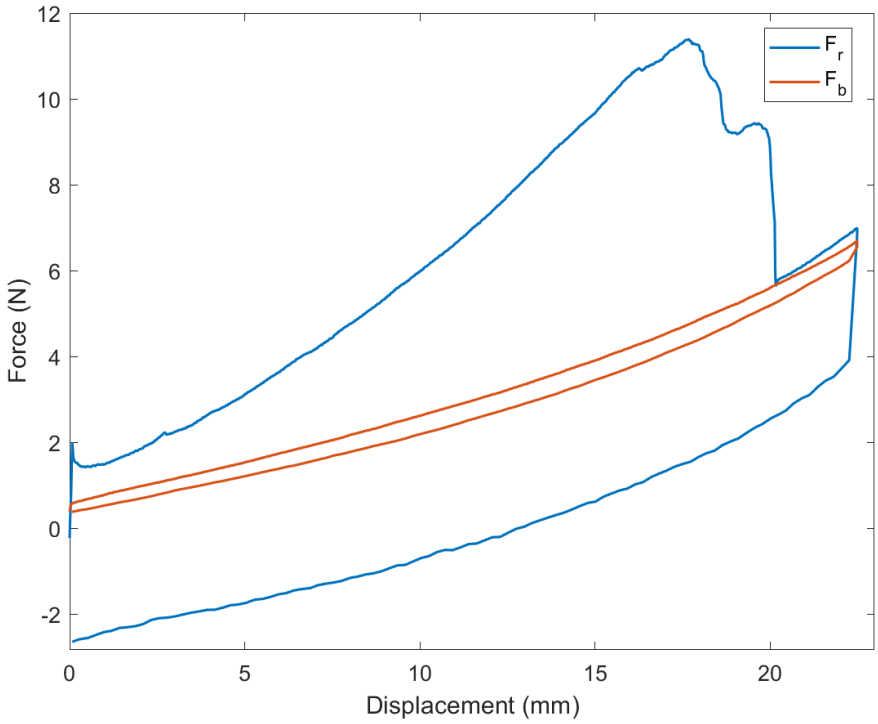

Figure 61: Raw force-displacement curve of C4 and beam cycle 8 after vertical alignment at the rupture point.

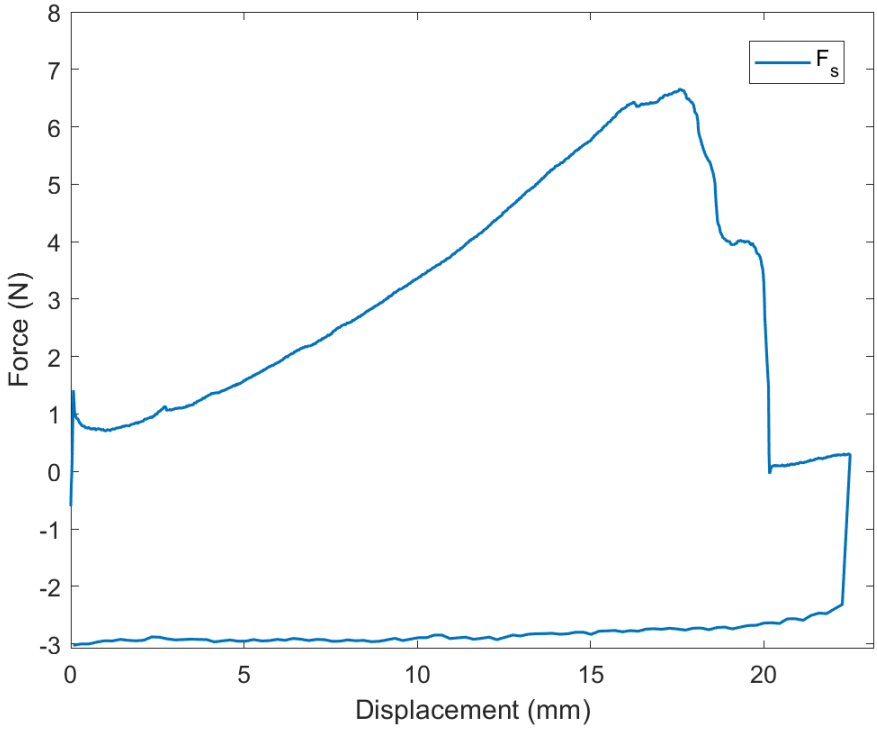

Figure 62: Corrected force-displacement curve of C4 after subtraction of the beam contribution.

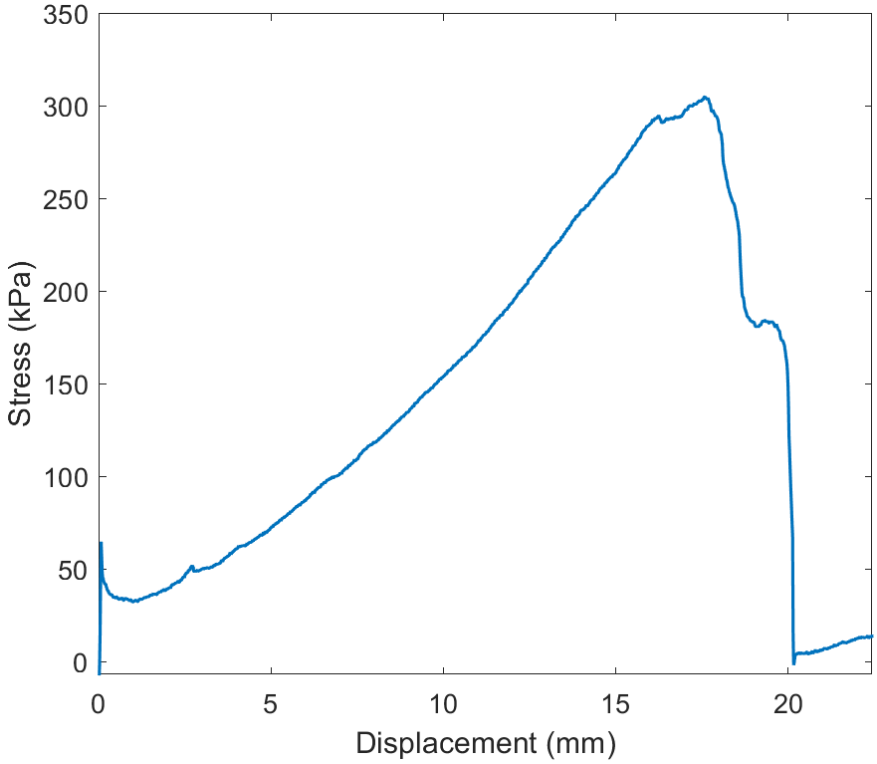

Figure 63: Engineering stress–displacement curve of C4. The peak corresponds to an ultimate engineering stress of 290.2 kPa. The curve shows the loading phase only.

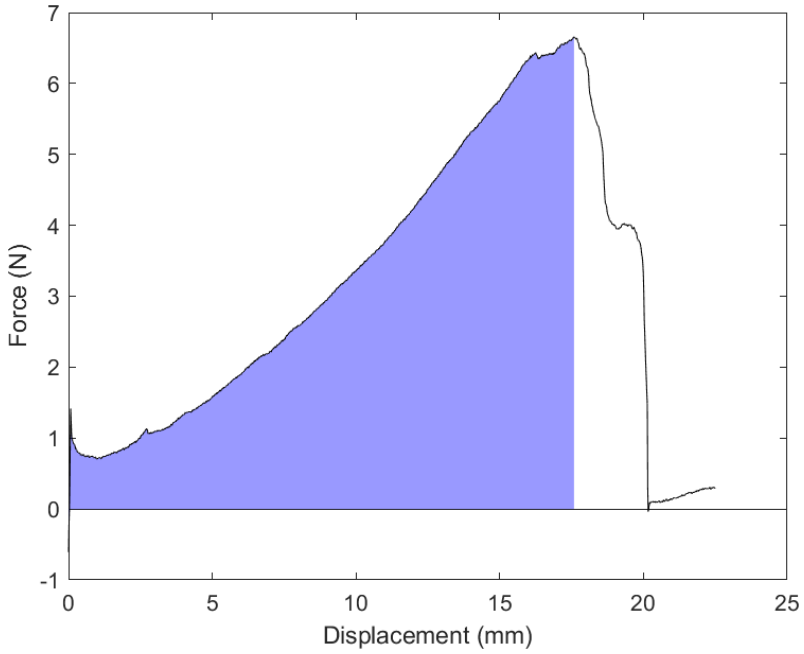

Figure 64: Calculation of the propagation energy. The blue area under the force–fracture path curve represents the mechanical work required to propagate the crack through the sample. After normalization, the total propagation energy was 23.0 mJ/mm.

The seventh longitudinal sample, tested on 30 January

Sample L7 exhibited a straight tearing pattern during fracture testing. The quality of the DIC data for this sample was lower compared to others. The speckle pattern applied to the intimal surface lacked contrast quality, making it difficult for the DIC software to track deformation accurately. As a result, the pixel subset size had to be increased to improve pattern recognition, which decreased the accuracy of the strain measurements.
All fracture behavior calculations could still be performed despite the limitations. The ultimate engineering stress was 215.9 kPa, and the reconstructed crack path length was 12.92 mm. The sample reached an ultimate strain of 81% before rupture, with an average strain of 37.2% in the circular region surrounding the crack tip. The normalized initiation energy was calculated to be 15.7 mJ/mm, and the propagation energy was 1.06 mJ/mm^2.

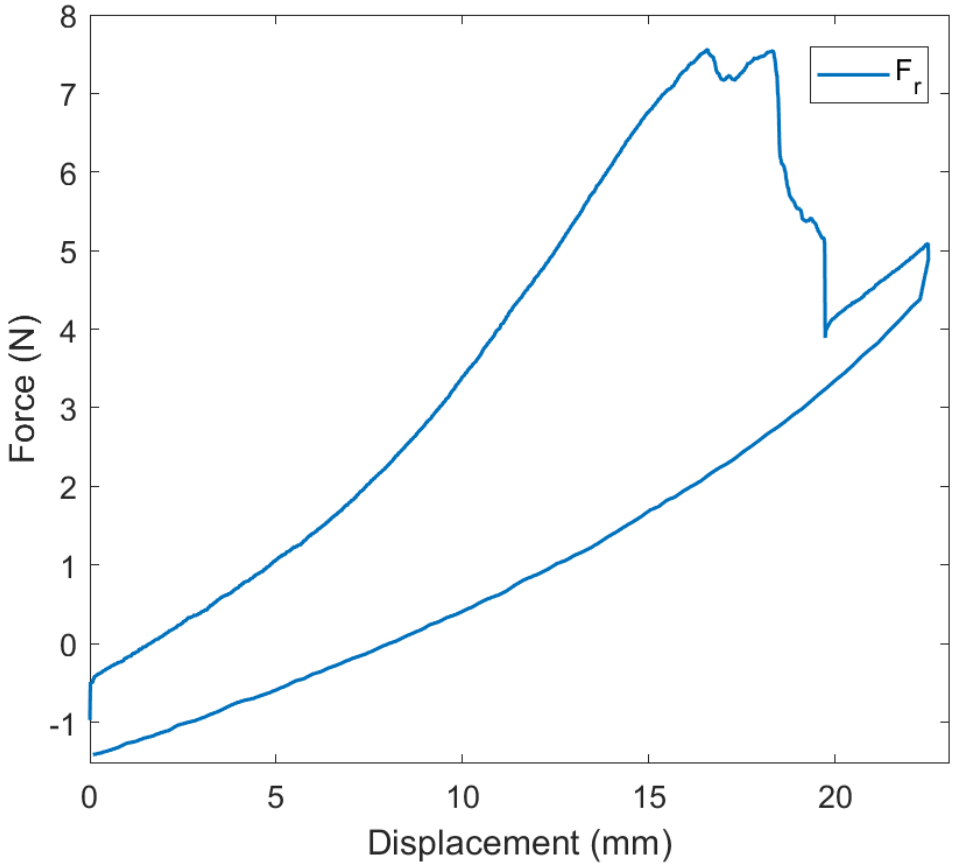

Figure 65: Raw force-displacement curve of L7, showing loading and unloading phases during fracture testing. The steep slope at the start of unloading indicates a friction-related artifact resulting from surface wear at the aluminum clamp–arm interface.

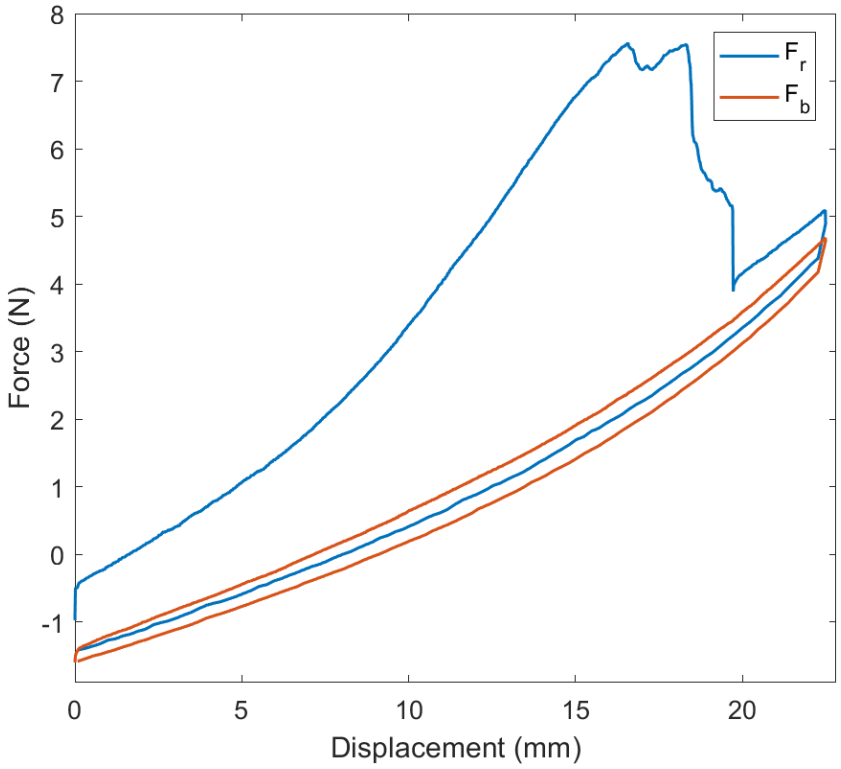

Figure 66: Raw force-displacement curve of L7 plotted alongside beam cycle 6 before offset correction.

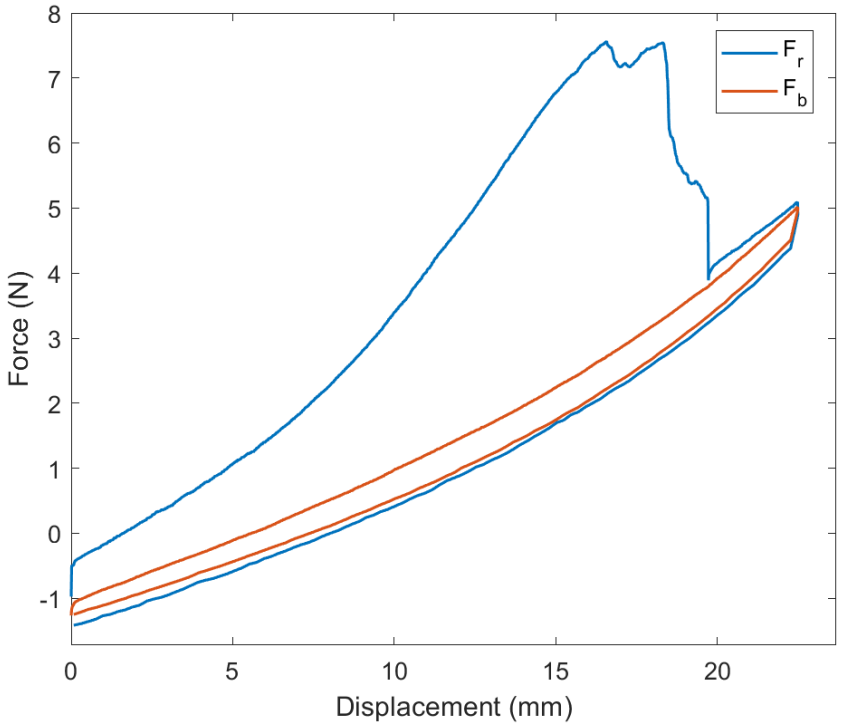

Figure 67: Raw force-displacement curve of L7 and beam cycle 6 after vertical alignment at the rupture point.

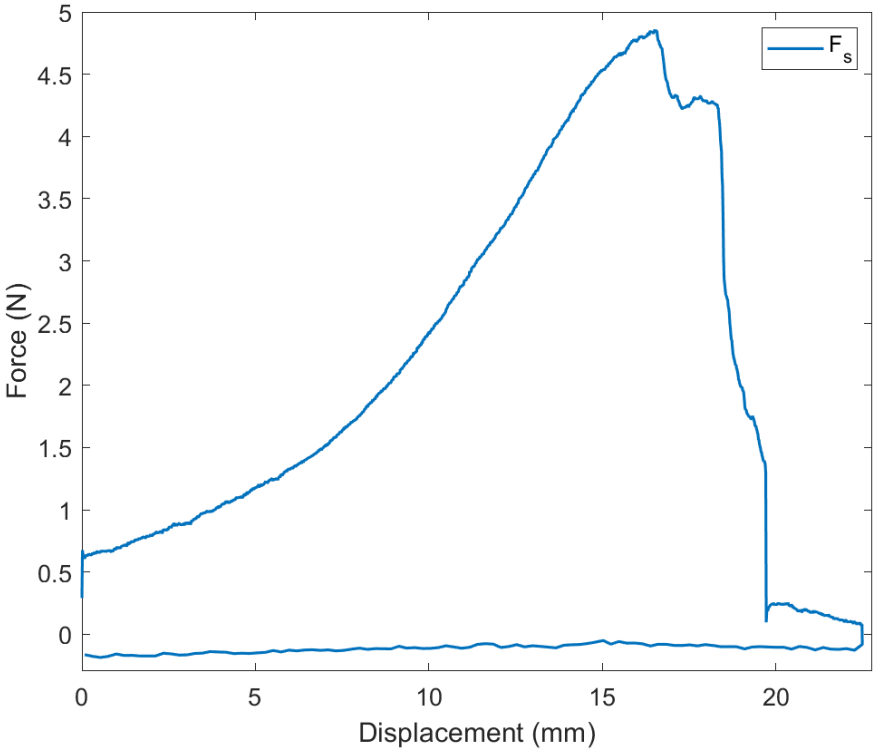

Figure 68: Corrected force-displacement curve of L7 after subtraction of the beam contribution.

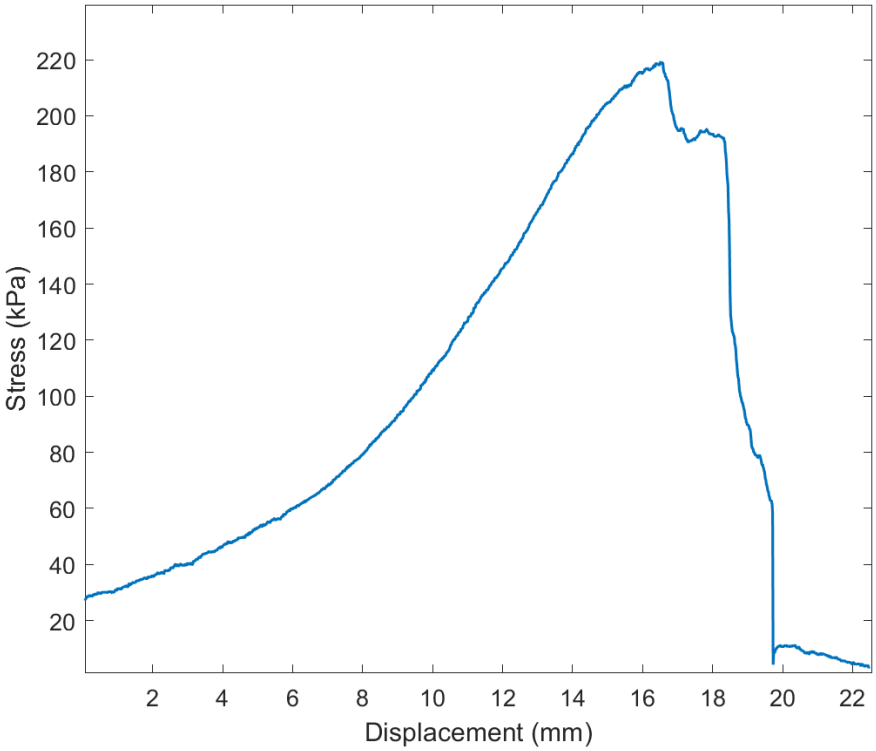

Figure 69: Engineering stress–displacement curve of L7. The peak corresponds to an ultimate engineering stress of 215.9 kPa. The curve shows the loading phase only.

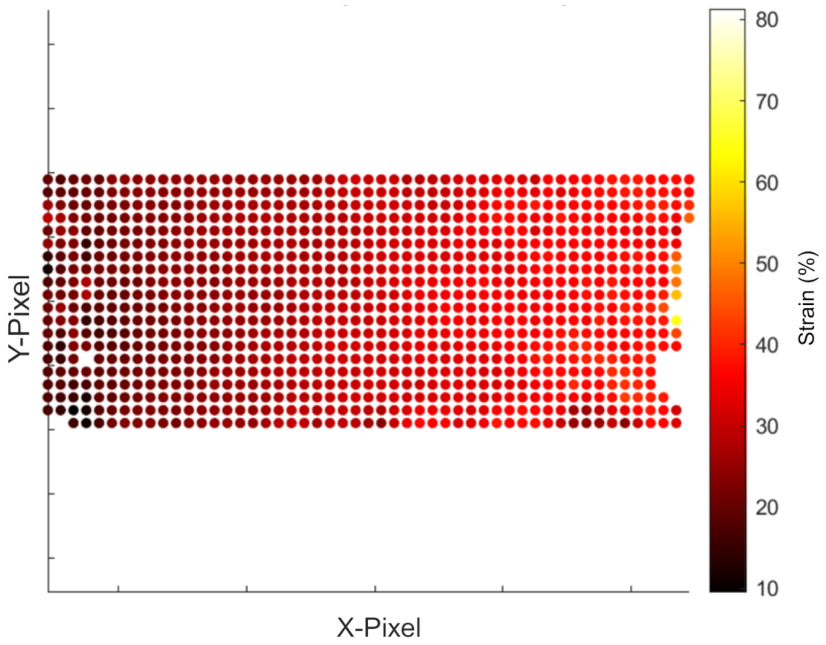

Figure 70: Heatmap of maximal principal strain across the sample surface, generated from the DIC image immediately before crack initiation. Yellow regions indicate high local strain, while red indicates lower strain levels. The ultimate strain was 81%.

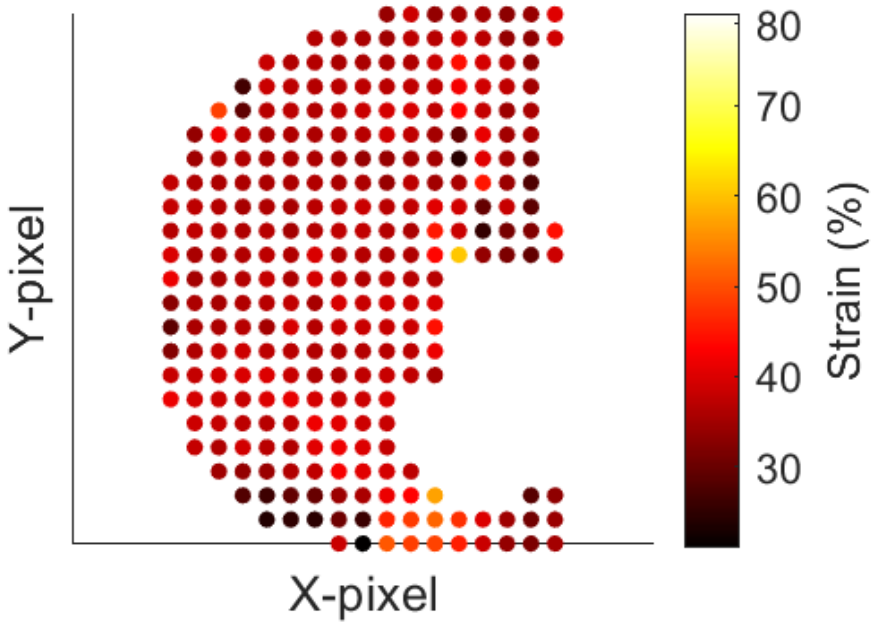

Figure 71: Zoomed-in strain heatmap of a circular region surrounding the crack tip. The average maximal principal strain within this region was 37.2%.

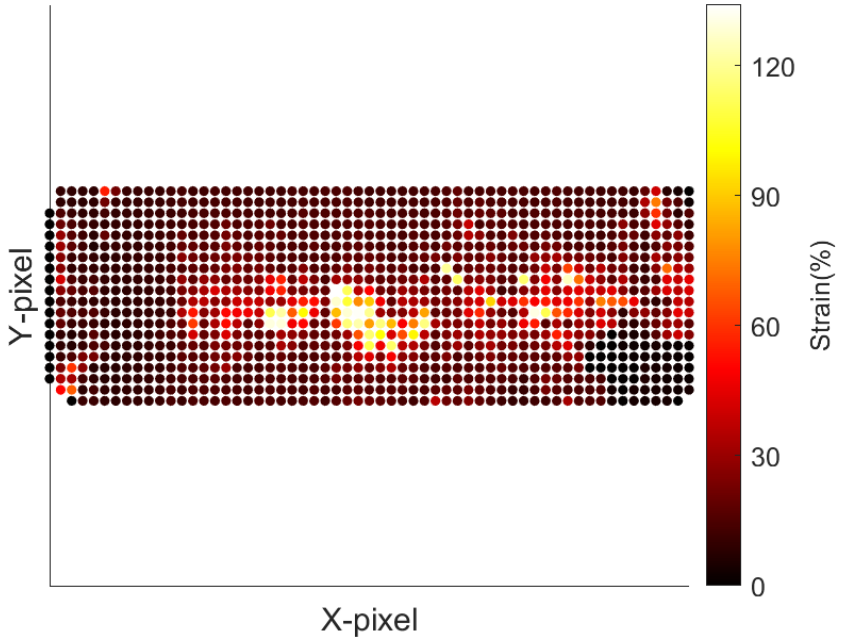

Figure 72: Cumulative heatmap of maximal principal strain recorded per pixel over the entire fracture test. The high-strain pattern visualizes the crack trajectory across the sample surface. Yellow regions represent highly strained areas, whereas red indicates lower strain values.

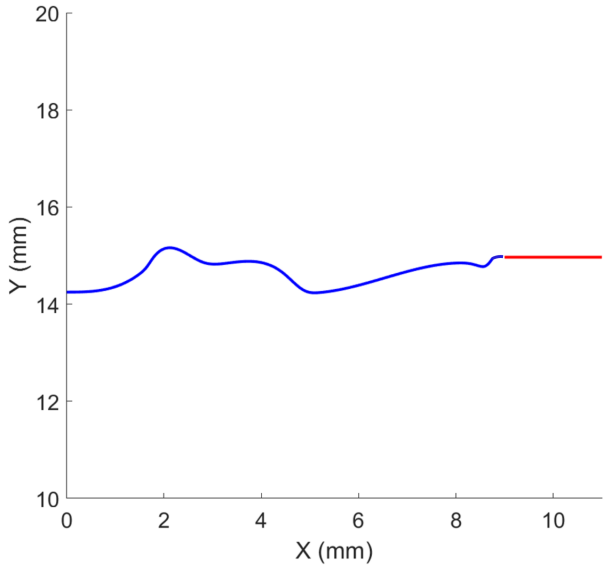

Figure 73: Reconstructed fracture path based on interpolated regions of highest strain. The 2 mm initial notch is shown in red. Pixel coordinates were converted to millimeters using the known sample width for calibration. The total crack path length was estimated to be 12.92 mm.

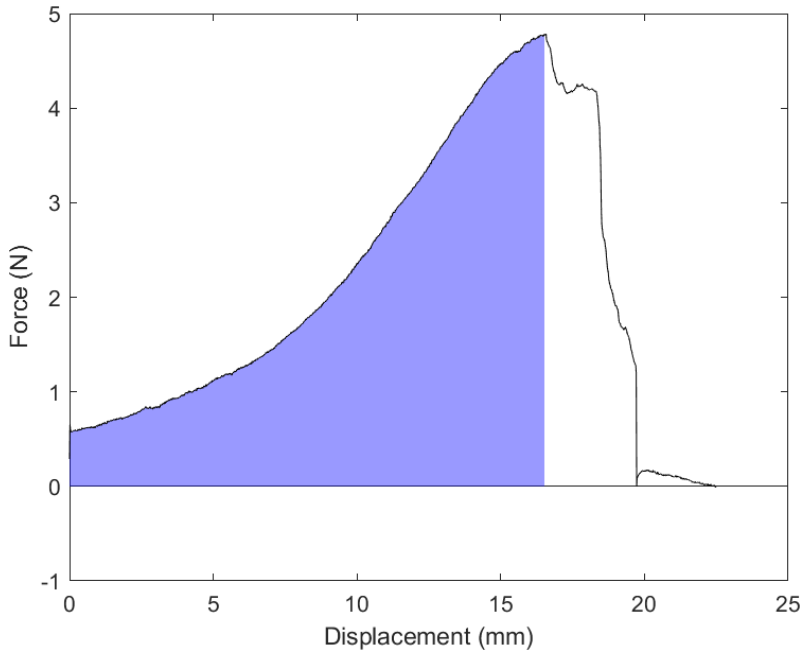

Figure 74: Calculation of the initiation energy. The blue area under the corrected force-displacement curve represents the mechanical work required to initiate rupture. The curve is integrated from the start of the test up to the point of visible crack formation. After normalization, the total initiation energy was 15.7 mJ/mm.

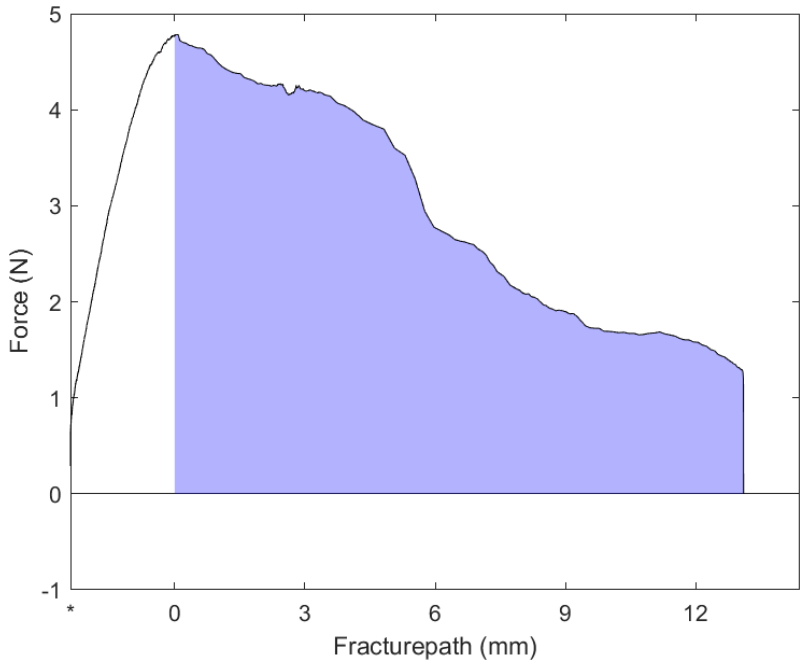

Figure 75: Calculation of the propagation energy. The blue area under the force–fracture path curve represents the mechanical work required to propagate the crack through the sample. After normalization, the dissipation was 1.06 mJ/mm^2.

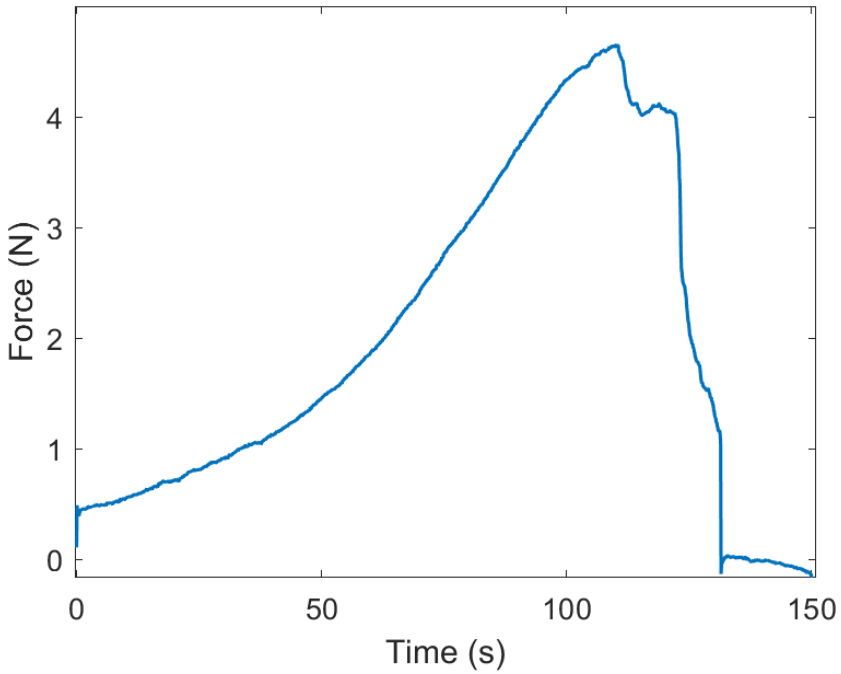

Figure 76: Raw force-time curve recorded by the biaxial testing machine during fracture testing. This dataset provided the force measurements used to construct the force-fracture path curve.

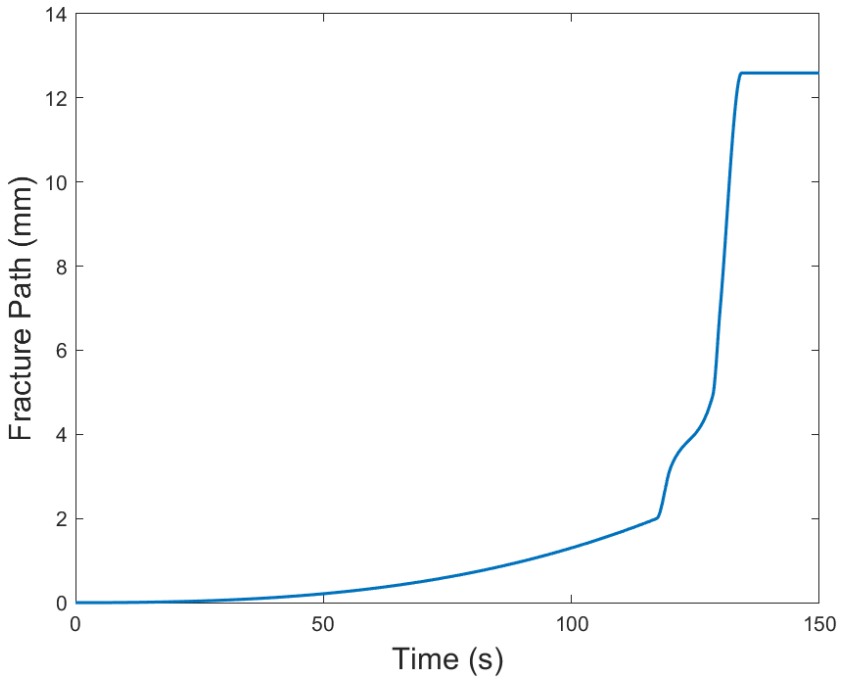

Figure 77: Fracture path–time curve reconstructed by manually analyzing DIC images. Fracture lengths were estimated by identifying the crack location at specific time points, enabling synchronization with the force-time data.

The eighth circumferential sample tested on 30 January

Sample C8 exhibited a curved rupture trajectory. The tear started with a slow propagation to the left. One-third into the fracture path, it shifted to the right, corresponding to the first steep drop in the force-displacement curve. The second steep drop marks the crack redirecting back to the left, ultimately completing the rupture near the center of the sample. The ultimate engineering stress was 196.4 kPa, and the reconstructed crack path measured 15.25 mm in length. The sample reached a maximum principal strain of 153% before rupture, with an average strain of 41.4% in the circular region around the crack tip. The normalized initiation energy was 17.4 mJ/mm, and the propagation energy was 1.31 mJ/mm^2.

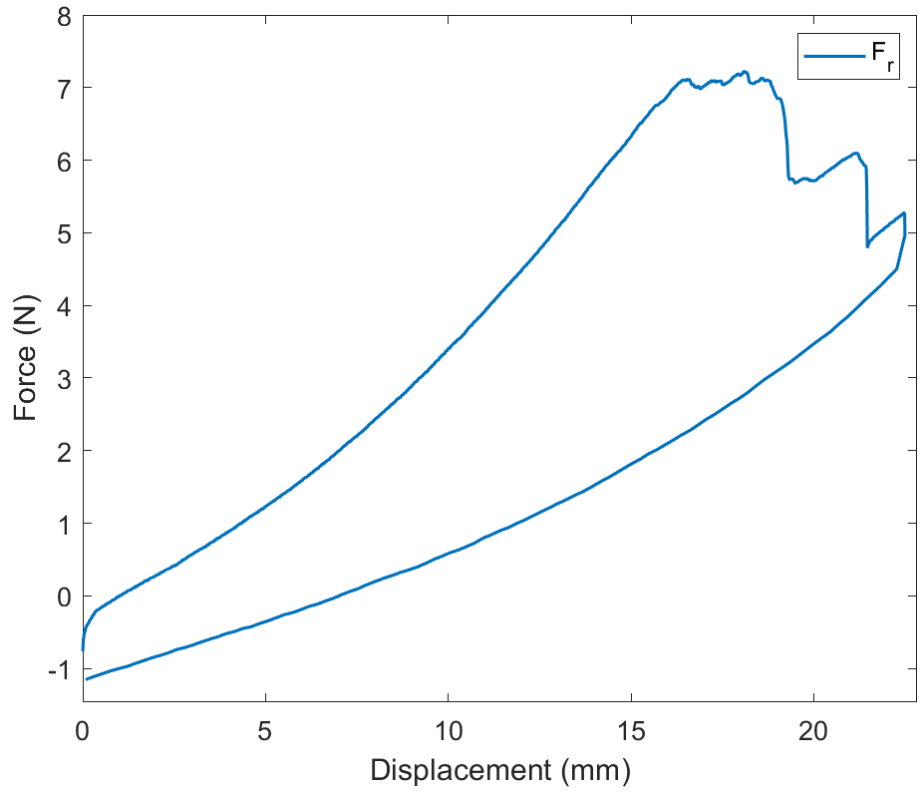

Figure 78: Raw force-displacement curve of C8, showing loading and unloading phases during fracture testing. The steep slope at the start of unloading indicates a friction-related artifact resulting from surface wear at the aluminum clamp–arm interface.

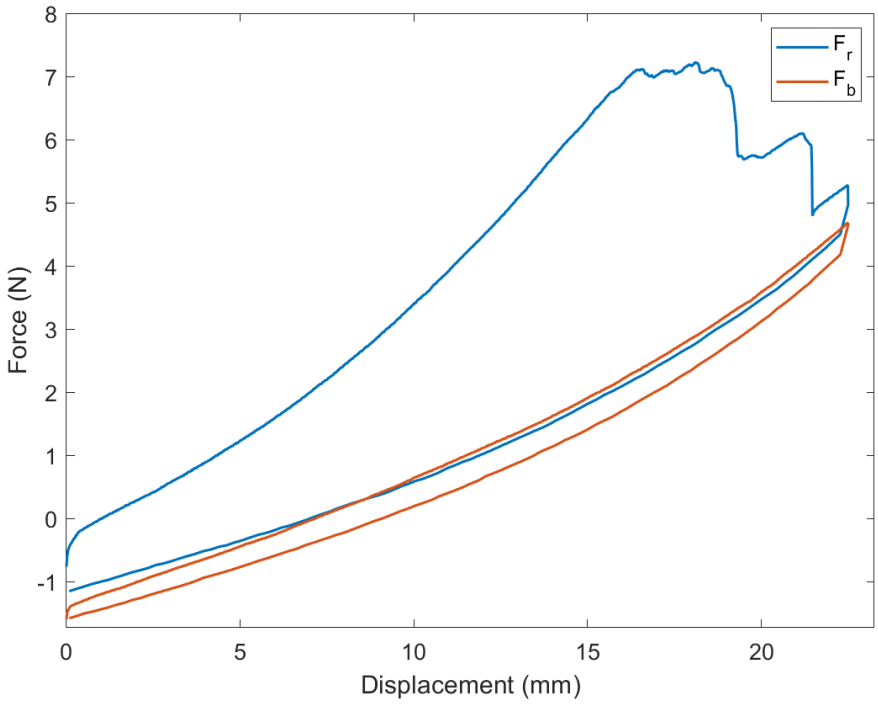

Figure 79: Raw force-displacement curve of C8 plotted alongside beam cycle 6 before offset correction.

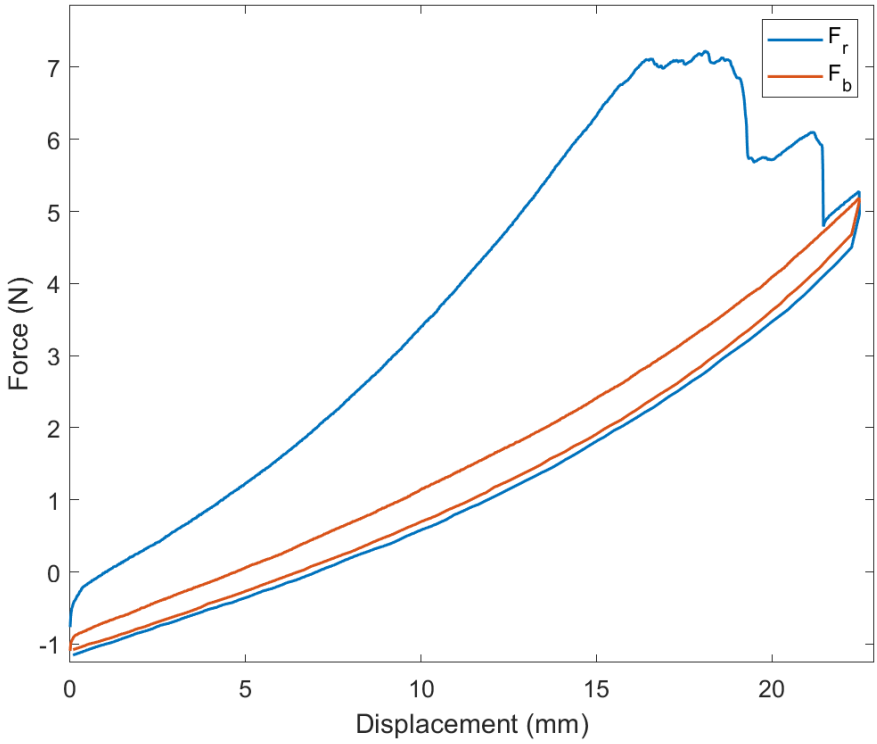

Figure 80: Raw force-displacement curve of C8 and beam cycle 6 after vertical alignment at the rupture point.

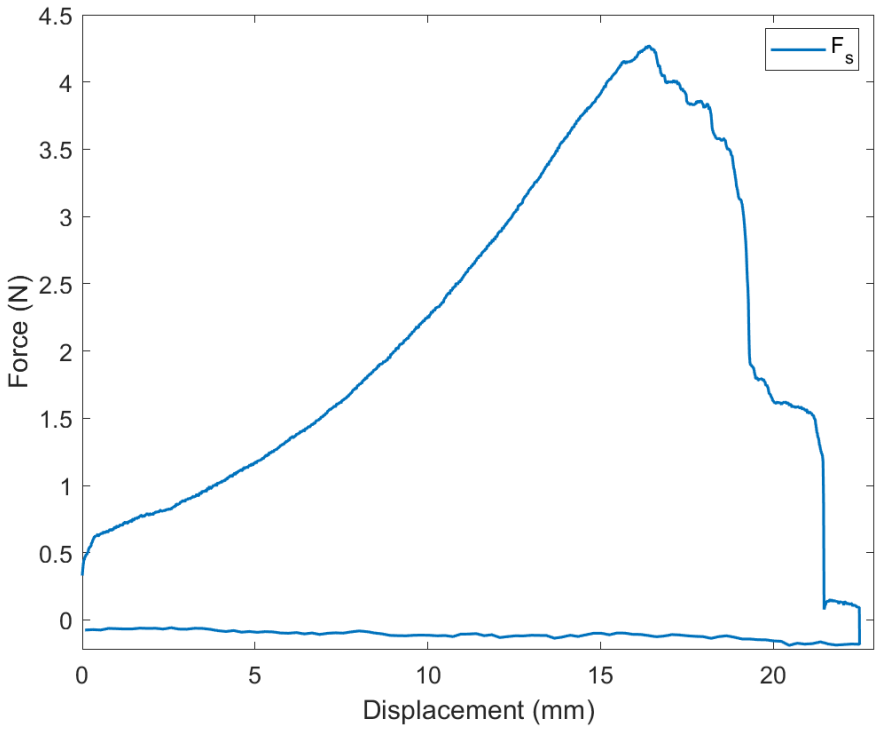

Figure 81: Corrected force-displacement curve of C8 after subtraction of the beam contribution.

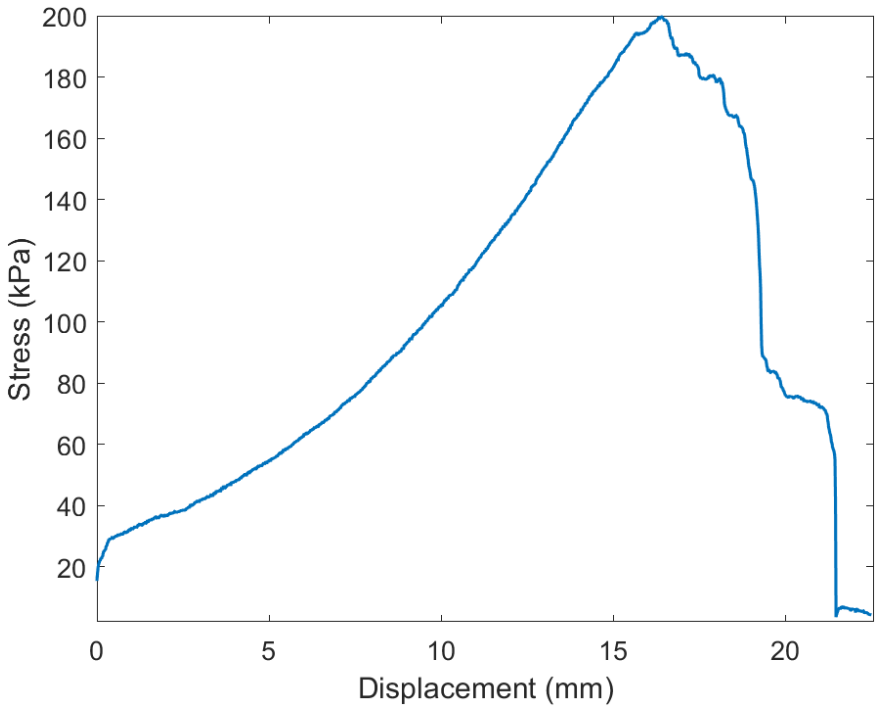

Figure 82: Engineering stress–displacement curve of C8. The peak corresponds to an ultimate engineering stress of 196.4 kPa. The curve shows the loading phase only.

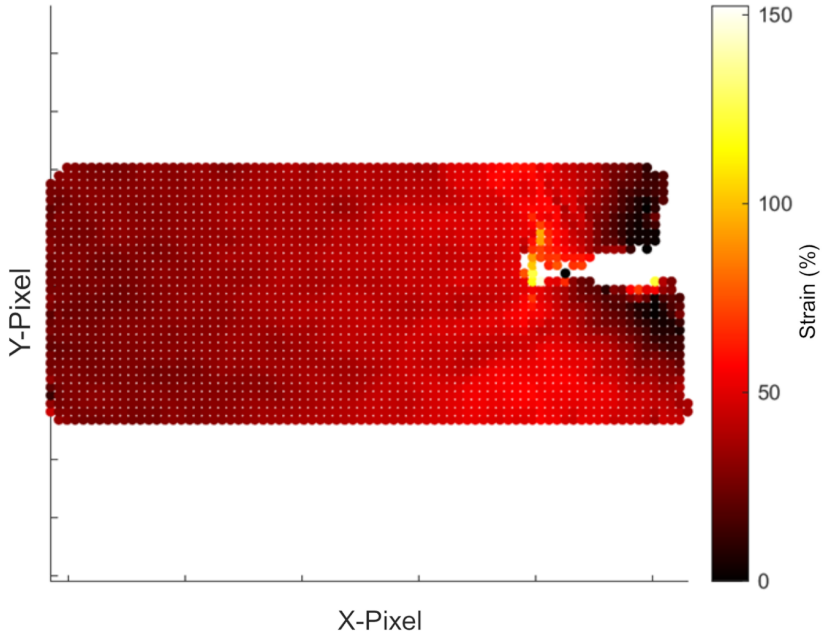

Figure 83: Heatmap of maximal principal strain across the sample surface, generated from the DIC image immediately before crack initiation. Yellow regions indicate high local strain, while red indicates lower strain levels. The ultimate strain was 153%.

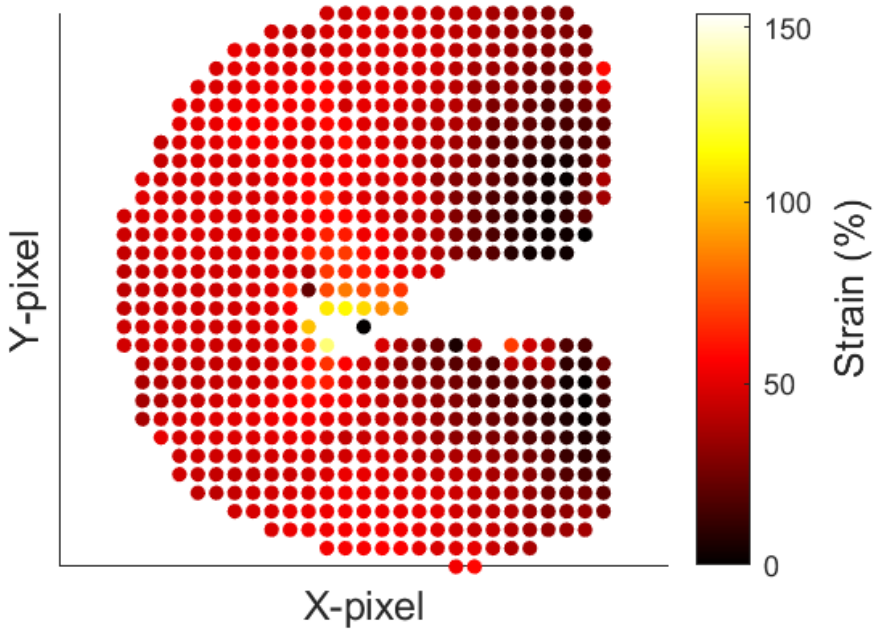

Figure 84: Zoomed-in strain heatmap of a circular region surrounding the crack tip. The average maximal principal strain within this region was 41.4%.

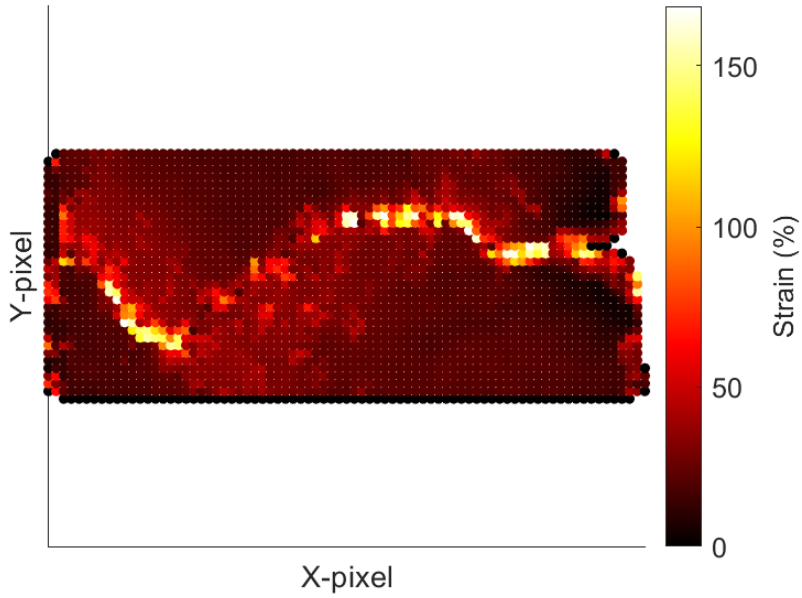

Figure 85: Cumulative heatmap of maximal principal strain recorded per pixel over the entire fracture test. The high-strain pattern visualizes the crack trajectory across the sample surface. Yellow regions represent highly strained areas, whereas red indicates lower strain values.

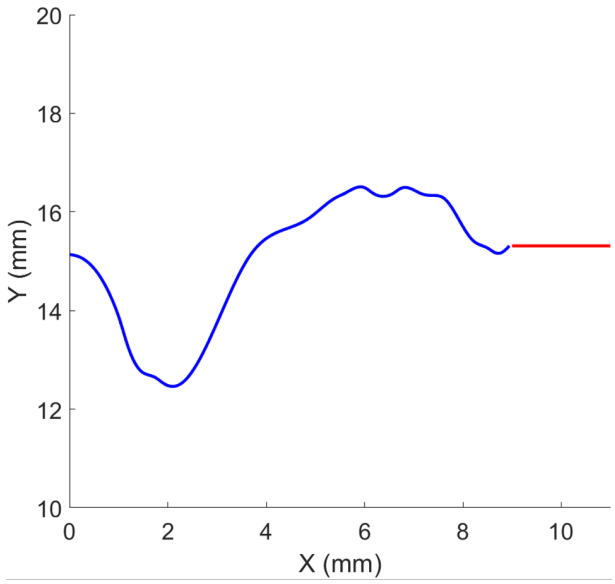

Figure 86: Reconstructed fracture path based on interpolated regions of highest strain. The 2 mm initial notch is shown in red. Pixel coordinates were converted to millimeters using the known sample width for calibration. The total crack path length was estimated to be 15.25 mm.

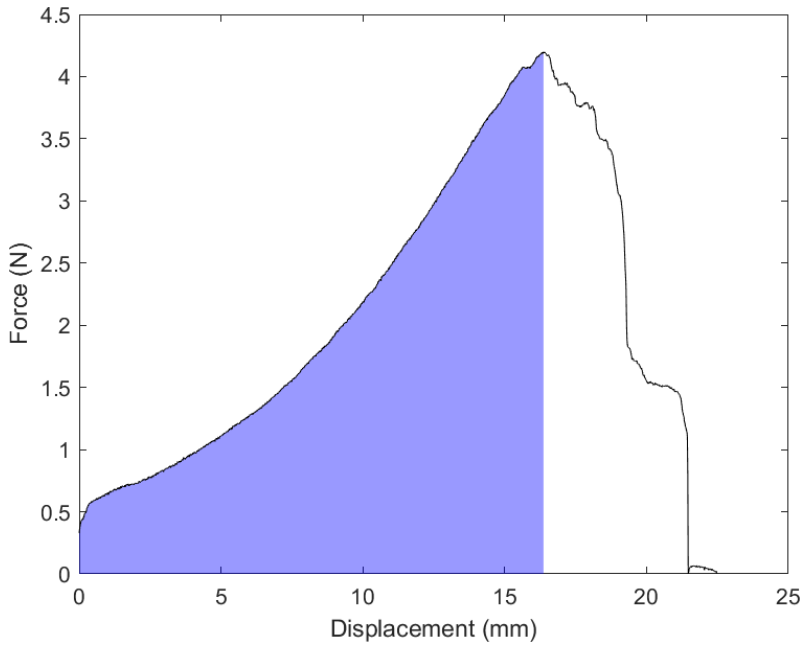

Figure 87: Calculation of the initiation energy. The blue area under the corrected force-displacement curve represents the mechanical work required to initiate rupture. The curve is integrated from the start of the test up to the point of visible crack formation. After normalization, the total initiation energy was 17.4 mJ/mm.

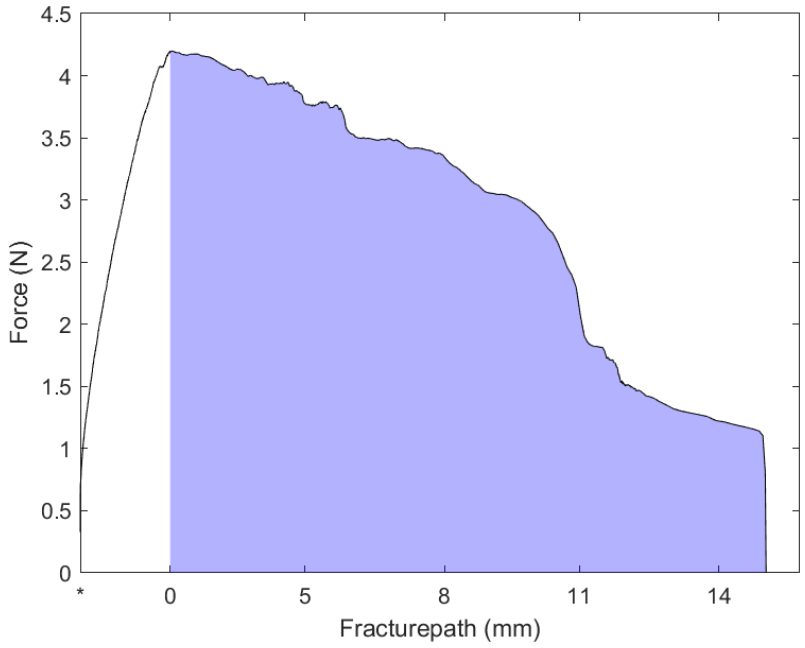

Figure 88: Calculation of the propagation energy. The blue area under the force–fracture path curve represents the mechanical work required to propagate the crack through the sample. After normalization, the dissipation was 1.31 mJ/mm^2.

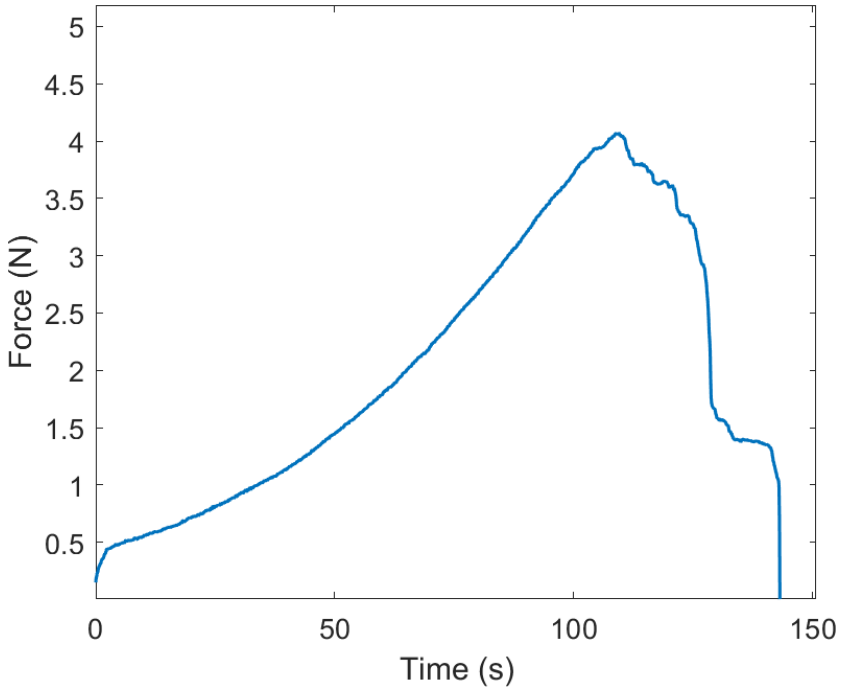

Figure 89: Raw force-time curve recorded by the biaxial testing machine during fracture testing. This dataset provided the force measurements used to construct the force-fracture path curve.

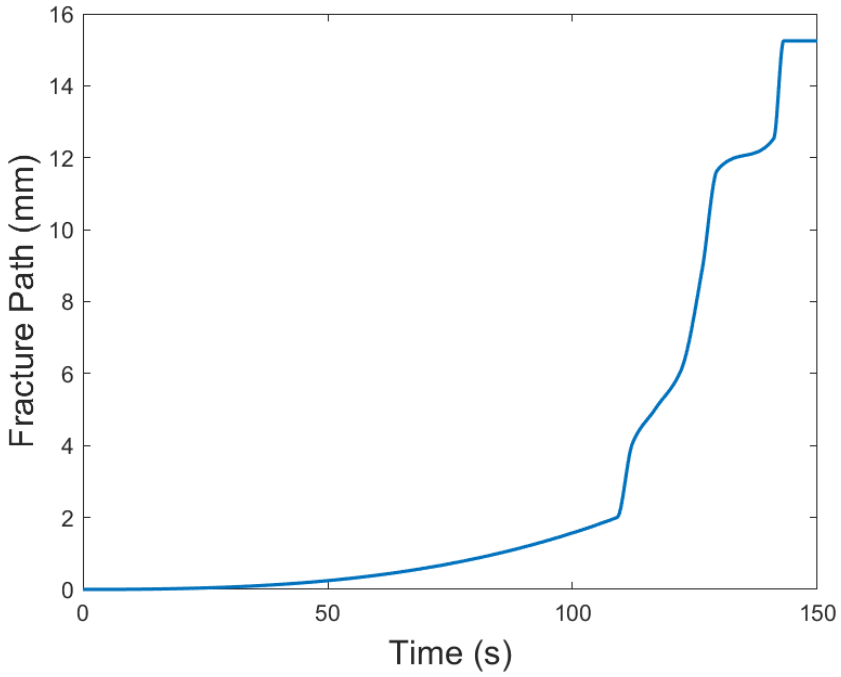

Figure 90: Fracture path–time curve reconstructed by manually analyzing DIC images. Fracture lengths were estimated by identifying the crack location at specific time points, enabling synchronization with the force-time data.

Mechanical behavior of beam used on January 30

This subsection shows the results of the separate beam-only test conducted on the beam used on January 30. From these measurements, beam cycle 6 was selected for subtraction during data correction.

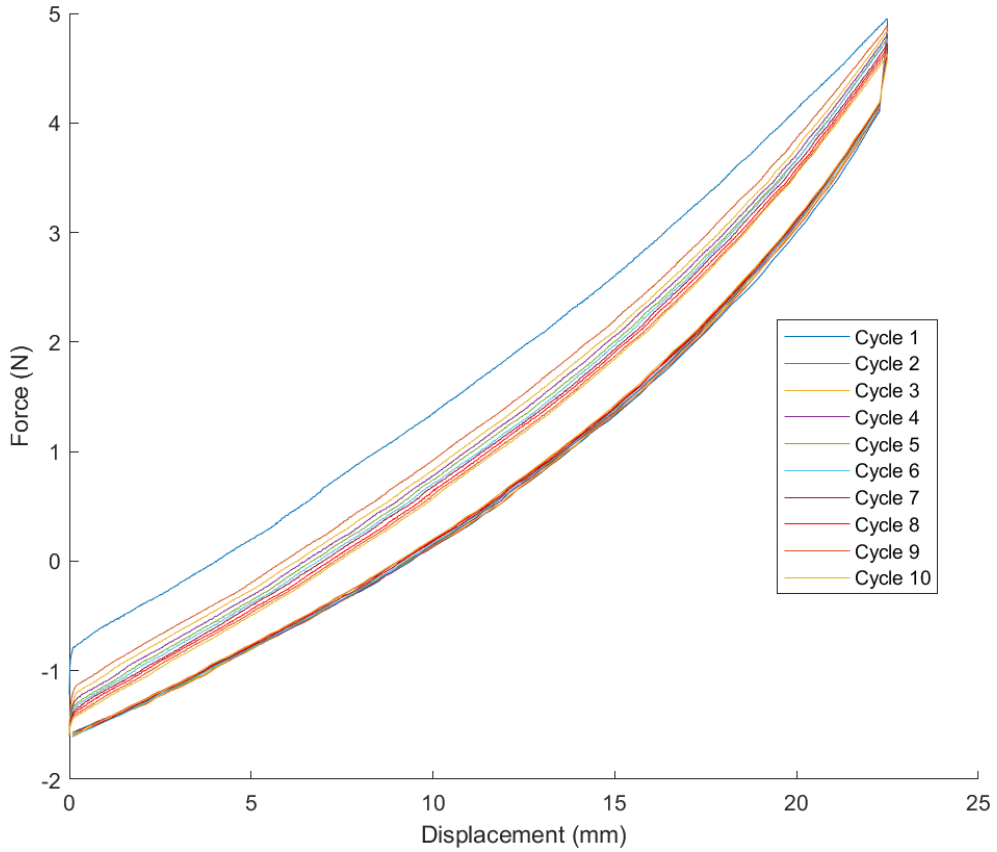

Figure 91: Force–displacement curves from ten successive beam-only loading-unloading cycles. The first cycle (blue) varies due to preconditioning effects. The following cycles increasingly exhibit more repetitive mechanical behavior. Beam cycle 6 (red) was selected for correction and subtraction from the sample curve.